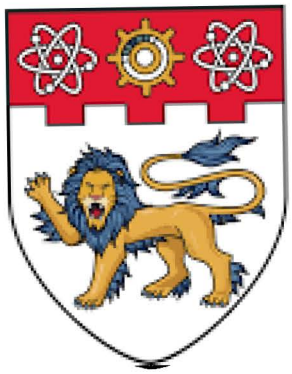

NANYANG TECHNOLOGICAL UNIVERSITY
SINGAPORE

MECHANICAL ENERGY HARVESTING USING PIEZOELECTRIC POLYMER FOR SELF-POWERED DEVICE APPLICATION

KAUSHIK PARIDA

SCHOOL OF MATERIALS SCIENCE AND ENGINEERING

2018

MECHANICAL ENERGY HARVESTING USING PIEZOELECTRIC POLYMER FOR SELF-POWERED DEVICE APPLICATION

KAUSHIK PARIDA

SCHOOL OF MATERIALS SCIENCE AND ENGINEERING

A thesis submitted to the Nanyang Technological University
in partial fulfilment of the requirement for the degree of
Doctor of Philosophy

2018

Statement of Originality

I hereby certify that the work embodied in this thesis is the result of original research and has not been submitted for a higher degree to any other University or Institution.

01-06-2018
.....
Date

Kaushik Parida
.....
Kaushik Parida

Abstract

The advent of portable electronics has propelled an immense enthusiasm to generate energy from the ambient environment. The availability of mechanical vibrations in the ambient environment is almost everywhere, making it a potential source of energy generation. Various mechanisms have been adopted to tap ambient mechanical vibrational energy. Piezoelectric, triboelectric, and electrostatic mechanisms have been used to convert these ambient mechanical energies into useful electrical energy. Piezoelectric materials have recently gained significant attention to harvest the ambient mechanical energy due to its inherent polarization. Piezoelectric polymers, specifically poly (vinylidene fluoride - trifluoroethylene) [P(VDF-TrFE)], due to its higher piezoelectric coefficient have been extensively explored. Moreover, they can sustain higher stress, strains and strain rates compared to inorganic piezoelectric materials. Additionally, they are flexible, transparent, and chemically stable, thus making it suitable for self-powered device applications. However, the energy harvesting ability of piezoelectric polymers are unsatisfactory and cannot be effectively used to power electronics devices. Extensive effort has been made to enhance the energy harvesting performance of P(VDF-TrFE) films by employing various strategies. The performance can be improved by tuning the fundamental properties such as piezoelectric coefficient, dielectric constant, strain, surface charge, and capacitance. The specific objective of the the work presented in this dissertation is to increase the energy harvesting performance of P(VDF-TrFE) by tuning the structural, surface charge and capacitance of the device.

The structural properties of the P(VDF-TrFE) is tuned by a creating porous P(VDF-TrFE) film. The porous P(VDF-TrFE) film showed an increment in the power density by 88 times compared to that of the compact P(VDF-TrFE) film attributed to the lower dielectric constant, higher β phase content and higher compressibility of the porous P(VDF-TrFE) film. A self-charged supercapacitor was demonstrated by utilizing the porous P(VDF-TrFE) film as the separator. Fabrication of the porous P(VDF-TrFE) energy harvester is extremely difficult due to the dielectric breakdown of the porous film on application of an electric

field. This problem is circumvented by fabricating a self-poled porous P(VDF-TrFE) sponge, which also eliminates the tedious and costly annealing and poling processes. The output performance of the P(VDF-TrFE) film in the triboelectric energy harvester mode depends on the surface charge density. Enhanced energy harvesting performance of the P(VDF-TrFE) is demonstrated by utilizing the combined effect of triboelectric surface charge and polarization induced surface charge of the self-polarized P(VDF-TrFE) film. The device is used to fabricate a self-powered wide range pressure sensor which can detect pressure ranging from 0.05 to 600 kPa with high sensitivity. Lastly, the capacitance of the device is tuned by using a slime-based ionically conducting current collectors for triboelectric nanogenerator (TENG). The use of ionic current collector leads to the formation of an electric double layer which increases the capacitance of the device thus improving the energy harvesting performance.

Acknowledgements

First, I would like to express gratitude to my supervisor Prof. Pooi See Lee for her guidance, support, and advice, during my Ph.D. I would like to thank her, for teaching and inspiring me to develop a scientific mindset. I will be grateful for all the tiring and time consuming scientific discussions, brainstorming, and providing me creative ideas to solve problems during my Ph.D. I would like to express my gratitude to the thesis advising committee, Assoc. Prof. Lu Xuehong and Assoc. Prof. Raju V. Ramanujan for their suggestions, recommendations and valuable time. I am thankful to all the technical staff of MSE, NTU and to Nanyang Technological University, Singapore for funding my Ph.D. I would like to thank all my lab members, including Dr. Venkateswarlu Bhavanasi, Dr. Vipin Kumar, Dr. Rama Raju Bendi, Dr. Wang Jiangxin, Dr. Lin Meng-Fang, Dr. Nguyen Viet Cuong, Dr. Chee Jianzhi Kenji, Qian Kai, Dr. Xiong Jiaqing and Chen Xiaoliang for all the technical discussion and experimental help. Finally, I dedicate this dissertation to my parents, sisters and all family members. I want to thank my father Prof. Kulamani Parida and my mother Mrs. Renubala Parida, who inspired me to pursue research, supported and believed in me. Without their constant support, blessing, and motivation, this could not have been possible.

Acknowledgements

Table of Contents

Abstract i

Acknowledgements iii

Table of Contents v

Table Captions ix

Figure Captions xi

Abbreviations xxi

Chapter 1 Introduction 1

1.1 Hypothesis and Problem Statement 2

1.2 Objectives and Scope 3

1.3 Dissertation Overview 4

1.4 Findings and Outcomes/Originality 5

References 6

Chapter 2 Literature Review 7

2.1 Overview 8

2.1.1 Energy harvesting technologies 8

2.1.2 Piezoelectric energy harvester 10

2.1.3 Triboelectric energy harvester 11

2.1.4 Various piezoelectric materials 14

2.1.5 Piezoelectric P(VDF-TrFE) 15

2.1.6 Various methodologies to improve the energy harvesting performance of P(VDF-TrFE) 16

2.1.5 Self-powered devices 20

References xx

Chapter 3 Experimental Methodology 27

3.1 Rationale for selection of Materials 28

3.2 Typical experimental procedure 28

3.3 Fabrication 29

3.4 Characterization 34

References xx

Chapter 4 Porous P(VDF-TrFE) Films 39

4.1 Introduction 40

4.2 Results and Discussion 40

4.2.1 Morphological characterization of porous P(VDF-TrFE) 40

4.2.2 Phase identification and quantification of P(VDF-TrFE) film 42

4.2.3 Energy harvesting performance of porous P(VDF-TrFE) film 44

4.2.4 Application - Self-charged supercapacitor 49

4.3 Principle Outcomes 56

4.4 Chapter Summary 56

References xx

Chapter 5 Self-polarized porous P(VDF-TrFE) film 59

5.1 Introduction 60

5.2 Results and Discussion 60

5.2.1 Morphological and ferroelectric characterization of the porous self-poled P(VDF-TrFE) film 60

5.2.2 Evaluation of the self-poled porous P(VDF-TrFE) film 62

5.2.3 Enhancement of the energy harvesting performance of the self-poled porous P(VDF-TrFE) film 66

5.3 Application - self-powered wide-range pressure sensor 71

5.2.1 Evaluation of pressure sensor 74

5.2.2 Practical application of the self-poled P(VDF-TrFE) pressure sensor 78

5.4 Principal outcomes 83

5.5 Chapter Summary 84

References xx

Chapter 6 Ionic current collector for porous P(VDF-TrFE) film 89

6.1 Introduction 90

6.2 Results and Discussion 90

6.2.1 Characterization of the ionic conductor 90

6.2.2 Mechanism of energy generation 92

6.2.3 Energy harvesting performance of the porous P(VDF-TrFE) with ionic current collector 94

6.2 Self-healing energy harvester 97

6.2.1 Mechanical properties of the self-healing ionic current collector 99

6.3 Principle Outcomes 103

6.4 Chapter Summary 104

References 104

Chapter 7 Conclusions and recommendations 107

7.1 Conclusions 108

7.2 Future work 109

References .....

Table Captions

Table 2.1 Comparison of the piezoelectric and triboelectric energy harvesters.

Table 2.2 Triboelectric series.

Table 2.3 Piezoelectric properties of the various piezoelectric materials.

Table 2.4 Summary of the recent work on P(VDF-TrFE) based mechanical energy harvesters.

Table 4.1 Summary of the energy harvesting performance of the compact and porous P(VDF-TrFE) film.

Table 4.2 Table highlighting the state-of-the-art self-powered electrochemical energy storage devices.

Table 5.1 Comparison of the energy harvesting performance of the self-poled and non-poled porous P(VDF-TrFE) TEH.

Table 5.2 Comparison of different characteristics of various pressure sensor.

Table 5.3 Sensitivity and pressure range of various self-powered pressure sensors.

Table 6.1 Summary of the energy harvesting performance of the porous P(VDF-TrFE) TEH with and without ionic current collector.

Table 7.1 Summary of the energy harvesting performance of all the work done in this dissertation.

Table Captions

Figure Captions

Figure 2.1. (a) The various mechanical forces present in the ambient environment. (b) The power required by the various electronic devices.

Figure 2.2. Schematic of the piezoelectric energy harvester.

Figure 2.3. Schematic of the triboelectric energy harvester.

Figure 2.4. Schematic of different modes of triboelectric energy harvester. (a) The vertical contact-separation mode. (b) The lateral sliding mode. (c) The single-electrode mode. (d) The free-standing mode. Reproduced with permission from the Royal Society of Chemistry.

Figure 2.5. First-order lumped-parameter equivalent circuit model of the triboelectric device.

Figure 2.6. Schematic of the self-powered system.

Figure 3.1. Experimental protocol followed in this dissertation.

Figure 3.2. Schematic representation of the fabrication of the porous P(VDF-TrFE) film.

Figure 3.3. Schematic representation of the fabrication of the self-poled porous P(VDF-TrFE) film.

Figure 3.4. Schematic diagram of the piezoelectric energy harvester.

Figure 3.5. Schematic diagram of the fabrication process of the TENG with the ionic conductor as the current collector.

Figure 3.6. Schematic diagram of the measurement setup used to measure the energy harvesting performance.

Figure 4.1. FESEM image of the porous P(VDF-TrFE) film prepared with variation of the volume percentage of DMF:acetone at (a) 100:0, (b) 75:25, (c)

50:50, and (d) 25:75. (e) FESEM image of the compact P(VDF-TrFE) film. Scale bar = 100 μm. (f) Variation of % porosity with the change in the volume percentage of DMF:Acetone.

Figure 4.2. (a) FT-IR spectra of the P(VDF-TrFE) compact and porous film with variation of the volume percentage of DMF:acetone at (1) 100:0, (2) 75:25, (3) 50:50, and (4) 25:75. (b) The relative proportion of β phase for the compact and porous P(VDF-TrFE) film. (c) FT-IR spectra of the porous P(VDF-TrFE) film indicating the interfacial interactions. (d) XRD spectra of the P(VDF-TrFE) compact film and the porous foam with variation of the volume percentage of DMF:acetone at (1) 100:0, (2) 75:25, (3) 50:50, and (4) 25:75

Figure 4.3. Schematic of the working of the piezoelectric energy harvester.

Figure 4.4. Schematic diagram of the porous P(VDF-TrFE) piezoelectric energy harvester. (b) Digital image of the porous P(VDF-TrFE) piezoelectric energy harvester. (c)Voltage output generated from the porous P(VDFTrFE) piezoelectric energy harvester when subjected to a pressure of 600 kPa at a frequency of 5 Hz. (d) Current density generated from the porous P(VDFTrFE) piezoelectric energy harvester when subjected to a pressure of 600 kPa at a frequency of 5 Hz. (e) Variation of voltage output of the porous P(VDF-TrFE) piezoelectric energy harvester with the variation of applied pressure (exerted at 5 Hz frequency). (f) Power density of the porous P(VDF-TrFE) piezoelectric energy harvester across various resistances when subjected to a mechanical pressure of 600 kPa at 5 Hz frequency. (g) Stability of the porous P(VDF-TrFE) piezoelectric energy harvester when subjected to a mechanical pressure of 600 kPa at a frequency of 5 Hz for 10000 cycles. (h) Variation of voltage output of the porous P(VDF-TrFE) piezoelectric energy harvester with the variation of applied frequency (exerted at 600 kPa pressure).

Figure 4.5. (a) Voltage output generated from the non-porous P(VDFTrFE) piezoelectric energy harvester when subjected to a pressure of 600 kPa at a frequency of 5 Hz. (d) Current density generated from the non-porous P(VDFTrFE) piezoelectric energy harvester when subjected to a pressure of 600 kPa at a frequency of 5 Hz.

Figure 4.6. (a) Compressive stress-strain behaviour of the porous and compact P(VDF-TrFE) film. (b) Variation of dielectric permittivity with the change in applied frequency for the porous and compact P(VDF-TrFE) film.

Figure 4.7. (a) FE-SEM image of the CNT electrode. (b) Cross-section of the electrode showing the embedded portion of CNT in PDMS. (c) Digital image of the CNT embedded in PDMS electrode. (d) Digital image showing the high flexibility of the electrode.

Figure 4.8. Electrochemical performance of the self-charged supercapacitor. (a) Cyclic voltammogram (CV) of the self-charged supercapacitor at a scan rate of 20 mVs^{-1}. (b) Galvanostatic charging and discharging curves of the self-chrged supercapacitor measured at current densities of 0.050, 0.075, 0.10, and 0.25 $mAcm^{-2}$. (c) The areal capacitance of the self-charged supercapacitor method at various current densities. (d) Areal capacitance retention of the self-charged supercapacitor when subjected to a mechanical pressure of 600 kPa at a frequency of 5 Hz.

Figure 4.9. (a) Schematic of the self-charged super capacitor. (b) Demonstration of the self-charging of the supercapacitor when subjected to a compression pressure of 420 kPa at a frequency of 5 Hz exerted for 40 s and then discharged at a current density of 0.1 $mAcm^{-2}$. (c) The control sample

with filter paper (impregnated with gel electrolyte), showed no increment in the OCP under the similar experimental conditions. (d) Demonstration of the self-charging of the supercapacitor when subjected to a compression pressure of 120 and 350 kPa exerted at a frequency of 10 Hz for 10 s. (e) Demonstration of the self-charging of the supercapacitor when subjected to a compression pressure of 350 kPa at a frequency of 5 Hz and 10 Hz exerted for 10 s. (f) Demonstration of the stability of the supercapacitor by self-charging (by exerting a mechanical pressure of 600 kPa at a frequency of 10 Hz for 50 s) and discharging (by a discharge current of 5 $mAcm^{-2}$) for 50 cycles.

Figure 4.10. Schematic representation of the mechanism of SP-EDLC device. (a) The device is maintained at equilibrium condition where the ions are uniformly distributed in the P(VDF-TrFE) film. (b) On application of the mechanical pressure an electric field is developed which leads to the migration of ions. (c) Development of an EDL layer at the electrodes.

Figure 5.1. (a) Digital photo of the self-poled porous P(VDF-TrFE) film. (b) FESEM image showing the top view of self-poled porous P(VDF-TrFE) film. Inset in (b) is an enlarged FESEM image showing a pore. Scale bar: 10 μm. (c) Cross-sectional FESEM images of the self-poled porous P(VDF-TrFE) film.

Figure 5.2. (a) XRD spectra of the self-poled porous P(VDF-TrFE) film. (b) FTIR spectra of the self-poled porous P(VDF-TrFE) film.

Figure 5.3. PFM phase image of the (a) Self-poled porous P(VDF-TrFE) film. (b) Non-poled compact P(VDF-TrFE) film.

Figure 5.4. (a) Schematic diagram of self-poled porous P(VDF-TrFE) piezoelectric energy harvester. (b) The voltage output of self-poled porous P(VDF-TrFE) PEH, when subjected to a mechanical pressure of 625 kPa exerted

at a frequency of 20 Hz. (c) The voltage output from the control sample (non-poled compact P(VDF-TrFE) film, prepared by spin coating method), when subjected to a mechanical pressure of 625 kPa, exerted at a frequency of 20 Hz. (d) The voltage output with the variation of fabrication temperature of the P(VDF-TrFE) film (at 50% RH), when subjected to a pressure of 625 kPa exerted at a frequency of 20 Hz. (e) The voltage output from the P(VDF-TrFE) film (fabricated at a temperature of −20 °C in the absence of humidity (< 5% RH)), when subjected to a pressure of 625 kPa exerted at a frequency of 20 Hz. (f) FTIR spectra demonstrating a peak at 3,600−3,120 cm^{-1} region verifying the presence of the hydrogen bond in the self-poled P(VDF-TrFE) film.

Figure 5.5. (a) Schematic diagram of the P(VDF-TrFE) TEH. (b) Schematic diagram of the negatively and positively polarized P(VDF-TrFE).

Figure 5.6. Schematic diagram of the mechanism of the P(VDF-TrFE) THE.

Figure 5.7. (a) Digital photo of the TEH device. (b) Voltage output of the self-poled. P(VDF-TrFE) TEH subjected to pressure of 600 kPa exerted at a frequency of 5 Hz. (c) Current density of the self-poled P(VDF-TrFE) TEH subjected to pressure of 600 kPa exerted at a frequency of 5 Hz. (d) Voltage output response of the non-poled P(VDF-TrFE) TEH subjected to a pressure of 600 kPa exerted at a frequency of 5 Hz.

Figure 5.8. (a) Voltage output response of the non-poled P(VDF-TrFE) TEH subjected to a pressure of 600 kPa exerted at a frequency of 5 Hz. (b) Current density of the non-poled P(VDF-TrFE) TEH subjected to pressure of 600 kPa exerted at a frequency of 5 Hz.

Figure 5.9. (a) Charge transfer of self-poled porous P(VDF-TrFE) TEH subjected to pressure of 600 kPa exerted at a frequency of 5 Hz. (b) Charge transfer of non-poled porous P(VDF-TrFE) TEH subjected to pressure of 600

kPa exerted at a frequency of 5 Hz. (c) The voltage output pulse of the self-poled porus P(VDF-TrFE) TEH subjected to a pressure of 600 kPa exerted at a frequency of 5 Hz. (b) The voltage output pulse of the non-poled P(VDF-TrFE) TEH subjected to a pressure of 600 kPa exerted at a frequency of 5 Hz.

Figure 5.10. (a) Stability of self-poled porous P(VDF-TrFE) TEH for medium-pressure range (30 kPa). (d) Stability of self-poled porous P(VDF-TrFE) TEH for high-pressure range (350 kPa). (c) The voltage output of the self-poled P(VDF-TrFE) TEH at different % relative humidity (%RH) at a mechanical pressure 150 kPa exerted at a frequency of 5 Hz.

Figure 5.11. (a) Voltage output of the non-poled P(VDF-TrFE) pressure sensor for low-pressure range (0.1 to 5 kPa). (c) Voltage output of the non-poled P(VDF-TrFE) pressure sensor for medium pressure range (5 to 50 kPa). (d) Voltage output of the non-poled P(VDF-TrFE) pressure sensor for high-pressure range (50 to 600 kPa).

Figure 5.12. (a) Voltage output of self-poled P(VDF-TrFE) pressure sensor for low-pressure range (0.05 to 5 kPa). (e) Voltage output of self-poled P(VDF-TrFE) pressure sensor for medium-pressure range (5 to 60 kPa). (f) Voltage output of self-poled P(VDF-TrFE) pressure sensor for high-pressure range (60 to 600 kPa).

Figure 5.13. (a) Response time of self-poled P(VDF-TrFE) pressure sensor upon application of mechanical pressure of 600 kPa at a frequency of 5 Hz. (b) Variation of the output voltage of the self-poled P(VDF-TrFE) TEH with a range from 0.05 to 600 kPa. (c) Voltage error in percentage between linear fit and actual characteristics of the TEH for the range of 0.05 to 600 kPa.

Figure 5.14. Practical application of self-poled porous P(VDF-TrFE) pressure sensor for human-machine interface and smart robotics. (a) Pressure sensor attached to the finger of the humanoid robot to detect pressure exerted by human touch. Scale bar: 4 cm. (b) Voltage output generated from a gentle and hard finger tapping on pressure sensor attached to humanoid robot finger. (c) Photograph of pressure sensor attached to the foot of humanoid robot to detect robot motion. Scale bar: 10 cm. (d) Voltage output generated during slow and fast foot tapping of the humanoid robot.

Figure 5.15. Practical application of the pressure sensor is to monitor the landing of a quadcopter robot. (a) Pressure sensor application to detection of landing pressure of large quadcopter robot. Scale bar: 20 cm. (b) Voltage output detected during the landing of the large quadcopter robot. (c) Photograph of the pressure sensor to monitor the landing of a mini quadcopter robot. Scale bar: 20 cm. (d) Voltage output detected during the smooth landing of the mini quadcopter robot on the pressure sensor. (e) Voltage output detected during take-off of the mini quadcopter robot from the pressure sensor. (f) Voltage output detected during the crash landing of the mini quadcopter robot on the pressure sensor.

Figure 5.16. (a) The self-poled P(VDF-TrFE) pressure sensor arranged in a matrix for the pressure-mapping application. (b) Application of pressure on to the self-poled P(VDF-TrFE) pressure sensor by finger tapping. (c) 3D pressure map of pressure exerted on self-poled P(VDF-TrFE) pressure sensor upon finger tapping. (d) 2D pressure map of pressure exerted on self-poled P(VDF-TrFE) pressure sensor upon finger tapping.

Figure 5.17. (a) Photograph of the self-poled P(VDF-TrFE) pressure sensor to detect pressure exerted by a robotic arm during object manipulation. Scale bar: 20 cm. (b) Voltage output during objects (light and heavy weight)

manipulation (loading and unloading) on the self-poled P(VDF-TrFE) pressure sensor by the robotic arm.

Figure 5.18. (a) Digital photo of the self-poled P(VDF-TrFE) pressure sensor device demonstrating high flexibility (with a bending angle = 180°). (b) Bending cycle stability of the self-poled P(VDF-TrFE) pressure sensor. (c) Digital photo of the pressure sensor attached to the finger to detect finger movements. (d) Voltage output detected by bending the finger.

Figure 6.1. (a) Schematic diagram of the IS-TEH. (b) Digital photo of the highly transparent IS-TEH. (b) Digital photo of the ionic conductor showing high transparency. (c) Transmittance spectra of the PVA slime (ionic conductor) with respect to a glass slide. (d) Illustration of reaction between PVA and borate ions leads to the formation of slime (a borate cross-linked poly(vinyl alcohol)). (e) Electrochemical impedance spectroscopy measurement of the slime (ionic conductor). (f) FTIR spectra of the PVA slime (ionic conductor).

Figure 6.2. Schematic diagram of the mechanism of energy generation of the TEH with the ionic conductor.

Figure 6.3. The energy harvesting performance of the IS-TEH when subjected to a mechancial pressure of 600 kPa at a frequency of 5 Hz. (a) Voltage output (V_{oc}) (b) Current density (I_s). (c) Variation of voltage and current as a function of load resistance of the IS-TEH. (d) Schematic diagram of the TEH without the ionic current collector. The energy harvesting performance of the TEH without ionic current collector when subjected to a mechancial pressure of 600 kPa at a frequency of 5 Hz. (e) Voltage output (V_{oc}) (f) Current density (I_s).

Figure 6.4. Capacitance of the PVA slime and P(VDF-TrFE) as a function of frequency.

Figure 6.5. (a) The voltage output of the IS-TEH before mechanical damage and self-healed device. (b) The change in the resistance of the slime during bifurcation and self-healing.

Figure 6.6. Schematic representation of the self-healing process of the IS-TEH.

Figure 6.7. The changes in the storage (G') and loss modulus (G") as a function of angular frequency for the virgin and self-healed PVA ionic conductor.

Figure 6.8. (a) and (b) The tensile stress-strain curve of 3 virgin PVA slime samples.

Figure 6.9. (a) and (b) The tensile stress-strain curve of the self-healing and virgin PVA ionic conductor.

Figure 6.10. The tensile stress-strain curve of the self-healing PVA slime with different healing times.

Figure 6.11. The tensile stress-strain curve of the (a) Virgin PVA slime (b) Self-healed PVA slime (with 15 min self-healing duration) (c) Self-healed PVA slime (with 15 min self-healing duration) after the keeping the bifurcated parts separated for 24 h.

Figure Captions

Abbreviations

PVDF	Poly(vinylidene fluoride)
P(VDF-TrFE)	Poly(vinylidene fluoride-trifluoroethylene)
VIPS	Vapor Induced phase separation
XRD	X-ray diffraction
FESEM	Field Emission Scanning Electron Microscopy
AFM	Atomic Force Microscopy
$PbTiO_3$	Lead Titania
$BaTiO_3$	Barium Titanate
AlN	Aluminium Nitride

Chapter 1

Introduction

Energy is one of the cardinal aspects of human life; in fact, the importance of energy can be reflected from the mammoth forecasted 25 % increment in the per capita energy consumption by 2040. (Outlook for Energy, Exxonmobil report, 2017). The world is highly dependent on energy, and its appetite is increasing day by day. A possible solution is to use to alternative or renewable means of energy generation. In this work, P(VDF-TrFE) is used as a piezoelectric polymer for mechanical energy harvesting. It is highly flexible, transparent, and can sustain high mechanical stress compared to that of the inorganic materials. Amongst the organic materials, P(VDF-TrFE) shows the highest piezoelectric coefficient. In this dissertation, various strategies are adopted to increase the energy harvesting performance of P(VDF-TrFE), and it is used in different self-powered device applications. In this chapter, the problem statement, objective of the dissertation, hypothesis, originality, findings, and overview of the thesis is highlighted.

1.1 Hypothesis and problem statement

Piezoelectric materials are potential candidates for the fabrication of mechanical energy harvesters (MEH) due to the inherent polarization, which generates a voltage output on the application of mechanical pressure. Compared to inorganic materials, organic piezoelectric materials can sustain higher mechanical strain, stress and strain rate. Moreover, they are flexible, transparent and chemically stable. Thus, they are more suitable for the realization of multifunctional and self-powered devices. However, the energy harvesting ability of the piezoelectric polymers are low compared to inorganic piezoelectric materials, and the amount of power generated is not sufficient for self-powered device application. Voltage output of a piezoelectric energy harvester is given by the following equation 1.1.[1]

$$V = \frac{\sigma t d_{33}}{\epsilon} \tag{1.1}$$

where V = voltage output, ϵ = dielectric constant, σ = mechanical stress, t = thickness and d_{33} = piezoelectric coefficient. The mechanical stress is the product of Young's modulus and strain in the material. Mechanical stress (σ) = Young's modulus (Y) * Strain (ε). Thus, the equation 1.1 can be modified as equation 1.2.

$$V = \frac{Y \varepsilon t d_{33}}{\epsilon} \tag{1.2}$$

The voltage output of the triboelectric energy harvester is given by the equation 1.3.[2]

$$V = \frac{\sigma x}{\epsilon} \tag{1.3}$$

where, V = voltage output, ε = permittivity of free space, σ = surface charge density, x = separation distance between the two polymers. Thus, by tuning the intrinsic properties (such as the dielectric constant and strain exerted on the material), the energy harvesting performance of P(VDF-TrFE) can be improved. From equation 1.2, it can observe that by decreasing the dielectric constant and by increasing the strain on the material the voltage output of the device can be improved. Therefore, it is hypothesized that by creating porous

P(VDF-TrFE) films (with higher strain and lower dielectric constant) the energy harvesting performance of the P(VDF-TrFE) can be improved. Additionally, porous structure increases the compressibility of the material, which in turn can increase the piezoelectric coefficient. From equation 1.3, it can observed that by increasing the surface charge density of the polymer the voltage output can be improved. Therefore, the second hypothesis of this thesis is that by utilizing the combined effect of triboelectric surface charge and polarization induced surface charge, the energy harvesting performance of the P(VDF-TrFE) can be further improved. The surface charge density depends on the capacitance of the device. Therefore, last, but not least, it is hypothesized that by utilizing an ionic current collector in P(VDF-TrFE) mechanical energy harvester, the capacitance of the device can be improved, which can increase the energy harvesting performance.

1.2 Objective and scope

The objective of the thesis work is to enhance the mechanical energy harvesting performance of the P(VDF-TrFE) and utilize it for self-powered device application.

In this study, the energy harvesting performance of the P(VDF-TrFE) was improved by changing its physical properties such as compressibility and dielectric constant by creating porous P(VDF-TrFE) films. The combined effect of triboelectric surface charge and piezoelectric polarization was utilized to enhance the energy harvesting performance. Additionally, the use of ionic current collector for charge collection further enhances the performance. For application demonstrations, the P(VDF-TrFE) MEH was utilized for the realization of a self-charging supercapacitor, wide-range self-powered pressure sensor, and a touch sensor.

1.3 Dissertation Overview

Chapter 2 presents an overview of the mechanical energy harvesters, particularly piezoelectric and triboelectric energy harvesters. Various piezoelectric materials including both organic and inorganic materials are discussed. Detailed discussion on the P(VDF-TrFE) is provided. The methodologies adopted to improve the energy harvesting performance are discussed.

Chapter 3 presents the discussion on the experimental methodologies adopted in this dissertation. Specifically, detailed discussion on the fabrication of various materials and devices are provided. All the characterization techniques used to characterize the materials and devices are discussed in detail.

Chapter 4 presents the use of porous P(VDF-TrFE) films, to enhance the energy harvesting performance. The porous P(VDF-TrFE) films, showed an increment in the power density by 88 times compared to that of the compact film. The superior energy harvesting performance of the porous P(VDF-TrFE) film as compared to the compact P(VDF-TrFE) film, can be attributed to the following factors: lower dielectric constant, higher β phase content and higher compressibility. Detailed results are provided with proper explanations.

Chapter 5 presents the fabrication of self-poled porous P(VDF-TrFE) film. Here a combinational effect of triboelectric surface charge and piezoelectric polarization was utilized to enhance the performance of the mechanical energy harvester. Furthermore, this effect was used to fabricate a self-powered wide range pressure sensor. Detailed results are provided with proper explanations.

Chapter 6 presents the use of ionic current collector in mechanical energy harvester. The ionic conductor shows enhanced energy harvesting performance compared to the electronic current collector due to the formation of an electric double layer. Additionally, a self-healing energy harvester is demonstrated. Detailed results are provided with proper explanations.

Chapter 7 provides the summary and conclusion of the dissertation and provides direction for future work.

1.4 Findings and outcomes/originality of the work

The following are the findings, outcomes, and originality of this work

1. A porous P(VDF-TrFE) film was successfully fabricated which shows superior energy harvesting performance compared to that of the compact P(VDF-TrFE) film. The enhanced performance can be attributed to lower dielectric constant, higher β phase content and higher compressibility. A fast self-charging supercapacitor is fabricated by utilizing the porous P(VDF-TrFE) film as the separator.
2. Developed a novel method to fabricate a self-polarized P(VDF-TrFE) film eliminating the costly and tedious annealing and poling processes. Enhanced the energy harvesting performance of the P(VDF-TrFE) by utilizing the combined effect of triboelectric surface charge and polarization induced surface charge of the self-polarized P(VDF-TrFE) film. Demonstrated a wide range self-powered pressure sensor.
3. Demonstrated the use of an ionic current collector to enhance the energy harvesting performance of the P(VDF-TrFE) due to the formation of an electric double layer which increases the capacitance of the device. The resultant TENG device also delivers a self-healing capability.

References

[1] J.-H. Lee, H.-J. Yoon, T. Y. Kim, M. K. Gupta, J. H. Lee, W. Seung, H. Ryu, S.-W. Kim, *Adv. Funct. Mater.* **2015**, *25*, 3203.

[2] Z. L. Wang, *Faraday Discuss.* **2014**, *176*, 447.

Chapter 2

Literature Review

In this chapter, the literature review pertaining to the dissertation work is present. First, the mechanical energy harvesters including piezoelectric and triboelectric energy harvesters is introduced. Various piezoelectric materials were discussed, highlighting the fundamentals and working mechanisms. Further explanations about the piezoelectric polymers, specifically P(VDF-TrFE) and the various mechanisms used to improve its energy harvesting performance are provided. The recent progress made in the P(VDF-TrFE) based mechanical energy harvester are summarized. Finally, the concept of the self-powered device is introduced, and recent progress is highlighted.

2.1 Overview

2.1.1 Energy harvesting technologies

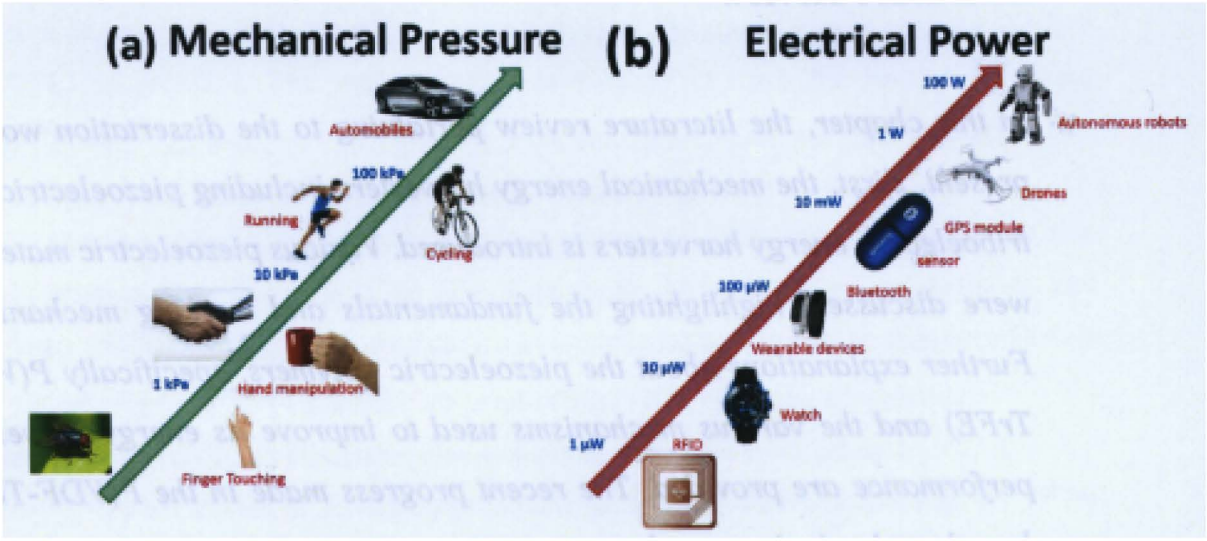

Figure 2.1. (a) The various mechanical forces present in the ambient environment. (b) The power required by the various electronic devices.

The steep decline of fossil fuels and the meteoric rise in global warming in the last half-century have propelled an immense enthusiasm for the development of non-conventional means of energy generation. Based on the Paris Agreement (2015), a global plan is set to limit the global warming by 2 °C. Extensive research is being carried out on various forms of non-conventional energy such as chemical, solar, thermal and mechanical. Among the different forms of non-conventional energy, mechanical energy is a potential candidate due to its availability almost everywhere and at all times in the ambient environment. Figure 2.1a shows the various mechanical forces present in the ambient environment. In this dissertation, the performance of the mechanical energy harvesters is measured at a mechanical pressure of 600 kPa exerted at a frequency of 5 Hz. This is roughly equivalent to pressure exerted by human running wearing sports shoe (with spikes) at a speed of 14 km/h, road racing bicycle going at a speed of 50 km/h, passenger bus going at a speed of 50 km/h, a galloping baby horse, industrial equipment vibrating at 5 Hz frequency. In addition to having an impact on large-scale energy utilization, mechanical energy harvesters can make significant contributions to wearable and personal electronics by

making them self-sustaining and independent. Furthermore, it has huge application in wearable electronics, health monitoring, sports application and sensor networks. Mechanical energy harvesters are best suited for the fabrication of self-powered systems. However, there are very few commercial energy harvesting devices due to the low current density of the device. The key direction is to increase the current density of the device. However, the state-of-the-art device can be utilized to power portable electronics working in the range of few micro to milliWatt/cm^{-2}. These systems can be useful for low-power consumer electronics such as RFID sensor, LEDs, pressure sensors, MSN nodes, remote wireless sensing and cardiac pacemaker, etc. The power required by the various electronic devices are indicated in the Figure 2.1b. Mechanical energy harvester can be of different types such as electrostatic[1], electromagnetic[2], triboelectric and piezoelectric[3] based on the working mechanism. Table 2.1 compares the piezoelectric and triboelectric energy harvesters.

Table 2.1 Comparison of the piezoelectric and triboelectric energy harvesters.

Piezoelectric Energy Harvesters	**Triboelectric Energy Harvesters**
It is based on the generation of potential difference due to the change in the dipole moment in the material on application of mechanical force.	It is based on the generation of potential difference due to the coupling of triboelectric effect and electrostatic effect.
It is based on the intrinsic piezoelectric properties arising due to non-centro symmetry in the crystal structure. Hence the scope of material is limited.	It is based on surface charge effect, observed in all most all the materials. Hence there is a wider choice of synthetic polymers and other insulative materials.
Higher pressure is required to create a dipole moment. Thus a higher pressure is required to generate a voltage.	Voltage can be generated when two polymers can contact and separate, thus it can operate at low pressure.
Can work at a higher frequency, as the dipole moment can response to the higher rate of force application.	Cannot work at a higher frequency, as it is difficult to create contact-separation between polymers at a higher frequency.

Due to inverse piezoelectric effect, can show actuation.	Does not show actuation.
Does not get affected by humidity, thus shows stable performance.	Affected by humidity, thus proper sealing is required.
More tedious preparation method as it requires sophisticated processing procedures such as poling and annealing.	Relatively easy to fabricate.

2.1.2 Piezoelectric energy harvester

The piezoelectric energy harvester is a device which generates a voltage output on the application of mechanical pressure. It consists of a piezoelectric material, which develops a potential difference across the film under stress, called direct piezoelectric effect. Conversely, on the application of an electric field these materials develop a strain, called inverse piezoelectric effect. In this dissertation, piezoelectric material particularly P(VDF-TrFE) is utilized to fabricate mechanical energy harvesters. Figure 2.2 shows the schematic of a piezoelectric energy harvester.

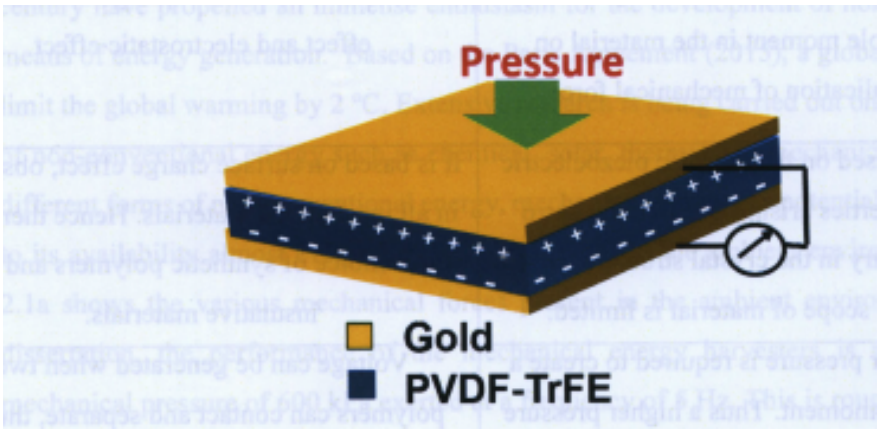

Figure 2.2. Schematic of the piezoelectric energy harvester.

Piezoelectricity materials consist of permanent electric dipoles (positive and negative charges separated by a space). In the case of crystalline inorganic materials such as lead

titania ($PbTiO_3$), barium titanate ($BaTiO_3$) and aluminium nitride (AlN), the dipoles arise from the non-centrosymmetric crystal structure. For organic materials, the difference in the electronegativity of elements attached to the carbon chain creates the electric dipoles. For example, the electric dipole in PVDF material is caused due to the high electronegativity fluorine and electropositive hydrogen attached to the carbon chain. The dipoles are randomly oriented, giving rise to net zero polarization. Upon electrical poling or mechanical stretching, the dipoles can be aligned. On application of force on the aligned piezoelectric polymers, there is a change in the dipole moment, thus creating a potential difference. Equation 1.1, gives the voltage output generated by the piezoelectric energy harvester. Thus, the output performance can be improved by changing the fundamental properties such as piezoelectric coefficient, strain, and dielectric constant.

2.1.3 Triboelectric energy harvester

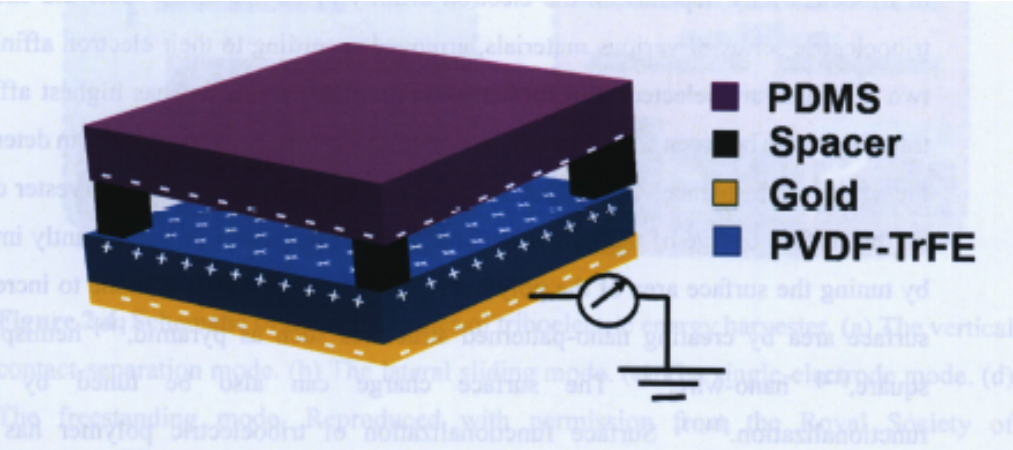

Figure 2.3. Schematic of the triboelectric energy harvester.

The triboelectric energy harvester is a device which generates a voltage output on the application of mechanical force. Energy generation occurs due to the coupling between the triboelectric and electrostatic induction effects.[4–6] It consists of two polymers with different electronegativity, separated by a space, as shown in the Figure 2.3. Before application of mechanical force, the two polymers are not in contact, thus no surface charges. Upon application of mechanical force, the two polymers come in contact with each other. Upon contact, charge transfer takes place from one polymer to the other due to the

difference in their electronegativities. Thus the two polymers acquire triboelectric surface charge with opposite polarity.[6] When the mechanical force is released, the two oppositely charged surfaces (PDMS and P(VDF-TrFE)) become separated in space, thus creating a potential difference. This leads to a transient charge flow from the metal contact to the ground, generating a voltage output. An electrostatic equilibrium is achieved when the two oppositely charged surfaces reach the maximum separation distance. When the mechanical force is reapplied again, the distance between the two polymers as well as their potential difference decrease, resulting in a charge flow in the opposite direction, which generates a voltage in the reverse direction.[7,8] Thus, repeating the procedure described above produces multiple voltage outputs.

Most of the materials known to mankind, can show triboelectric effect. However, intensity of triboelectricity depends on the electron affinity of the material. Table 2.2 shows the triboelectric series of various materials, arranged according to their electron affinity.[9] If two materials are selected with further away from each other, it has highest affinity to transfer charge between each other. Selection of material plays a crucial role in determining the device performance. The output voltage of the triboelectric energy harvester depends on the surface charge of the polymers. The surface charge can be significantly improved by tuning the surface area of the polymer. Extensive work has been done to increase the surface area by creating nano-patterned structures such as pyramid,[10] hemisphere,[11] square,[12] nano-wire.[13] The surface charge can also be tuned by surface functionalization.[14,15] Surface functionalization of triboelectric polymer has shown significant improvement in energy harvesting performance. Capacitance of the materials plays an important role, as it affects the amount of surface charge density. Extensive work has been carried out to tune the capacitance of the material, to increase the surface charge.[16,17] Change in permittivity also affects the energy harvesting performance as it can affect the electrostatic induction.

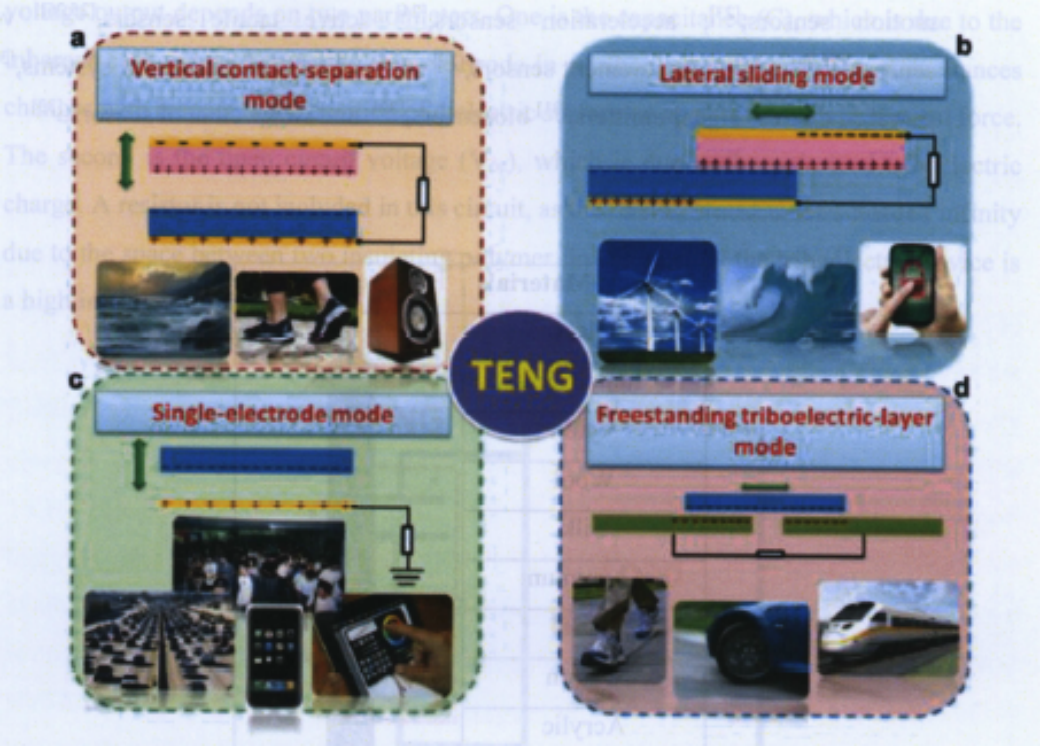

Figure 2.4. Schematic of different modes of triboelectric energy harvester. (a) The vertical contact-separation mode. (b) The lateral sliding mode. (c) The single-electrode mode. (d) The freestanding mode. Reproduced with permission from the Royal Society of Chemistry.[18]

Triboelectric nanogenerator operates in 4 modes or device structure, such as vertical contact-separation mode, in-plane sliding mode, single-electrode mode and free-standing triboelectric-layer mode (Figure 2.4). In this work, single-electrode mode is primarily used. In the single electrode mode, the top polymer layer need not be connected or bonded with an electrode or connecting wide. In this mode, only the bottom electrode is connected to the ground. This mode provides more versatility and applicability as the top layer can move freely without any restriction. This mode is used to generate energy from rain drop,[19] air

flow,[20] and rotating tires.[21] It is more suitable for touch sensor application, as the force can be directly applied by hand or external contact as one of the triboelectric layer. It has been extensively used as various self-powered sensors such as pressure sensors,[22] body motion sensors,[23], acceleration sensors,[24] active tactile sensors,[25,26] velocity sensors,[27,28] angle measurement sensors,[29] self-powered identification systems,[30] self-powered distress signal emitters,[31] biosensors,[32] and water/ethanol sensors.[33]

Table 2.2 Triboelectric series.

Various Materials	Positive Material
Glass	
Human Hair	
Nylon	
Wool	
Silk	
Aluminium	
Paper	
Cotton	
Acrylic	
Polyurethane	
Polypropylene	
Teflon	
Silicone rubber	Negative Material

The first-order lumped-parameter equivalent circuit model of the triboelectric nanogenerator is a voltage source in series with a capacitor as shown in Figure 2.5. The inherent behavior of the triboelectric device is capacitive in nature, thus the governing equation is V–Q–x is used to explain the behavior (equation 2.1).

$$V = -\frac{Q}{C(x)} + V_{oc}(x)$$

where V = the total voltage difference between the two triboelectric electrodes, Q = the transferred charges, C(x) = capacitance between the two electrodes and x= separation distance between two triboelectric layer. From the equation 2.1, we can observe that the voltage output depends on two parameters. One is the capacitance (C), which is due to the inherent capacitance across the two electrode in a triboelectric device. The capacitances changes with respect to the position of dielectric surface on application of mechanical force. The second is the open circuit voltage (V_{oc}), which is due to the polarized triboelectric charge. A resistor is not included in this circuit, as the internal resistance is close to infinity due to the space between two insulating polymer. In conclusion, the triboelectric device is a high impedance charge source.

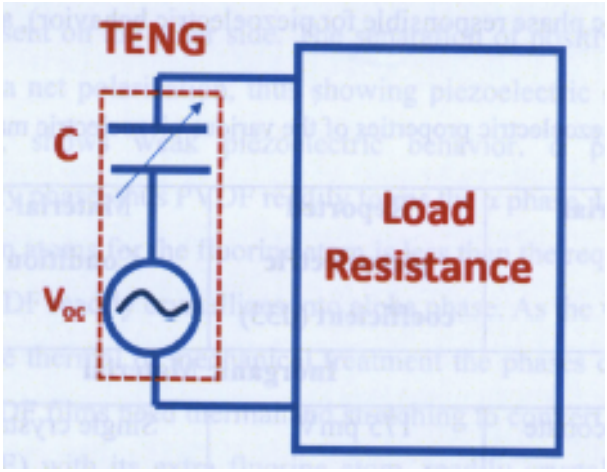

Figure 2.5. First-order lumped-parameter equivalent circuit model of the triboelectric device.

2.1.4 Various piezoelectric materials

Piezoelectric materials can be broadly classified into organic and inorganic materials. In inorganic piezoelectric materials, polarization arises from the non-centrosymmetric crystal structure. Piezoelectric effect was first observed in Rochelle salt. Inorganic piezoelectric materials include inorganic perovskite materials such as $PbZrTiO_3$, $BaTiO_3$, and AlN. Inorganic piezoelectric materials demonstrate excellent polarization (For e.g. piezoelectric coefficient for PZT is around d33 > 100 pC/N). For organic materials, the electric dipoles arise from the difference in the electronegativity of elements attached to the carbon chain as seen in the case of PVDF, where the electric dipole is caused due to the high

electronegativity fluorine and electropositive hydrogen attached to the carbon chain. Organic piezoelectric materials are flexible; thus they can sustain high compressive mechanical stress, strains, and strain rates. The dielectric constant is low compared to the inorganic piezoelectric materials. Moreover, some organic materials are highly transparent, solution processable, low cost, which makes easy industrial adaptability. They are highly chemically and thermally stable. Among the various piezoelectric polymer, PVDF and its copolymers show the highest piezoelectric coefficients (~ 20pC/N). Additionally, it also demonstrates high remnant polarization (8-12 $\mu C/cm^2$) and low coercive field (50 MV/m).[34,35] Table 2.3 shows the piezoelectric properties of the various piezoelectric materials. In this dissertation, P(VDF-TrFE) is used to fabricate a mechanical energy harvester. P(VDF-TrFE) is utilized in this dissertation, as it readily forms β phase (piezoelectric phase responsible for piezoelectric behavior), and it has a higher piezoelectric coefficient.

Table 2.3. Piezoelectric properties of the various piezoelectric materials.

Material	**Reported piezoelectric coefficient (d33)**	**Material Condition**	**Reference**
Inorganic Material			
Lead Zirconate titanate	175 pmV^{-1}	Single crystal	[36]
Barium Titanate (BTO)	85 pmV^{-1}	Single crystal	[37]
Zinc Oxide (ZnO)	45 pmV^{-1}	Single nanowire	
Organic Material			
PVDF	28 pmV^{-1}	High β phase PVDF film	[38]
P(VDF-TrFE) film	20 pmV^{-1}	Spin coated film	[39]
ParyleneC	1–2 pC /N	Thick film	[40]
Nylon-11	3.1 pC /N	Thin film	[41]

2.1.5 Piezoelectric P(VDF-TrFE)

Amongst the various organic piezoelectric materials PVDF and its copolymer P(VDF-TrFE) are extensively explored due to its higher piezoelectric coefficient (values d33 ~ 20 pm/V), high remnant polarization (8-12 $\mu C/cm^2$) and low coercive field (50 MV/m).[34,42,43] P(VDF-TrFE) is a copolymer of PVDF. It shows various conformations, such as α, β and γ phase. In the α phase (the trans–gauche (TGTG) conformation), positively charged hydrogen and negatively charged fluorine atoms are arranged alternatively on one side of the carbon chain. Due to the alternate arrangement of hydrogen and fluorine, it shows net zero dipole moment, thus no piezoelectric effect. In the β phase (all trans (TTTT) conformation), the hydrogen atoms are arranged on one side of the carbon chain, and the fluorine atoms are present on the other side. The separation of positively and negatively charges, gives rise to a net polarization, thus showing piezoelectric effect. γ phase (the TTTG configuration), shows weak piezoelectric behavior. α phase is the most thermodynamic stability phase, thus PVDF readily forms the α phase. In β phase, the space available by two carbon atoms for the fluorine atom is less than the required space. Thus it is unstable, and the PVDF readily crystallizes into alpha phase. As the various phases have similar energies, by the thermal or mechanical treatment the phases can be converted to one another. Thus, PVDF films need thermal and stretching to convert α phase to β phase. However, P(VDF-TrFE) with its extra fluorine atom, readily crystallizes into β phase. Upon copolymerizing the PVDF with TrFE, the bigger fluorine atom replaces the small hydrogen atom. This makes the α phase unstable, thus readily forming β phase. P(VDF-TrFE) is chosen in this study as it readily forms β phase, without any treatment and its shows higher piezoelectric coefficient.

2.1.6 Various methodologies to improve the energy harvesting performance of P(VDF-TrFE)

Voltage output of a piezoelectric energy harvester is given by the following equation 2.2.[44]

$$V = \frac{Y \varepsilon t d_{33}}{\epsilon} \tag{2.2}$$

where V = voltage output, ϵ = dielectric constant, σ = mechanical stress, t = thickness, d_{33} = piezoelectric coefficient, Y = Young's modulus and ε = strain. The voltage output of the triboelectric energy harvester is given by the equation 2.3.[45]

$$V = \frac{\sigma x}{\epsilon} \tag{2.3}$$

where, V = voltage output, ε = permittivity of free space, σ = surface charge density, x = separation distance between the two polymers. The energy harvesting performance of P(VDF-TrFE) can be improved by tuning the intrinsic properties. Various methodologies have been adopted to increase the performance of the P(VDF-TrFE). Few of the approaches are described in detail.

2.1.6.1 Structural modification of P(VDF-TrFE)

The technique of structural modification of P(VDF-TrFE) was adopted to tune the intrinsic properties of the P(VDF-TrFE). For example, buckled piezoelectric ribbons were used to create strain gradient induced polarization. This internal stress showed an enhancement of performance by 70 % compared to that of the compact film. Furthermore, pyramidal shaped micro patterned P(VDF-TrFE) was created, which creates stress concentration at the sharp edges, thus improving the energy harvesting performance compared to that of the compact films.[46] 1-D nanostructures of P(VDF-TrFE) has been explored to create stress confinement in one direction, thus improving the energy harvesting performance. Nanoconfinement also improves the β phase, thus improving the piezoelectric coefficient.[47] This is demonstrated by fabricating P(VDF-TrFE) nanotubes.[47,48] P(VDF-TrFE) nanostructures can also be created by electrospinning. The application of a strong electric field along with mechanical stretching during the electrospinning process enhances the β content, thus improving the performance. This process also creates enhanced crystallinity with higher piezoelectric coefficient.[49–52]

2.1.6.2 Composites piezoelectric materials for mechanical energy harvesters.

Extensive work has been done to fabricate composite based piezoelectric energy harvester. Inorganic materials such as PZT and BTO have higher piezoelectric coefficient than organic material, thus by combining the inorganic and organic materials, higher energy harvesting performance can be achieved. Incorporation of nanostructured inorganic materials into PVDF improves strain bearing ability of the material and thus improve the performance. Additionally, incorporation of inorganic material into PVDF films, enhances the β phase. For example non-piezoelectric materials such as Ag-Graphene, [53] Cerium, [54] and DNA[54] has been incorporated into PVDF, to enhance the energy harvesting performance by increasing the β phase content. Ferroelectric polarized graphene electrodes were used as effective charge collection layer in P(VDF-TrFE) films.[47,55] Some of the key works done on P(VDF-TrFE) are highlighted in Table 2.4.

Table 2.4. Summary of the recent work on P(VDF-TrFE) based mechanical energy harvesters.

Work done on PVDF-TrFE	V out	I out	Contribution	Reference
-Direct write P(VDF-TrFE) fiber -Stretching at a freq of 2Hz	5- 30 mV	0.5 – 3 nA	- nano fiber mat of PVDF-TrFE fabricated by electro spinning - first energy harvesting paper on PVDF-TrFE	[50]
-P(VDF-TrFE) with graphene electrode -Bending at a strain = 0.081%	4 V	0.4-0.2 $\mu A/m^2$	increase the carrier concentration of the graphene by poling	[56]
-P(VDF-TrFE) fiber -Vibrated at a freq of 2.6Hz	0.6 V	-	- applied electrospinning-method	[57]
-Gold nanoparticle -Bending test	280 mV	-	-Gold nano particle electrode used to increase the surface area of the gold contact	[58]
-Graphene multilayer film -Bending with a strain rate of	3 V	0.37 $\mu A/cm^2$	- increase the carrier concentration of the graphene by poling	[59]

60mm/s and with a strain value of 0.3%				
-spring type Device -Compression force of 17.4N	88 mV	-	-demonstrate a new spring type device structure, coated with PVDF-TrFE	[60]
-Aligned nanofiber -Bending test at 1Hz	1 V	30 nA	-Highly sensitive pressure sensor demonstrated -fabricated freestanding array of aligned nano fiber of PVDF-TrFE	[51]
-Surface controlled porous structure -Bending test at 1Hz	2 V	300 nA	-enhancement voltage output due to surface compressibility	[61]
-Sandwich structure of (graphene-P(VDF-TrFE) – CNT) -Stretching	0.7 V	-	-demonstrate the combined effect of piezoelectric and pyroelectric	[62]
-P(VDF-TrFE) nanotube -Pressure of 75 kPa at a freq of 1Hz	4.8 V	-	-Higher voltage output due to confinement effect -Higher piezoelectric coefficient	[47]
-Flexible P(VDF-TrFE) on PET substrate -Bending at a freq of 0.75 Hz and at a strain magnitude of 0.943%	7 V	58 nA	- Highest voltage output report so far - However effective working area of the device is very small so the current density is very small	[63]
Self-poled P(VDF-TrFE) nanotube	3 V	6 nA	- Confined geometry leads to oriented crystallization and self-poling.	[48]
solvent annealed P(VDF-TrFE) film	8V	0.4 μAcm^{-2}	- solvent annealing leads to well aligned electrical dipoles.	[64]

2.1.7 Self-powered devices

Self-powered, interactive, maintenance-free, and multifunctional operations are the key requirements for the realization of the next-generation electronics devices. A self-powered system consists of an energy harvesting unit (which harvest energy from the ambient energy), an energy storage unit (which stores the generated energy) and an energy utilization unit (which utilizes the energy). Figure 2.6 shows the schematic of the self-powered system.

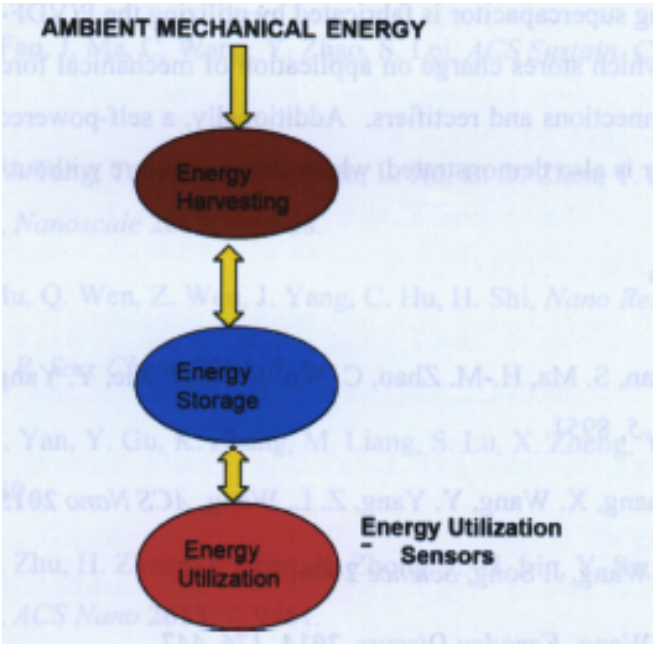

Figure 2.6. Schematic of the self-powered system.

Recently, humongous endeavors have been made to fabricate a self-powered system. Several recent reports show the discrete integration of mechanical energy harvester with electrochemical devices like a supercapacitor,[65] electrochromic and batteries.[66] The piezoelectric energy harvester has also been utilized to power sensors,[67–70]cardiac pacemaker,[71] and wireless data transmission system.[72] However, the mechanical energy harvester is connected to the other electronics components by external electrical connections and rectifiers, which results in the huge loss of energy and eventually decreases the amount of energy utilized or stored. This issue can be resolved by functional integration

of devices, where the single device performs both the energy harvesting, energy storage, and energy utilization function. An integrated self-charged battery system has also been demonstrated where the piezoelectric PVDF material is used as a separator in order to drive the ion across the battery electrode.[73–75] However, the charging time of the battery is very high, which takes about 5 minutes to increase a potential of 200 mV. As the increment in the voltage of the battery during charging is very low (maximum 300 mV), so it cannot be utilized for practical application. Thus, a tremendous potential exists for the possibility of increasing the voltage to a higher potential and in a lesser time. In this dissertation, a fast self-charging supercapacitor is fabricated by utilizing the P(VDF-TrFE) as a piezoelectric-separator, which stores charge on application of mechanical force without the use of any external connections and rectifiers. Additionally, a self-powered pressure sensor and the touch sensor is also demonstrated, which detect pressure without external power supply.

References

[1] H. Tian, S. Ma, H.-M. Zhao, C. Wu, J. Ge, D. Xie, Y. Yang, T.-L. Ren, *Nanoscale* **2013**, *5*, 8951.

[2] K. Zhang, X. Wang, Y. Yang, Z. L. Wang, *ACS Nano* **2015**, *9*, 3521.

[3] Z. L. Wang, J. Song, *Science* **2006**, *312*, 242.

[4] Z. L. Wang, *Faraday Discuss.* **2014**, *176*, 447.

[5] Z. L. Wang, J. Chen, L. Lin, *Energy Environ. Sci.* **2015**, *8*, 2250.

[6] Y.-C. Lai, J. Deng, S. Niu, W. Peng, C. Wu, R. Liu, Z. Wen, Z. L. Wang, *Adv. Mater.* **2016**, *28*, 10024.

[7] J. Chun, J. W. Kim, W. Jung, C.-Y. Kang, S.-W. Kim, Z. L. Wang, J. M. Baik, *Energy Environ. Sci.* **2015**, *8*, 3006.

[8] S. Wang, L. Lin, Z. L. Wang, *Nano Energy* **2015**, *11*, 436.

[9] J.-H. Lee, R. Hinchet, T. Y. Kim, H. Ryu, W. Seung, H.-J. Yoon, S.-W. Kim, *Adv. Mater.* **2015**, *27*, 5553.

[10] F.-R. Fan, L. Lin, G. Zhu, W. Wu, R. Zhang, Z. L. Wang, *Nano Lett.* **2012**, *12*, 3109.

[11] K. Y. Lee, H. Yoon, T. Jiang, X. Wen, W. Seung, S. Kim, Z. L. Wang, **2016**, DOI 10.1002/aenm.201502566.

[12] Y. Zhu, B. Yang, J. Liu, X. Wang, L. Wang, X. Chen, C. Yang, **2016**, *6*, 22233.

[13] Y. Feng, Y. Zheng, S. Ma, D. Wang, F. Zhou, W. Liu, *Nano Energy* **2016**, *19*, 48.

[14] Y. Yu, X. Wang, *Extrem. Mech. Lett.* **2016**, *9*, 514.

[15] X. Ren, H. Fan, J. Ma, C. Wang, Y. Zhao, S. Lei, *ACS Sustain. Chem. Eng.* **2017**, *5*, 1957.

[16] J. J. Shao, W. Tang, T. Jiang, X. Y. Chen, L. Xu, B. D. Chen, T. Zhou, C. R. Deng, Z. L. Wang, *Nanoscale* **2017**, *9*, 9668.

[17] X. He, X. Mu, Q. Wen, Z. Wen, J. Yang, C. Hu, H. Shi, *Nano Res.* **2016**, *9*, 3714.

[18] Z. L. Wang, *R. Soc. Chem.* **2014**, *0*, 1.

[19] Q. Liang, X. Yan, Y. Gu, K. Zhang, M. Liang, S. Lu, X. Zheng, Y. Zhang, *Sci. Rep.* **2015**, *5*, 9080.

[20] Y. Yang, G. Zhu, H. Zhang, J. Chen, X. Zhong, Z.-H. Lin, Y. Su, P. Bai, X. Wen, Z. L. Wang, *ACS Nano* **2013**, *7*, 9461.

[21] H. Zhang, Y. Yang, X. Zhong, Y. Su, Y. Zhou, C. Hu, Z. L. Wang, *ACS Nano* **2014**, *8*, 680.

[22] P.-K. Yang, Z.-H. Lin, K. C. Pradel, L. Lin, X. Li, X. Wen, J.-H. He, Z. L. Wang, *ACS Nano* **2015**, *9*, 901.

[23] F. Yi, L. Lin, S. Niu, P. K. Yang, Z. Wang, J. Chen, Y. Zhou, Y. Zi, J. Wang, Q. Liao, Y. Zhang, Z. L. Wang, *Adv. Funct. Mater.* **2015**, *25*, 3688.

[24] H. Zhang, Y. Yang, Y. Su, J. Chen, K. Adams, S. Lee, C. Hu, Z. L. Wang, *Adv. Funct. Mater.* **2014**, *24*, 1401.

[25] Y. Yang, H. Zhang, Z.-H. Lin, Y. S. Zhou, Q. Jing, Y. Su, J. Yang, J. Chen, C. Hu, Z. L. Wang, *ACS Nano* **2013**, *7*, 9213.

[26] G. Zhu, W. Q. Yang, T. Zhang, Q. Jing, J. Chen, Y. S. Zhou, P. Bai, Z. L. Wang, *Nano Lett.* **2014**, *14*, 3208.

[27] F. Yi, L. Lin, S. Niu, J. Yang, W. Wu, S. Wang, Q. Liao, Y. Zhang, Z. L. Wang, *Adv. Funct. Mater.* **2014**, *24*, 7488.

[28] Y. Su, G. Zhu, W. Yang, J. Yang, J. Chen, Q. Jing, Z. Wu, Y. Jiang, Z. L. Wang, *ACS Nano* **2014**, *8*, 3843.

[29] Y. Wu, Q. Jing, J. Chen, P. Bai, J. Bai, G. Zhu, Y. Su, Z. L. Wang, *Adv. Funct. Mater.* **2015**, *25*, 2166.

[30] P. Bai, G. Zhu, Q. Jing, Y. Wu, J. Yang, J. Chen, J. Ma, G. Zhang, Z. L. Wang, *Nano Energy* **2015**, *12*, 278.

[31] Y. Su, X. Wen, G. Zhu, J. Yang, J. Chen, P. Bai, Z. Wu, Y. Jiang, Z. L. Wang, *Nano Energy* **2014**, *9*, 186.

[32] H. Zhang, Y. Yang, T.-C. Hou, Y. Su, C. Hu, Z. L. Wang, *Nano Energy* **2013**, *2*, 1019.

[33] P. Bai, G. Zhu, Q. Jing, J. Yang, J. Chen, Y. Su, J. Ma, G. Zhang, Z. L. Wang, *Adv. Funct. Mater.* **2014**, *24*, 5807.

[34] S. Horiuchi, Y. Tokura, *Nat Mater* **2008**, *7*, 357.

[35] A. J. Lovinger, *Science (80-.).* **1983**, *220*, 1115.

[36] R. C. W. Tsang, K. W. Kwok, H. L. W. Chan, C. L. Choy, *Integr. Ferroelectr.* **2002**, *50*, 143.

[37] D. Berlincourt, H. Jaffe, *Phys. Rev.* **1958**, *111*, 143.

[38] C. S. Lynch, *Ferroelectrics* **1993**, *150*, 331.

[39] V. Bhavanasi, D. Y. Kusuma, P. S. Lee, *Adv. Energy Mater.* **2014**, *4*, 1.

[40] J. Y. H. Kim, A. Cheng, Y. C. Tai, *2011 IEEE 24th Int. Conf. Micro Electro Mech. Syst.* **2011**, 473.

[41] J. Su, Z. Y. Ma, J. I. Scheinbeim, B. A. Newman, *J. Polym. Sci. Part B Polym. Phys.* **1995**, *33*, 85.

[42] D. Y. Kusuma, C. A. Nguyen, P. S. Lee, *J. Phys. Chem. B* **2010**, *114*, 13289.

[43] C.-C. Hong, P. Huang, J. Shieh, *Macromolecules* **2010**, *43*, 7722.

[44] K. S. Ramadan, D. Sameoto, S. Evoy, *Smart Mater. Struct.* **2014**, *23*, 33001.

[45] Z. L. Wang, J. Chen, L. Lin, *Energy Environ. Sci.* **2015**, *8*, 2250.

[46] J.-H. Lee, H.-J. Yoon, T. Y. Kim, M. K. Gupta, J. H. Lee, W. Seung, H. Ryu, S.-W. Kim, *Adv. Funct. Mater.* **2015**, *25*, 3203.

[47] V. Bhavanasi, D. Y. Kusuma, P. S. Lee, *Adv. Energy Mater.* **2014**, *4*.

[48] R. A. Whiter, V. Narayan, S. Kar-Narayan, *Adv. Energy Mater.* **2014**, *4*, 1.

[49] J. Fang, X. Wang, T. Lin, *J. Mater. Chem.* **2011**, *21*, 11088.

[50] C. Chang, V. H. Tran, J. Wang, Y. K. Fuh, L. Lin, *Nano Lett.* **2010**, *10*, 726.

[51] L. Persano, C. Dagdeviren, Y. Su, Y. Zhang, S. Girardo, D. Pisignano, Y. Huang, J. A. Rogers, *Nat. Commun.* **2013**, *4*, 1633.

[52] C. Sun, J. Shi, D. J. Bayerl, X. Wang, *Energy Environ. Sci.* **2011**, *4*, 4508.

[53] S. Garain, S. Jana, T. K. Sinha, D. Mandal, *ACS Appl. Mater. Interfaces* **2016**, *8*, 4532.

[54] S. Garain, T. K. Sinha, P. Adhikary, K. Henkel, S. Sen, S. Ram, C. Sinha, D. Schmeißer, D. Mandal, *ACS Appl. Mater. Interfaces* **2015**, *7*, 1298.

[55] W. H. Liew, M. S. Mirshekarloo, S. Chen, K. Yao, F. E. H. Tay, **2015**, *5*, 9790.

[56] J. H. Lee, K. Y. Lee, B. Kumar, N. T. Tien, N. E. Lee, S. W. Kim, *Energy Environ. Sci.* **2012**, 169.

[57] S. Dey, M. Purahmad, S. S. Ray, A. L. Yarin, M. Dutta, *2012 IEEE Nanotechnol.*

Mater. Devices Conf. IEEE NMDC 2012 **2012**, 21.

[58] D. Chen, T. Sharma, Y. Chen, X. Fu, J. X. J. Zhang, *8th Annu. IEEE Int. Conf. Nano/Micro Eng. Mol. Syst.* **2013**, *1*, 669.

[59] S. Bae, O. Kahya, B. K. Sharma, J. Kwon, H. J. Cho, *ACS Nano* **2013**, 3130.

[60] D. Kim, S. Hong, D. Li, H. S. Roh, G. Ahn, J. Kim, M. Park, J. Hong, T. Sung, K. No, *RSC Adv.* **2013**, *3*, 3194.

[61] D. Chen, T. Sharma, J. X. J. Zhang, *Sensors Actuators, A Phys.* **2014**, *216*, 196.

[62] J. H. Lee, K. Y. Lee, M. K. Gupta, T. Y. Kim, D. Y. Lee, J. Oh, C. Ryu, W. J. Yoo, C. Y. Kang, S. J. Yoon, J. B. Yoo, S. W. Kim, *Adv. Mater.* **2014**, *26*, 765.

[63] Z. Pi, J. Zhang, C. Wen, Z. B. Zhang, D. Wu, *Nano Energy* **2014**, *7*, 33.

[64] Y. Cho, J. B. Park, B.-S. Kim, J. Lee, W.-K. Hong, I.-K. Park, J. E. Jang, J. I. Sohn, S. Cha, J. M. Kim, *Nano Energy* **2015**, *16*, 524.

[65] L. Yuan, X. Xiao, T. Ding, J. Zhong, X. Zhang, Y. Shen, B. Hu, Y. Huang, J. Zhou, Z. L. Wang, *Angew. Chemie - Int. Ed.* **2012**, *51*, 4934.

[66] X. Yang, G. Zhu, S. Wang, R. Zhang, L. Lin, W. Wu, Z. L. Wang, *Energy Environ. Sci.* **2012**, *5*, 9462.

[67] G. Kettlgruber, M. Kaltenbrunner, C. M. Siket, R. Moser, I. M. Graz, R. Schwödiauer, S. Bauer, *J. Mater. Chem. A* **2013**, *1*, 5505.

[68] H. S. Lee, J. Chung, G. Hwang, C. K. Jeong, Y. Jung, J. Kwak, H. Kang, M. Byun, W. D. Kim, S. Hur, S. Oh, K. J. Lee, **2014**, 6914.

[69] S. Jung, J. H. Kim, J. Kim, S. Choi, J. Lee, I. Park, T. Hyeon, D. H. Kim, *Adv. Mater.* **2014**, *26*, 4825.

[70] Z. H. Lin, G. Zhu, Y. S. Zhou, Y. Yang, P. Bai, J. Chen, Z. L. Wang, *Angew. Chemie - Int. Ed.* **2013**, *52*, 5065.

[71] G. T. Hwang, H. Park, J. H. Lee, S. Oh, K. Il Park, M. Byun, H. Park, G. Ahn, C. K. Jeong, K. No, H. Kwon, S. G. Lee, B. Joung, K. J. Lee, *Adv. Mater.* **2014**, *26*,

4880.

[72] Y. Hu, Y. Zhang, C. Xu, L. Lin, R. L. Snyder, Z. L. Wang, *Nano Lett.* **2011**, 2572.

[73] X. Xue, S. Wang, W. Guo, Y. Zhang, Z. L. Wang, *Nano Lett.* **2012**, *12*, 5048.

[74] X. Xue, P. Deng, S. Yuan, Y. Nie, B. He, L. Xing, Y. Zhang, *Energy Environ. Sci.* **2013**, *6*, 2615.

[75] X. Xue, P. Deng, B. He, Y. Nie, L. Xing, Y. Zhang, Z. L. Wang, *Adv. Energy Mater.* **2014**, *4*, 1.

Chapter 3

Experimental Methodology

In this chapter, methodology to prepare the porous, self-poled and compact P(VDF-TrFE) film is explained. The vapor induced phase separation (VIPS) method adopted to prepare the porous P(VDF-TrFE) film and the modified vapor induced phase separation method developed to prepare the self-poled porous P(VDF-TrFE) film is described in detail. The preparation methodology of freestanding PDMS film and PVA slime based ionic current collector is also described. Detailed explanation is provided for the fabrication of the piezoelectric and triboelectric energy harvester. The energy harvesting measurements of the mechanical energy harvester is described in detail. General characterization such as the mechanical and electrical characterization of the materials and devices used in this dissertation are explained in detail.

3.1 Rationale for selection of materials

The piezoelectric polymer is used in this dissertation due to its inherent polarization and higher surface charge. Additionally, the piezoelectric polymer can sustain higher stress, strain and strain rate compared to inorganic piezoelectric materials. Among the various piezoelectric polymers, P(VDF-TrFE) is selected in this dissertation due to its high piezoelectric coefficients compared to other piezoelectric polymers.[1,2] P(VDF-TrFE) readily forms piezoelectric β phase, without any external treatment due to the presence of an extra fluorine atom. P(VDF-TrFE) is flexible, rollable, and transparent, thus making it suitable for multifunctional operations.[3,4] It is also chemically stable and can absorb electrolyte, thus suitable for self-powered device applications.[5,6] Moreover, it is easy to process, making it scalable and industrial adoptable. Polydimethylsiloxane (PDMS) was used as the triboelectric negative material due to it higher electronegativity as compared to P(VDF-TrFE).[7–9] PDMS is considered as one of the best triboelectric negative material. Poly(vinyl alcohol) (PVA) polymer matrix is selected for the fabrication of ionic current collector due to its non-toxicity, biocompatibility, high ionic conductivity and high transparency.

3.2 Typical experimental procedure

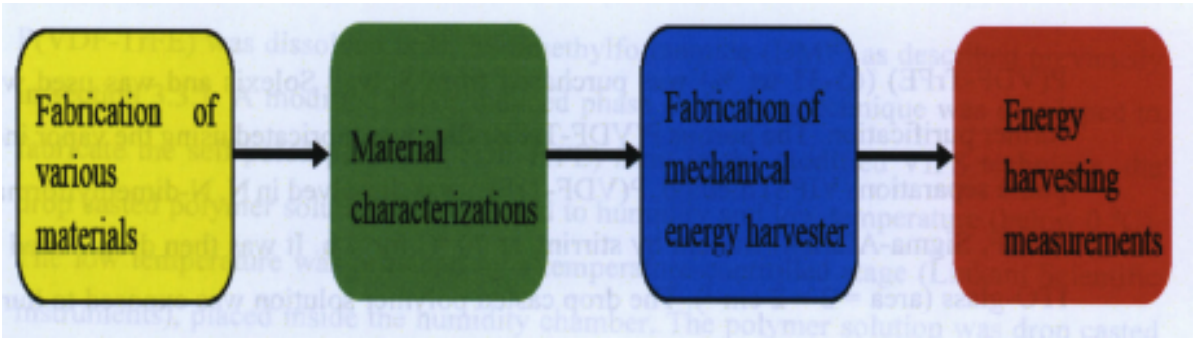

Figure 3.1. Experimental protocol followed in this dissertation.

Figure 3.1 depicts the flowchart of the experimental protocol adopted in this dissertation. The first step was to prepare the material used in this dissertation. Specifically, porous P(VDF-TrFE), self-poled porous P(VDF-TrFE), PDMS and PVA slime were prepared. This is followed by material structural, mechanical and electrical characterization. After

optimizing the required material, the mechanical energy harvester was fabricated. This was followed by measuring the energy harvesting performance of the device. Finally, a self-powered device was fabricated.

3.3 Fabrication

3.3.1 Preparation of the porous P(VDF-TrFE) films

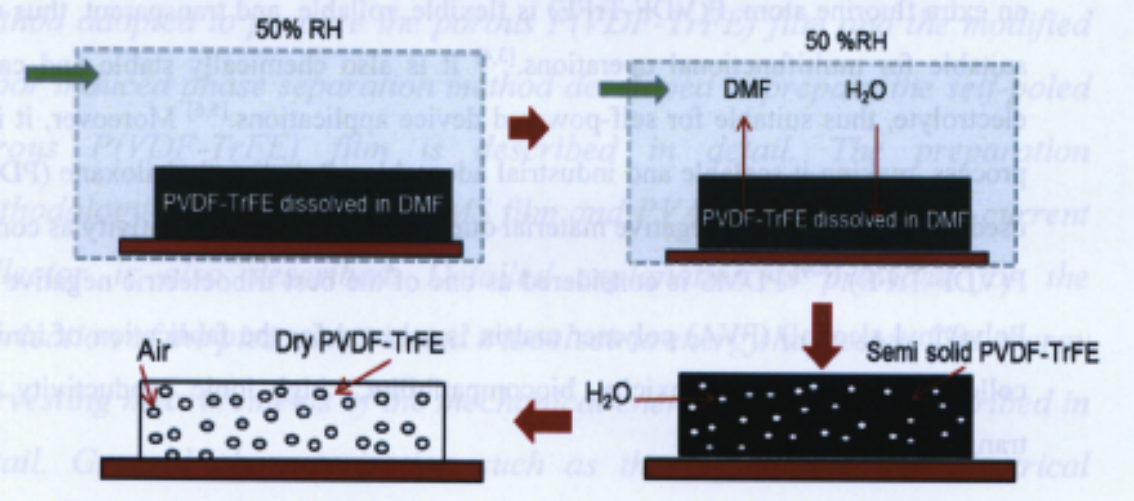

Figure 3.2. Schematic representation of the fabrication of the porous P(VDF-TrFE) film.

P(VDF-TrFE) (65-35 wt %) was purchased from Solvay Solexis and was used without further purification. The porous P(VDF-TrFE) film was fabricated using the vapor induced phase separation (VIPS) method. P(VDF-TrFE) was dissolved in N, N-dimethylformamide (DMF, Sigma-Aldrich) solvent by stirring at 70 °C for 4 h. It was then drop casted on an ITO-glass (area = 2 × 2 cm^{-2}). The drop casted polymer solution was exposed to humidity by placing it inside a humidity chamber (ETS humidity controller 5200). The humidity of the chamber was varied to control the porosity of the film. The film was removed from the humidity chamber after a semi-solid film was formed. It was then dried at room temperature by keeping it in a fume hood. It forms a porous polymer film after 6 h of drying. The porous film was subsequently annealed at 140 °C for 2 h in an oven. Annealing ensures the formation of β phase and the removal of residual water. To make contacts, gold was

sputtered onto the film. Finally, the porous P(VDF-TrFE) film was electrically poled by applying an electric field of 20 V/μm at 100 °C to align the electric dipoles. Figure 3.2 depicts the schematic representation of the fabrication of the porous P(VDF-TrFE) film.

3.3.2 Preparation of the self-polarized porous P(VDF-TrFE) films

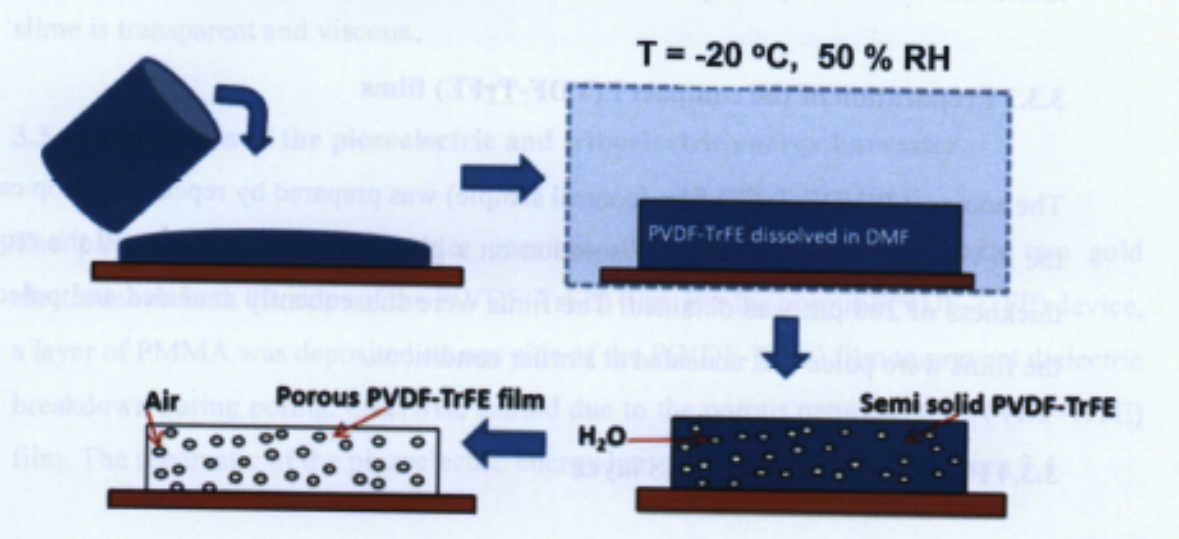

Figure 3.3. Schematic representation of the fabrication of the self-poled porous P(VDF-TrFE) film.

P(VDF-TrFE) was dissolved in N, N-dimethylformamide (DMF) as described previously in section 3.3.1. A modified vapor induced phase separation technique was developed to fabricate the self-poled porous P(VDF-TrFE) film. In the modified VIPS technique, the drop casted polymer solution was exposed to humidity and low temperature (below 0 °C). The low temperature was provided by a temperature-controlled stage (Linkam Scientific Instruments), placed inside the humidity chamber. The polymer solution was drop casted onto a glass slide (area = 2 × 2 cm^{-2}) and placed on the temperature-controlled stage inside the humidity chamber. A temperature of -20°C and a 50 % relativel humidity (RH) were maintained until a semi-solid film was formed (approximately 1 h). The film was subsequently removed from the humidity chamber and air dried for 6 h at room temperature until all the absorbed water was removed, and a porous white sponge was formed. The

sponge was peeled off from the glass to obtain a free-standing, flexible self-poled P(VDF-TrFE) sponge. To understand the mechanism of self-polarization, P(VDF-TrFE) films were fabricated at various temperature and humidity. The temperature was varied using the temperature-controlled stage, and the humidity was varied using the humidity chamber. The thickness and area of all the P(VDF-TrFE) films fabricated at various conditions were 200 $\pm$ 10 μm and 2 × 2 cm^{-2} respectively. Figure 3.3 depicts the schematic representation of the fabrication of the self-poled porous P(VDF-TrFE) film.

3.3.3 Preparation of the compact P(VDF-TrFE) films

The compact P(VDF-TrFE) film (control sample) was prepared by repeatedly drop casting the P(VDF-TrFE) dissolved DMF solution on a glass slide (2 × 2 cm^{-2}), till the required thickness of 200 μm was obtained. The films were subsequently annealed and poled. All the films were poled and annealed at similar conditions.

3.3.4 Preparation of the PDMS layer

To prepare the PDMS layer, commercial PDMS (Sylgard 184, Dow Corning, USA) base and curer were thoroughly mixed in a weight ratio of 10:1. It was subsequently, cured at 60 °C for 2 h. The PDMS layer was peeled off from the substrate, to obtain a freestanding layer.

3.3.5 Preparation of ionic conductor

Borax cross-linked PVA slime was used as the ionic conductor. PVA (average Mw 130,000, >99% hydrolyzed, Sigma-Aldrich) and Sodium tetraborate (Sigma-Aldrich) were used without purification. The 10 wt % PVA solution was prepared by slowly adding PVA powder to DI water maintained at a temperature of 80 °C while stirred vigorously. Slow adding ensures individual wetting of polymer grains. A viscous and clear solution was obtained after 3 h of stirring at 80 °C. 4 wt % borax solution was separately prepared by mixing hydrated sodium tetraborate ($Na_2B_4O_7.10H_2O$) in DI water. Borax solution was

added to the PVA solution in a mixture of 10:1 (PVA:borax) volumetric ratio, while vigorously stirring with a spatula until the mixture was complete gelled. A lesser amount of borax, will partially cross link the polymer, thus making an inconsistent slime. Moreover, the addition of higher amount of borax solution will further increase the cross-linking of polymer, which increases the viscosity of the slime. Higher viscosity will hinder the viscoelastic flow of the slime upon stretching. Thus, a volumetric ratio of 10:1 (PVA: Borax) was used to get a consistent, high ionically conducting and viscoelastic slime. The obtained slime is transparent and viscous.

3.3.6 Fabrication of the piezoelectric and triboelectric energy harvester

The piezoelectric energy harvester consists of a sandwich structure, with two gold electrodes on both the sides of the P(VDF-TrFE) film. For the porous P(VDF-TrFE) device, a layer of PMMA was deposited on one side of the P(VDF-TrFE) film to prevent dielectric breakdown during poling, otherwise caused due to the porous nature of the P(VDF-TrFE) film. The schematic of the piezoelectric energy harvester is shown in the Figure 3.4.

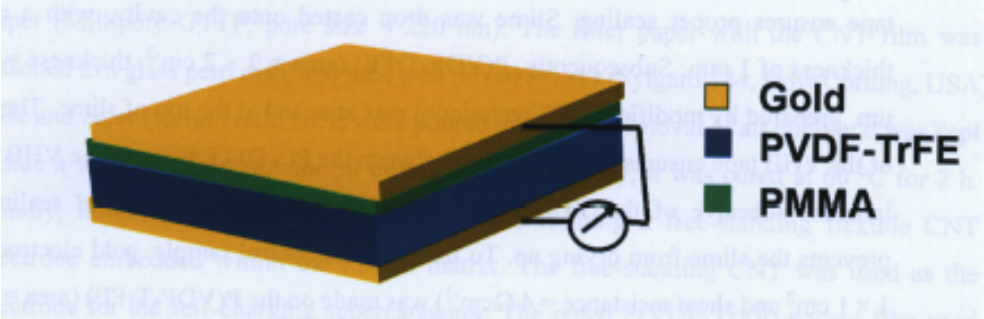

Figure 3.4. Schematic diagram of the piezoelectric energy harvester.

The triboelectric energy harvester consists of two polymers separated by a spacer. The schematic of the triboelectric energy harvester is shown in the Figure 2.3. As shown in the Figure 2.3, it consists of two layers: (i) A P(VDF-TrFE) film with gold electrodes (thickness = 30 nm, area = 1 × 1 cm^2) on one side. (ii) A freestanding PDMS film. The two layers were separated by a spacer (a commercial elastic tape (3M VHB 4910), thickness = 2 mm). The elastic nature of the spacer, allows the two polymer layers to separate when the force

is released. The gold electrodes were connected to one terminal of the measuring instrument, while the other terminal of the measuring instrument was connected to the ground. The device was sealed by applying a thin layer of silicone rubber to the junction between the PDMS and the spacer (VHB tape). This prevents the water vapor from interacting with the triboelectric surface of the PDMS and PVDF-TrFE, thus ensuring stable performance.

3.3.7 Fabrication of triboelectric energy harvester with ionic current collector

Figure 3.5 schematically illustrates the detailed fabrication process of the TENG with ionic current collector. The TENG consists of PVA slime (ionic current collector) sandwich between P(VDF-TrFE) and VHB tape. VHB tape (VHB 4010, 3M, USA) was used as the substrate (area = 2 × 2 cm^{-2}, thickness = 1 mm). A conducting wire was attached to the substrate as shown in Figure 3.6. To ensure proper encapsulation and sealing of the slime, a cavity (area = 1 × 1 cm^2, thickness = 1 mm) was made by sticking one more layer of VHB tape (with a rectangular hole in the center) onto the substrate. The adhesive of the VHB tape ensures proper sealing. Slime was drop casted onto the cavity, with a controlled thickness of 1 mm. Subsequently, P(VDF-TrFE) (area = 2 × 2 cm^{-2}, thickness = 200 ± 10 μm, prepared by modified VIPS technique) was attached at the top of slime. The adhesive of the VHB tape ensures good adhesion between the P(VDF-TrFE) and the VHB tape. The inherent adhesive of the VHB tape ensures proper encapsulation and sealing, which prevents the slime from drying up. To fabricate the control sample, gold electrode (area = 1 × 1 cm^2 and sheet resistance = 4 Ωcm^{-1}) was made on the P(VDF-TrFE) (area = 2 × 2 cm^{-2}, thickness = 100 ± 20 μm, prepared by modified VIPS method). Copper tape was used to connect the gold electrode to the measuring instrument.

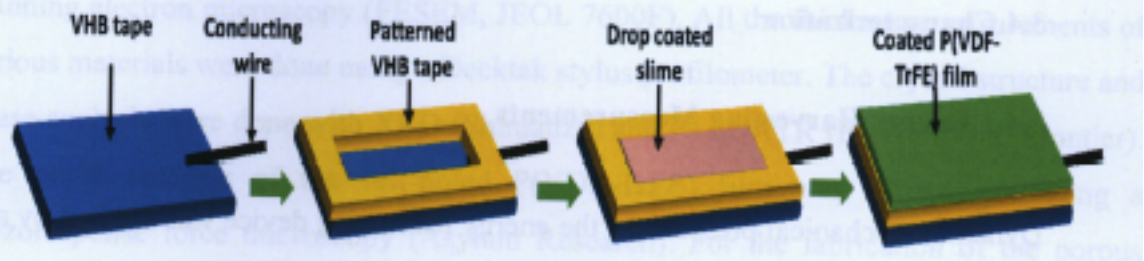

Figure 3.5. Schematic diagram of the fabrication process of the TENG with the ionic conductor as the current collector.

3.3.8 Fabrication of the self-charging supercapacitor

The poled porous P(VDF-TrFE) film was used as the separator (sandwich between the CNT electrodes) to fabricate the self-charging supercapacitor. Vacuum filtration method was adopted to fabricate the highly flexible CNT electrodes.[10] The SWCNT (Time Nano, China, Product Number: TNGMC2) was purchased commercially. The SWCNT with a concentration of 3 wt % and cellulose binder with a concentration of 5wt % were mixed in a ratio of 4:1. The CNT film was formed by vacuum filtration method using a PC filter paper (Millipore GTTP, pore size = 220 nm). The filter paper with the CNT film was attached to a glass petri dish, and then well mixed PDMS (Sylgard 184, Dow Corning, USA) base and curer (weight ratio 10:1) were poured in. For the removal of air bubble, it was kept inside a vacuum desiccator for 30 minutes. Subsequently, it was cured at 60 °C for 2 h. Finally, it was peeled off from the petri dish, forming a free-standing flexible CNT electrode embedded within the PDMS matrix. The free-standing CNT was used as the electrode for the self-charging supercapacitor. The poled P(VDF-TrFE) porous film used as the separator was immersed in the PMMA/$LiClO_4$/PC based gel electrolyte and then placed between the electrodes. The porous P(VDF-TrFE) porous film was used after removing the gold contacts by etching. The SP-EDLC was assembled in a pouch cell. To prevent any leakage, the SP-EDLC was properly sealed.

3.4 Characterization

3.4.1 Energy Harvesting Measurements

Dynamic mechanical pressure on the energy harvesting device was applied by a magnetic shaker (Sinocera, Model JZK-20). The pressure exerted on the device was measured using a force gauge (Mark-10, Model M7-025, for low-pressure range) and (Sinocera, Model CY-YD-303, for a medium and high-pressure range). The voltage output generated from the mechanical energy harvester was measured by an oscilloscope (Trektronix, MDO 3024, input resistance = 10 MΩ), the current output was measured by a low-noise current pre-amplifier (Stanford Research System, Model SR570, input resistance = 4 Ω) and the charge transfer using the (Keithley 6514 system electrometer, input resistance = 200 TΩ). Figure 3.6 shows the schematic diagram of the measurement setup.

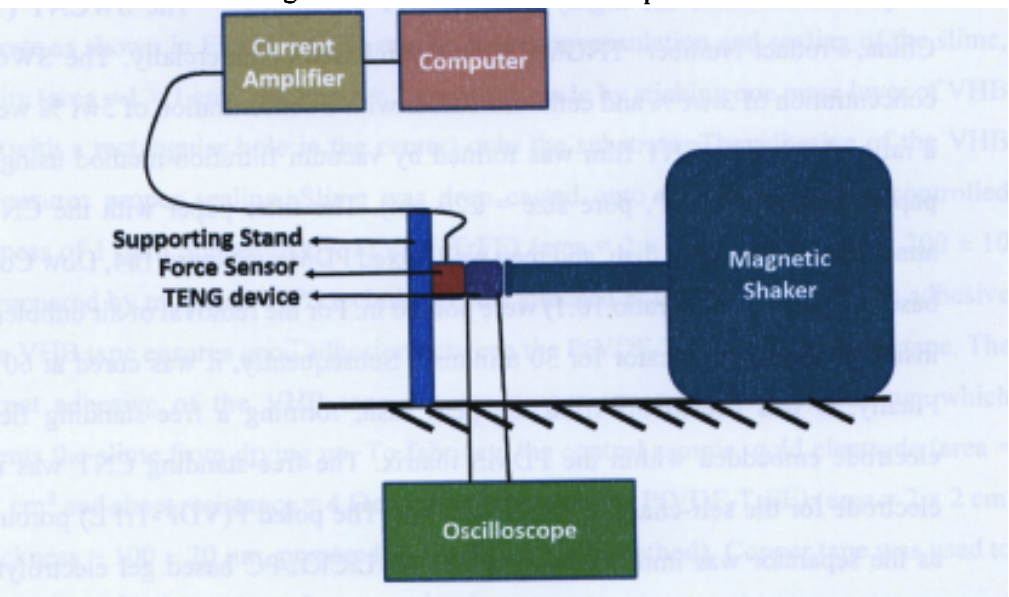

Figure 3.6. Schematic diagram of the measurement setup used to measure the energy harvesting performance.

3.4.2 General characterization

The top and cross-section morphologies of all the samples including the porous and compact P(VDF-TrFE) films and CNT electrodes were measured using a field-emission

scanning electron microscopy (FESEM, JEOL 7600F). All the thickness measurements of various materials were done using a Decktak stylus profilometer. The crystal structure and phase analysis were done with XRD (Shimadzu) and FTIR-ATR (Perkin Elmer Frontier). The phase analysis of the self-poled P(VDF-TrFE) film was carried out using a Piezoresponse force microscopy (Asylum Research). For the fabrication of the porous P(VDF-TrFE) films, humid atmosphere was provided by the humidity chamber (ETS humidity controller 5200). Shimadzu spectrometer (UV-2501pc,) was used to measure the transmittance spectra of the ionic conductor with respect to a glass slide over the range of 300 to 900 nm. Poling of the P(VDF-TrFE) films were done using a constant DC supply system (Kikusui, TOS 5051) voltage tester. All the mechanical measurements including the compressibility of the P(VDF-TrFE) film and mechanical properties of the ionic conductor was measured using a static compression tester (Instron 5576). The electrochemical performance of the SP-EDLC was investigated with (Autolab PGSTAT 30) potentiostat. The electrochemical impedance spectroscopy of the ionic conductor was measured using a potentiostat (Autolab PGSTAT 30), by sandwiching the ionic conductor (area = 1 × 1 cm^{-2}, thickness = 1 mm) between two Indium Tin Oxide (ITO) glass pieces. The sheet resistance measurements were done using a four-probe resistance measurement system (Advance Instrument Technology, CMT-SR2000N). A LCR meter (Agilent E4980A Precision), was used to measure the capacitance and resistance of the ionic conductor at various experimental conditions. The capacitance of the ionic conductor and silicone rubber were measured at a voltage of 0.1 V applied over a frequency range, by sandwiching the materials between two ITO glass pieces. The change in the resistance of the PVA slime (ionic conductor) during bifurcation and self-healing was measured (using the LCR meter), by inserting two metallic wire at the two extreme end of the TENG.

3.4.3 Piezoresponse force microscopy

Piezo Force Microscopy is an analytical tool used to study the piezoelectric and ferroelectric properties. It utilizes the coupling effect of mechanical and electric properties of the piezoelectric and ferroelectric materials. During the measurement, voltage is applied across the PFM tip and the sample, which creates a mechanical displacement due to the

piezoelectric effect. The mechanical displacement is measured (down to pm scale) by using a lock-in amplifier. In this dissertation, PFM was primarily used to observe the domain image of the self-poled and non-poled P(VDF-TrFE) film. To obtain the domain image, a small AC voltage is applied between the tip and the sample to detect the magnitude and phase of the piezoelectric response. The magnitude and phase of the piezoelectric response is detected by the lock-in amplifier. The orientation difference of the piezoelectric domains with respect to the applied signal give rise to the observed contrast in phase image. The amplitude of the image indicates the magnitude of mechanical deflection created by the piezoelectric domain when subjected to the electric field. The measurements are performed in contact mode at a frequency of 50 kHz. AFM tips (NT-MDT, CSG-10 tips) with a resonant frequency of 236 kHz, were used in the measurements.

References

[1] V. Bhavanasi, V. Kumar, K. Parida, J. Wang, P. S. Lee, *ACS Appl. Mater. Interfaces* **2016**, *8*, 521.

[2] A. J. Lovinger, *Science (80-.).* **1983**, *220*, 1115.

[3] V. Bhavanasi, D. Y. Kusuma, P. S. Lee, *Adv. Energy Mater.* **2014**, *4*.

[4] S. Horiuchi, Y. Tokura, *Nat. Mater.* **2008**, *7*, 357.

[5] D. Y. Kusuma, C. A. Nguyen, P. S. Lee, *J. Phys. Chem. B* **2010**, *114*, 13289.

[6] C.-C. Hong, P. Huang, J. Shieh, *Macromolecules* **2010**, *43*, 7722.

[7] J. Chun, B. U. Ye, J. W. Lee, D. Choi, C.-Y. Kang, S.-W. Kim, Z. L. Wang, J. M. Baik, *Nat. Commun.* **2016**, *7*, 12985.

[8] Y. Zhu, B. Yang, J. Liu, X. Wang, L. Wang, X. Chen, C. Yang, **2016**, *6*, 22233.

[9] Y. H. Ko, G. Nagaraju, S. H. Lee, J. S. Yu, *ACS Appl. Mater. Interfaces* **2014**, *6*, 6631.

[10] C. Yan, J. Wang, W. Kang, M. Cui, X. Wang, C. Y. Foo, K. J. Chee, P. S. Lee, *Adv. Mater.* **2014**, *26*, 2022.

Chapter 4

Porous P(VDF-TrFE) Films

Piezoelectric materials have gained significant attention in recent years due to its inherent polarization. Due to the flexible nature of the piezoelectric polymers, it can sustain higher strains compared to that of the inorganic piezoelectric materials, thus making them more suitable for mechanical energy harvester. In this chapter, the energy harvesting performance of the P(VDF-TrFE) is improved by structural modification. Specifically, a porous P(VDF-TrFE) film is created to improve the performance. Additionally, a self-charged supercapacitor is demonstrated.

*This section published substantially as K. Parida, V. Bhavanasi, V. Kumar, J. Wang, P. S. Lee, *J. Power Sources* **2017**, *342*, 70.

4.1 Introduction

Energy generation from ambient mechanical vibrations is significant for the realization of self-powered systems. With the advent of personal electronics, the demand for efficient energy conversion systems has increased significantly. Piezoelectric energy harvesters and piezoelectric materials have gained significant attention in the recent decade, due to its ability to harvest electrical energy from ambient mechanical vibrations. Extensive work has been done to enhance the energy harvesting ability of the P(VDF-TrFE) based piezoelectric polymer. One approach is to increase the internal stress in the material, by adding fillers in the piezoelectricity material. Alignment of the molecular chains further improves the performance.[1] The performance can be improved by combining the piezoelectric P(VDF-TrFE) with an electrostatic component (charged component).[2] The current of the piezoelectric energy harvester has been improved by utilizing the electrostatically doped graphene as the current collector in P(VDF-TrFE) based energy harvester.[3] To further improve the energy generation, it is hypothesized that by creating porous P(VDF-TrFE) films (with higher strain and lower dielectric constant) the energy harvesting performance of the P(VDF-TrFE) mechanical energy harvester can be improved. In this work, the structural modification was done to improve the performance. Porous P(VDF-TrFE) was created which lowered the dielectric constant and increased the β phase content and compressibility, thus improving the energy harvesting performance.

4.2 Results and Discussion

4.2.1 Morphological characterization of porous P(VDF-TrFE)

The vapor induced phase separation (VIPS) technique is adopted to fabricate the porous P(VDF-TrFE) film. This method is based on the phase separation in a ternary system of polymer/non-solvent/ solvent where P(VDF-TrFE) is the polymer, DMF is the solvent and water is the non-solvent.[4,5] The porous film is fabricated by exposing the drop casted polymer solution (P(VDF-TrFE) dissolved in DMF) to humidity. Upon exposing the drop

casted polymer solution to humidity, water vapor (non-solvent for P(VDF-TrFE)) penetrates into the polymer solution, due to the solubility of DMF and water. This results in a phase separation, creating a polymer rich and polymer diluted region. Subsequently, the P(VDF-TrFE) solidifies around the polymer diluted region (water droplet).[6] When the water is evaporated upon dying at room temperature, it leaves behind porous imprint in the P(VDF-TrFE) film. The presence of pores can be clearly seen from the FE-SEM image (Figure 4.1. a-d).

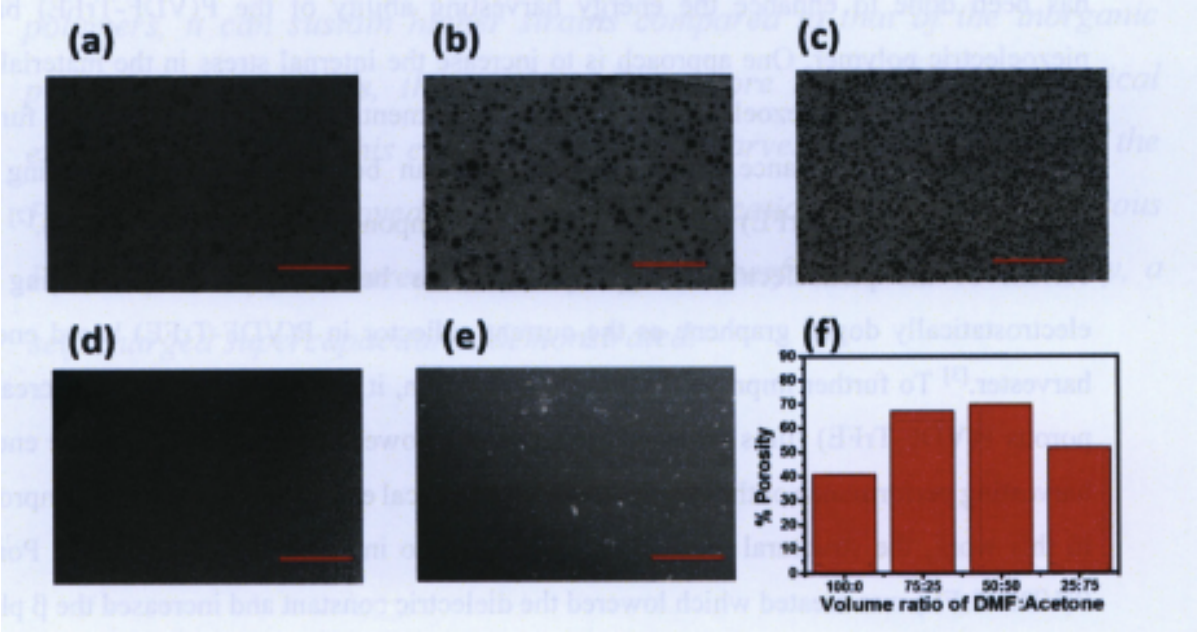

Figure 4.1. FESEM image of the porous P(VDF-TrFE) film prepared with variation of the volume percentage of DMF:acetone at (a) 100:0, (b) 75:25, (c) 50:50, and (d) 25:75. (e) FESEM image of the compact P(VDF-TrFE) film. Scale bar = 100 μm. (f) Variation of % porosity with the change in the volume percentage of DMF:Acetone.

The film fabricated by spin coating method shows compact structure without the presence of any porous structure (Figure 4.1e) The % porosity is optimized by varying the vapor pressure of the solvent. The vapor pressure is modified by mixing DMF (low vapor pressure of 3.5 hPa) with acetone (high vapor pressure of 240 hPa). As the amount of acetone increases, the % porosity increases, however at a high percentage of acetone (75% by volume), the amount of pores decreases (Figure 4.1 a-d and f). Higher vapor pressure leads

to the accelerated evaporation of the solvent, thus reducing the porosity. The maximum porosity is observed in the film prepared with (DMF: Acetone = 50:50) ratio.. To calculate the porosity, P(VDF-TrFE) films (thickness= 200 μm, area = 2 x 2 cm^2) were immersed in propylene carbonate solution for 30 minutes. The weight of the sample was measured before and after immersion. The porosity of the P(VDF-TrFE) films were calculated using the equation 4.1.[7]

$$\%P = \frac{M_S/\rho_S}{M_P/\rho_P + M_S/\rho_S} \quad (1)$$

where %P is the porosity of the P(VDF-TrFE) film; M_p is the mass of the P(VDF-TrFE) film; M_s is the mass of the absorbed propylene carbonate; ρ_p is the density of P(VDF-TrFE) and ρ_s is the density of the propylene carbonate.

4.2.2 Phase identification and quantification of P(VDF-TrFE) film

The β phase is the piezoelectric phase responsible for the piezoelectric behavior in P(VDF-TrFE). Thus it is essential to identify and quantify the presence of β phase. Figure 4.2a shows the FTIR spectra of the porous and compact P(VDF-TrFE) film. The piezoelectric β phase (TTTT) can be identified from the absorption band at 840 and 1275 cm^{-1} and the non-piezoelectric α phase (TGTG) can be identified from the absorption band at 614, 766 and 1152 cm^{-1}.[8,9] The relative percentage of α and β phase was calculated from the equation (4.1).

$$F(\beta) = \frac{A_\beta}{(K_\beta/K_\alpha)A_\alpha + A_\beta} \quad (4.1)$$

where F(β) is the relative percentage of β phase, K_{840} (7.7×10^4 cm^2 mol^{-1}) and K_{746}(6.1×10^4 cm^2 mol^{-1}) are the absorption coefficients for β and α phase respectively, A_α and A_β are the absorption intensity at 840 and 764 cm^{-1} respectively.[10] The relative proportion of β phase for the porous P(VDF-TrFE) film (fabricated with Acetone:DMF =50:50 by volume) is 94.8 % whereas for the compact thin film it is 86.4 % (Figure 4.2b). This shows a clear

increment in the proportion of β for the porous P(VDF-TrFE) film compared to the compact P(VDF-TrFE) film.

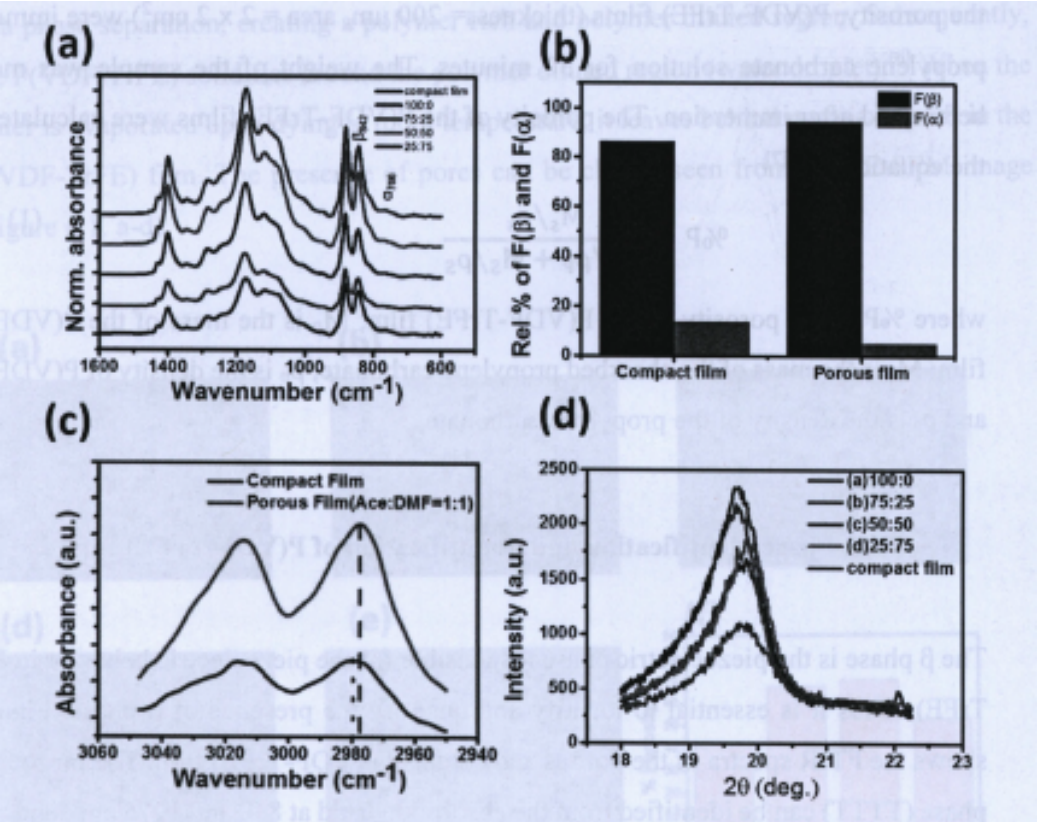

Figure 4.2. (a) FT-IR spectra of the P(VDF-TrFE) compact and porous film with variation of the volume percentage of DMF:acetone at (1) 100:0, (2) 75:25, (3) 50:50, and (4) 25:75. (b) The relative proportion of β phase for the compact and porous P(VDF-TrFE) film. (c) FT-IR spectra of the porous P(VDF-TrFE) film indicating the interfacial interactions. (d) XRD spectra of the P(VDF-TrFE) compact film and the porous foam with variation of the volume percentage of DMF:acetone at (1) 100:0, (2) 75:25, (3) 50:50, and (4) 25:75.

The increase in the β phase can be attributed to the H-bonding interactions between the polar water molecules with the P(VDF-TrFE) molecule.[11] These interfacial interactions lead to the nucleation of the β phase (all trans configuration).[12] The interfacial interactions was validated by the frequency shift of the CH_2 symmetric and asymmetric stretching vibration mode (Figure 4.2c) of the porous P(VDF-TrFE) film towards the lower wavenumber. The frequency shift occurs due to the change in the effective mass of CH_2

dipoles.[12] XRD analysis further verifies the claims made by spectroscopy analysis. The β phase is indicated by the peak at $2\theta = 19.8^0$ which is associated with the (110) or (200) planes of P(VDF-TrFE) film (Figure 4.2d). The full-width half maximum and peak intensity of the peak at 19.8^0 is higher for the porous P(VDF-TrFE) film compared to the compact P(VDF-TrFE) film, thus further validating the claim. It was observed that the amount of β phase changes with the % porosity (or with the change in the volume percentage of acetone and DMF). As the % porosity increases, the interfacial interaction increases, thus increasing the amount of β phases. Similarly, at a higher vapor pressure, % porosity decreases thus reducing the amount of β phases (Figure 4.2d).

4.2.3 Mechanism of energy generation

The piezoelectric energy harvester consists of a piezoelectric material, which on the application of a mechanical compressive pressure, creates an internal piezoelectric potential. The piezoelectric material consists of β phase (all trans (TTTT) conformation) consists of a positively charged hydrogen atoms and negatively charged fluorine atoms arranged on opposite side of the carbon chain. This non-overlapping of the positive and the negative charge centers give rise to a net dipole moment. However, these dipoles are randomly oriented giving rise to a net zero polarization. Upon poling, the dipoles are aligned in the direction of electric field. Application of a mechanical pressure changes the dipole moment which creates an internal piezoelectric potential across the film. The free charge carriers present in the metal contact (present at both sides on the P(VDF-TrFE) film) flows from the negative potential region to the positive potential across the external connection giving rise to a positive voltage peak. Upon releasing the mechanical pressure, the internal piezoelectric potential becomes zero. Thus the free charge carriers return back to the negative electrode, giving rise to a negative voltage peak. The schematic of the piezoelectric energy harvester is shown in Figure 4.3.

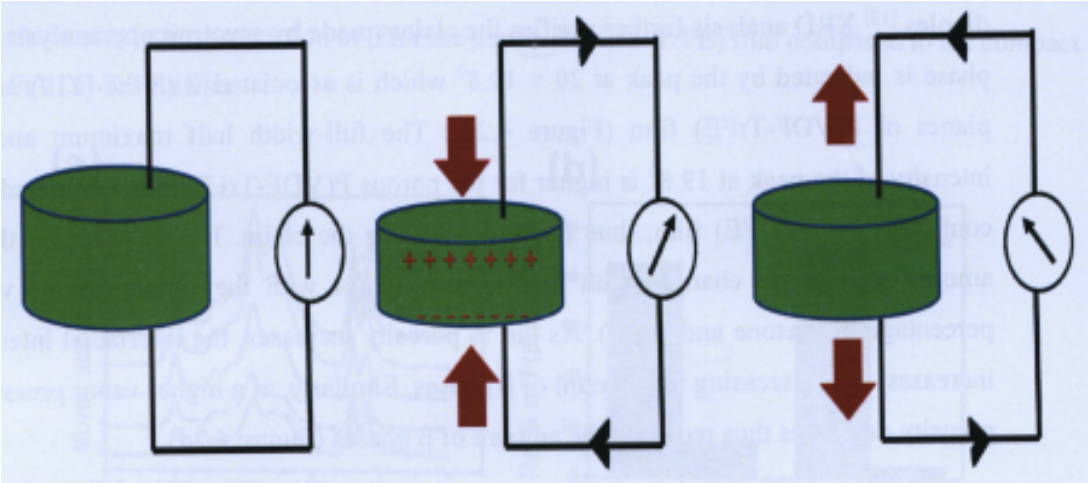

Figure 4.3. Schematic of the working of the piezoelectric energy harvester.

4.2.4 Energy harvesting performance

The energy harvesting performance of the porous P(VDF-TrFE) (fabricated with DMF:Acetone = 50:50, thickness = 200 μm, area = 2 cm^{-2}) was used to fabricate the piezoelectric energy harvester due to its higher β phase content and % porosity. Figure 4.4a schematically illustrates the piezoelectric energy harvesting device, and Figure 4.4b shows a digital photo of the device. The energy harvesting performance of the porous P(VDF-TrFE) film (open-circuit voltage (V_{oc}) and short-circuit current density (I_{sc})) was measured by exerting a compressive mechanical pressure of 600 kPa at a frequency of 5 Hz. The porous P(VDF-TrFE) generated an approximate V_{oc} of 6 V (Figure 4.4c) and I_{sc} of 0.6 $\mu A \cdot cm^{-2}$ (Figure 4.4d). Under real application, the device will be subjected to forces of various magnitude. Thus the energy harvesting performance was evaluated by varying the magnitude of the compressive pressure. As the mechanical pressure was increased, the strain in the material increased, which resulted in the increment of the voltage output (Figure 4.4e). With the increment the applied frequency at mechanical pressure of 600 kPa the voltage output increases (Figure 4.4h).

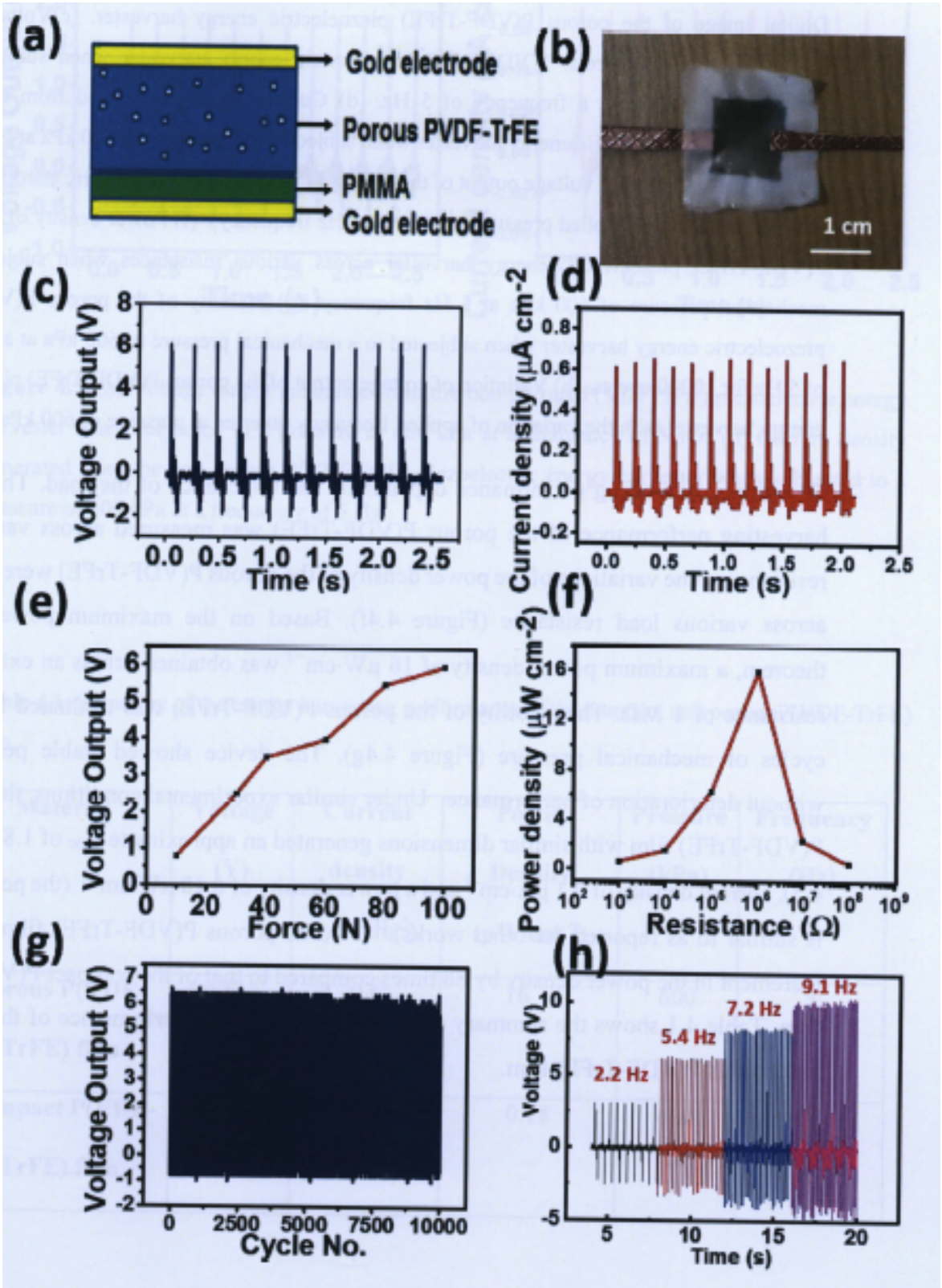

Figure 4.4. (a) Schematic diagram of the porous P(VDF-TrFE) piezoelectric energy harvester. (b) Digital image of the porous P(VDF-TrFE) piezoelectric energy harvester. (c)Voltage output generated from the porous P(VDFTrFE) piezoelectric energy harvester when subjected to a pressure of 600 kPa at a frequency of 5 Hz. (d) Current density generated from the porous P(VDFTrFE) piezoelectric energy harvester when subjected to a pressure of 600 kPa at a frequency of 5 Hz. (e) Variation of voltage output of the porous P(VDF-TrFE) piezoelectric energy harvester with the variation of applied pressure (exerted at 5 Hz frequency). (f) Power density of the porous P(VDF-TrFE) piezoelectric energy harvester across various resistances when subjected to a mechanical pressure of 600 kPa at 5 Hz frequency. (g) Stability of the porous P(VDF-TrFE) piezoelectric energy harvester when subjected to a mechanical pressure of 600 kPa at a frequency of 5 Hz for 10000 cycles. (h) Variation of voltage output of the porous P(VDF-TrFE) piezoelectric energy harvester with the variation of applied frequency (exerted at pressure of 600 kPa).

The energy harvesting performance depends on the impedance of the load. Thus energy harvesting performance of the porous P(VDF-TrFE) was measured across various load resistances. The variations of the power density of the porous P(VDF-TrFE) were measured across various load resistance (Figure 4.4f). Based on the maximum power transfer theorem, a maximum power density of 16 $\mu W \cdot cm^{-2}$ was obtained across an external load resistance of 1 MΩ. The stability of the porous P(VDF-TrFE) was evaluated for 10,000 cycles of mechanical pressure (Figure 4.4g). The device showed stable performance without deterioration of performance. Under similar experimental conditions, the compact P(VDF-TrFE) film with similar dimensions generated an approximate V_{oc} of 1.8 V (Figure 4.5), current density of 0.1 $\mu A \cdot cm^{-2}$ and a power density of 0.18 $\mu W \cdot cm^{-2}$ (the performance is similar to as reported for other works).[13–15] The porous P(VDF-TrFE) film shows an increment in the power density by 88 times compared to that of the compact P(VDF-TrFE) film. Table 4.1 shows the summary of the energy harvesting performance of the compact and porous P(VDF-TrFE) film.

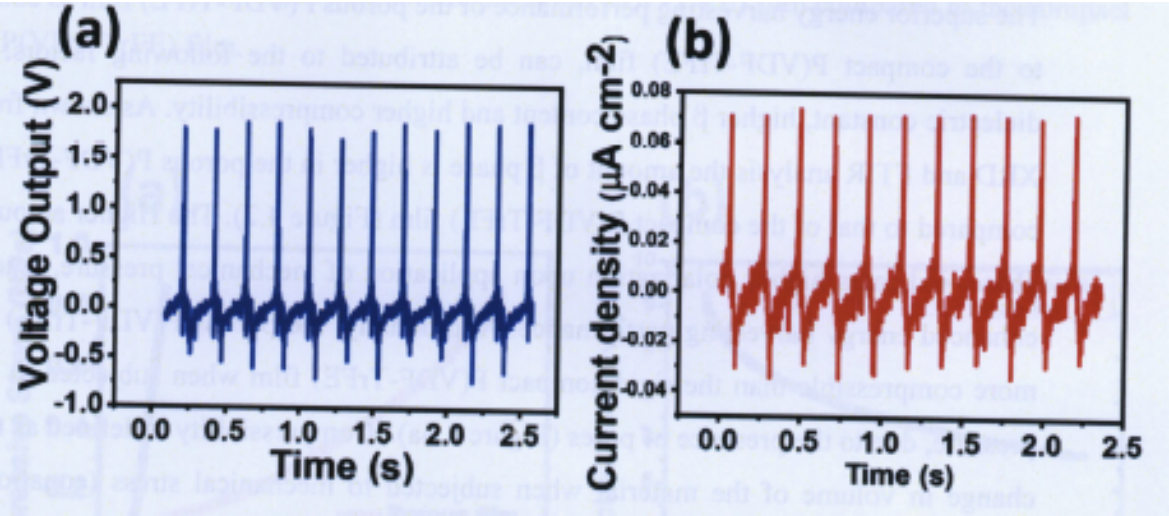

Figure 4.5. (a) Voltage output generated from the non-porous P(VDFTrFE) piezoelectric energy harvester when subjected to a pressure of 600 kPa at a frequency of 5 Hz. (d) Current density generated from the non-porous P(VDFTrFE) piezoelectric energy harvester when subjected to a pressure of 600 kPa at a frequency of 5 Hz.

Table 4.1: Summary of the energy harvesting performance of the compact and porous P(VDF-TrFE) film.

Material	Voltage (V)	Current density ($\mu A \cdot cm^{-2}$)	Power Density ($\mu W \cdot cm^{-2}$)	Pressure (kPa)	Frequency (Hz)
Porous P(VDF-TrFE) film	6	0.6	16	600	5
Compact P(VDF-TrFE) film	1.8	0.08	0.18	600	5

The superior energy harvesting performance of the porous P(VDF-TrFE) film as compared to the compact P(VDF-TrFE) film, can be attributed to the following factors: lower dielectric constant, higher β phase content and higher compressibility. As shown from the XRD and FTIR analysis the amount of β phase is higher in the porous P(VDF-TrFE) film compared to that of the compact P(VDF-TrFE) film (Figure 4.2). The Higher amount of β phase, indicates higher polarization upon application of mechanical pressure, leading to enhanced energy harvesting performance. Additionally, the porous P(VDF-TrFE) film is more compressible than the rigid compact P(VDF-TrFE) film when subjected to similar pressure, due to the presence of pores (Figure 4.6a). Compressibility is defined as the unit change in volume of the material when subjected to mechanical stress (equation 4.2). According to the equation 4.3, the compressibility of the piezoelectric material is directly related to the piezoelectric coefficient of the material. The porous P(VDF-TrFE) film 3.6 times more compressibility than the compact P(VDF-TrFE) film at a compressive pressure of 0.6 MPa.

$$C = \frac{\Delta U/U}{\sigma} \tag{4.2}$$

$$d = \frac{\partial P}{\partial \sigma} = \frac{\partial(\mu/U)}{\partial \sigma} = P\left(\frac{\partial \ln \mu}{\partial \sigma} - \frac{\partial \ln U}{\partial \sigma}\right) = P\left(\frac{\partial \ln \mu}{\partial \sigma} + C\right) \tag{4.3}$$

where C is the compressibility of the material; U is the volume of the sample; ΔU is the change in the volume of the sample on application of mechanical stress; σ is the stress applied; d is the piezoelectric coefficient; P is the polarization and μ is the total dipole moment. Moreover, the porous P(VDF-TrFE) film have low dielectric permittivity compared to the compact P(VDF-TrFE) film. Figure 4.6b shows the variation of dielectric permittivity over the frequencies ranging from 1 kHz to 1000 kHz. The porous P(VDF-TrFE) film shows 3 times lower dielectric permittivity as compared to the compact film. Dielectric permittivity is the opposition offered to the flow of the electric field. Thus a low dielectric permittivity will have a higher internal piezoelectric potential. The piezoelectric voltage output is inversely related to the dielectric permittivity, which results in the

increment in the voltage output of the porous P(VDF-TrFE) film compared to the compact P(VDF-TrFE) film.

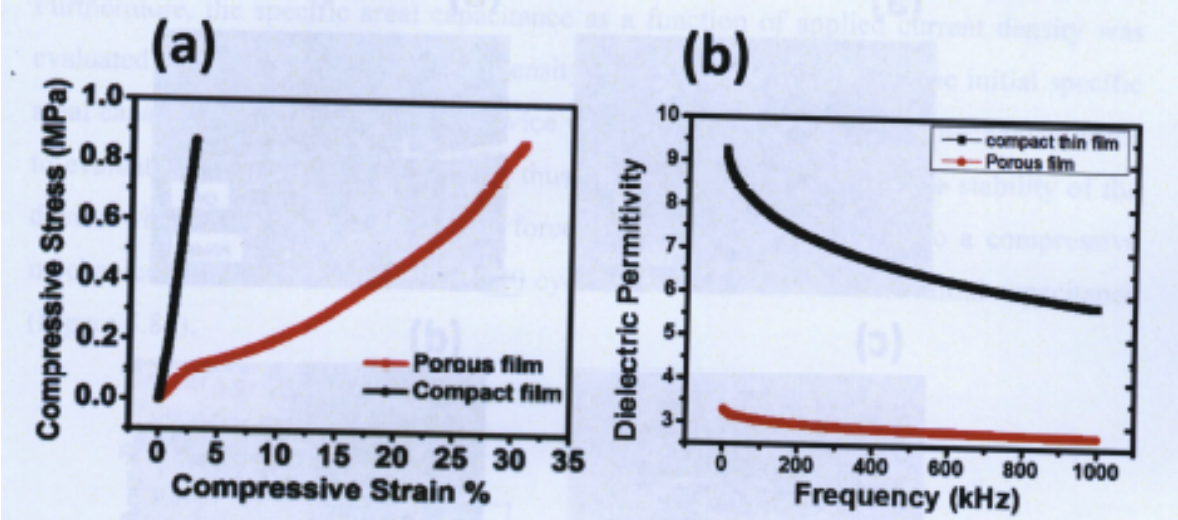

Figure 4.6. (a) Compressive stress-strain behaviour of the porous and compact P(VDF-TrFE) film. (b) Variation of dielectric permittivity with the change in applied frequency for the porous and compact P(VDF-TrFE) film.

4.2.5 Application - Self-charged supercapacitor

A self-charged supercapacitor was demonstrated, which stores charge on the application of mechanical force. The porous P(VDF-TrFE) was used as the separator in the supercapacitor. It acts as a matrix to hold the electrolyte and creates an internal electric field for the migration of ions, on the application of mechanical force. P(VDF-TrFE) is widely known to act as a matrix for electrolytes, and its piezoelectric properties make it an ideal candidate to be used as the separator in the self-charged electric double layer capacitor (SP-EDLC).[16]

4.2.5.1 Structural Characterization of the CNT electrode

CNT embedded in PDMS was used as the electrodes in the self-charged supercapacitor. The top and cross-section FESEM image of the CNT embedded in PDMS can be seen from the Figure 4.7a and b and the digital photo can be seen from the Figure 4.7c and d. Due to the excellent mechanical robustness,[17] and superior charge storage properties[18,19] CNT

was used as the electrode and current collector in the SP-EDLC. The active area of the CNT electrode exposed to the electrode was 1 x 1 cm^2.

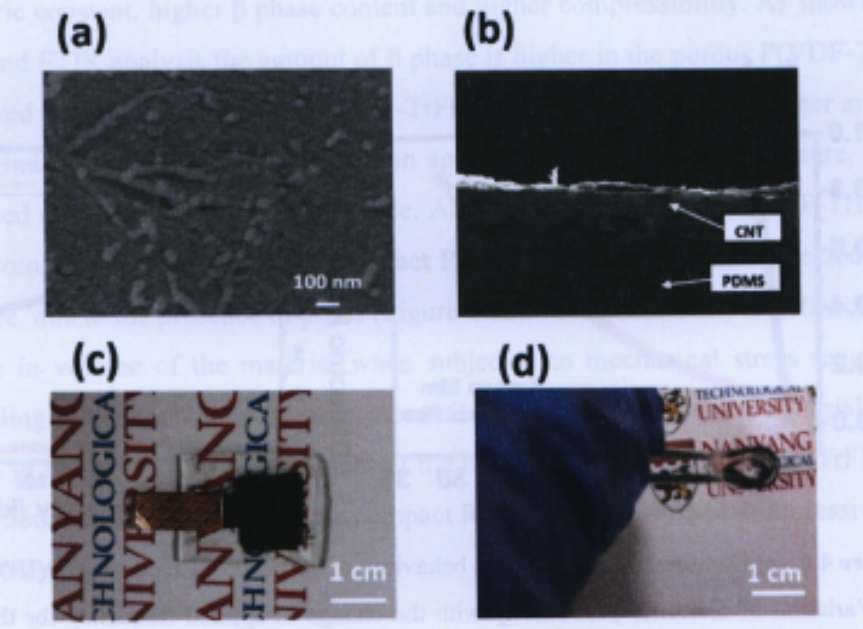

Figure 4.7. (a) FE-SEM image of the CNT electrode. (b) Cross-section of the electrode showing the embedded portion of CNT in PDMS. (c) Digital image of the CNT embedded in PDMS electrode. (d) Digital image showing the high flexibility of the electrode.

4.2.5.2 Electrochemical performance of the SP-EDLC

To evaluate the electrochemical performance of the SP-EDLC, the device was as-assembled in a sandwich structure where CNT embedded in PDMS was used as the electrodes and P(VDF-TrFE) as the separator. CNT is used as the supercapacitor electrode, due to its electric double layer charge storage mechanism, thus facilitating faster charge storage. P(VDF-TrFE) film was soaked with polymer gel electrolyte. Figure 4.8a shows a typical double layer cyclic voltammetry (CV) behavior without any distinctive reduction and oxidation peak, clearly indicating the formation of an electric double layer at the respective electrodes. The double layer formation was further verified from the galvanostatic discharge behavior of the device (Figure 4.8b). The specific areal capacitance was calculated from the discharge profile taking discharge time into consideration. The specific areal capacitance of the SP-EDLC was measured to be 1.2 $mFcm^{-2}$ at a discharge

current density of 0.05 $mAcm^{-2}$ (calculated from the galvanostatic discharge behavior). The obtained specific areal capacitance is similar to other reported value.[20] The areal energy density was calculated to be 1.7 $\mu Whcm^{-2}$ and power density to be 24.4 μWcm^{-2}. Furthermore, the specific areal capacitance as a function of applied current density was evaluated (Figure 4.8c). At a current density of 0.25 mA/cm^2, 66 % of the initial specific areal capacitance was retained. The device will be further subjected to a mechanical force to evaluate the self-charging behavior; thus, it is essential to evaluate the stability of the device when subjected to mechanical force. On subjecting the device to a compressive mechanical pressure of 600 kPa for 700 cycles, it retains ~80 % of its initial capacitance (Figure 4.8d).

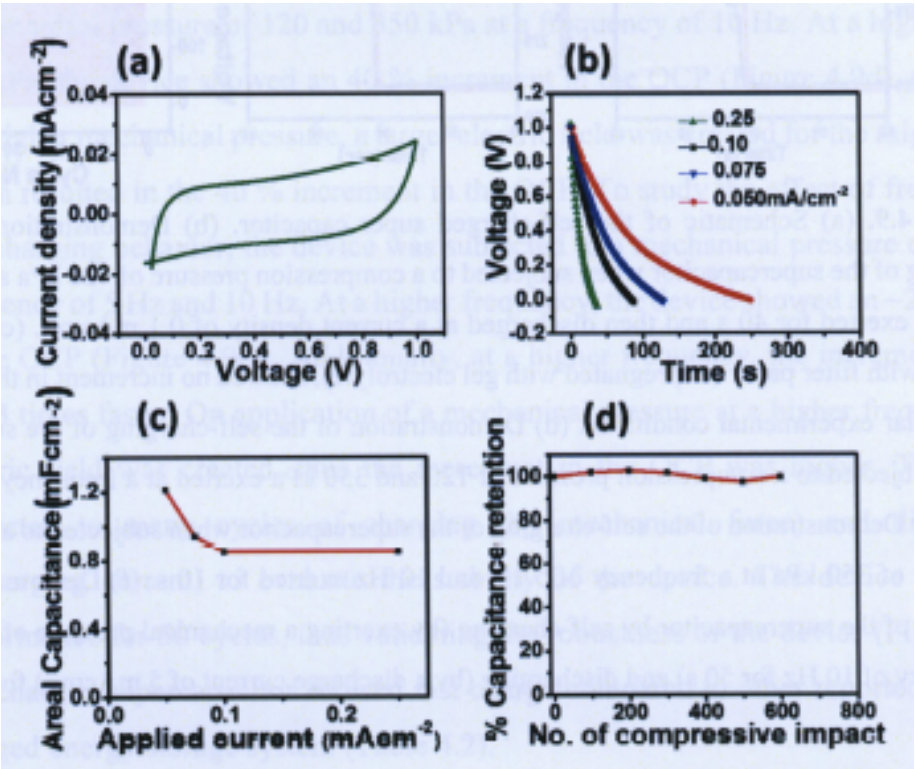

Figure 4.8. Electrochemical performance of the self-charged supercapacitor. (a) Cyclic voltammogram (CV) of the self-charged supercapacitor at a scan rate of 20 mVs^{-1}. (b) Galvanostatic charging and discharging curves of the self-charged supercapacitor measured at current densities of 0.050, 0.075, 0.10, and 0.25 $mAcm^{-2}$. (c) The areal capacitance of the self-charged supercapacitor method at various current densities. (d) Areal capacitance retention of the self-charged supercapacitor when subjected to a mechanical pressure of 600 kPa at a frequency of 5 Hz.

4.2.5.3 Self-Charging behavior of SP-EDLC

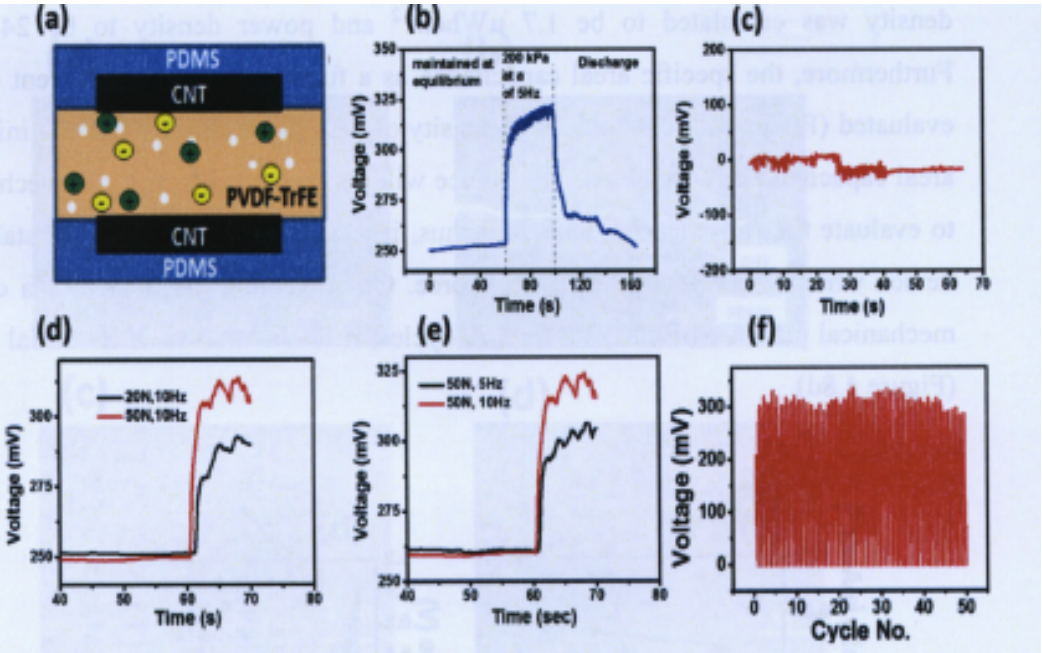

Figure 4.9. (a) Schematic of the self-charged super capacitor. (b) Demonstration of the self charging of the supercapacitor when subjected to a compression pressure of 420 kPa at a frequenc of 5 Hz exerted for 40 s and then discharged at a current density of 0.1 $mAcm^{-2}$. (c) The contrc sample with filter paper (impregnated with gel electrolyte), showed no increment in the OCP unde the similar experimental conditions. (d) Demonstration of the self-charging of the supercapacitc when subjected to a compression pressure of 120 and 350 kPa exerted at a frequency of 10 Hz fc 10 s. (e) Demonstration of the self-charging of the supercapacitor when subjected to a compressio pressure of 350 kPa at a frequency of 5 Hz and 10 Hz exerted for 10 s. (f) Demonstration of th stability of the supercapacitor by self-charging (by exerting a mechanical pressure of 600 kPa at frequency of 10 Hz for 50 s) and discharging (by a discharge current of 5 $mAcm^{-2}$) for 50 cycles.

To demonstrate the self-charging behavior, the porous P(VDF-TrFE) film was used as th separator in the supercapacitor. The porous P(VDF-TrFE) film can produce high voltag output (under compressive mechanical force) as described earlier. The P(VDF-TrFE) filr was impregnated with PMMA/$LiClO_4$/PC based gel electrolyte and sandwiched betwee CNT electrodes (Figure 4.9a). Before application of mechanical force, the device wa maintained at equilibrium, showing an initial open circuit potential (OCP) of 250 m

(Figure 4.9b). Upon application of an compression mechanical pressure of 420 kPa at a frequency of 5 Hz for 40 s, the SP-EDLC showed an increment in the OCP by 70 mV (Figure 4.9b). 90 % of the increment in the potential was achieved in less than 10 sec. A discharge current density of 0.1 μAcm^{-2} was applied to discharge the stored charge. From the discharge behavior, the amount of the charge stored (on the application of mechanical force) was calculated to be 95 μFcm^{-2}. To confirm the self-charging behavior, the P(VDF-TrFE) was replaced by a filter paper (impregnated with gel electrolyte). Under the similar experimental conditions, the device with filter paper showed no increment in the OCP (Figure 4.9c), thus validating the self-charging behavior using the porous P(VDF-TrFE) film. To better understand the self-charging behavior, the SP-EDLC was subjected to mechanical pressure with different magnitude and frequency. The device was subjected to a mechanical pressure of 120 and 350 kPa at a frequency of 10 Hz. At a higher pressure of 350 kPa, the device showed an 40 % increment in the OCP (Figure 4.9d). On application of a higher mechanical pressure, a larger electric field was created for the migration of ions, which resulted in the 40 % increment in the OCP. To study the effect of frequency on the self-charging behavior, the device was subjected to a mechanical pressure of 350 kPa at a frequency of 5 Hz and 10 Hz. At a higher frequency, the device showed an ~20 % increment in the OCP (Figure 4.9e). Additionally, at a higher frequency, the increment in the OCP was 3 times faster. On application of a mechanical pressure at a higher frequency, a larger electric field was created, thus the increment in the OCP was higher. The device was subjected to many cycles of charging (by mechanical force) and discharging (by discharging current) to evaluate the stability of the device. The device showed stable performance for 50 cycles, thus validating the robustness of the device (Figure 4.9f). The self-charged supercapacitor showed fast charge compared to other reported work on self-charged energy storage system (Table 4.2).

Table 4.2. Table highlighting the state-of-the-art self-charged electrochemical energy storage devices.

Sl No.	Self-charged energy storage	Force (N)	Frequency (Hz)	Increase in the OCP (mV)	Time of charging (s)	Cycle Stability	Reference
1	Hybridizing Energy Conversion and Storage	45	2.3	68	240	-	[21]
2	CuO/PVDF nanocomposite for Self-Charging Battery	30	1	169	240	5	[22]
3	PVDF–PZT nanocomposite for Self-Charging Battery	10	1.5	42.3	210	4	[23]
4	PVDF nanostructure for Self-Charging Battery	34	1.8	138	250	50	[24]
5	Piezoelectric-Driven Self-Charging Supercapacitor	18.8	-	~37	~125	15	[25]
6	Fast charging self-charged electrical double layer capacitor	70	5	60	10	50	This work

4.2.5.3 Mechanism of the self-charged EDLC

The mechanism of the SP-EDLC device is schematically illustrated in Figure 4.10. The device consists of a porous P(VDF-TrFE) film (as the piezoelectric-separator) impregnated with PMMA/$LiClO_4$/PC based gel electrolyte, sandwich between two CNT electrodes. Before application of mechanical pressure, the ions are uniformly distributed in the matrix of the porous P(VDF-TrFE) film, thus having a constant concentration of the ions across the matrix (Figure 4.10a). At equilibrium condition, the Fermi level of the electrodes matches with the electrochemical potential of the ions in the electrolyte. On application of mechanical pressure, the porous P(VDF-TrFE) film creates an internal electric field of 57.5 V/mm. This leads to the migration of ions (based on their characteristic charge) (Figure 4.10b). Due to the migration of ions, the local concentration of ions at the CNT electrode/electrolyte interface changes. This change of concentration changes the electrochemical potential at the interface. Adsorption of ions occurs at the CNT electrode surfaces to maintain equilibrium with the changes electrochemical potential, thus forming an electrical double layer (Figure 4.10c). The SP-EDLC stores charge, due to the formation of the electric double layer, which is reflected in the increase in the OCP of the device. Due to the fast adsorption of ions at CNT electrode, the device demonstrates faster self-charging compared to self-charging based on slow intercalation mechanism.

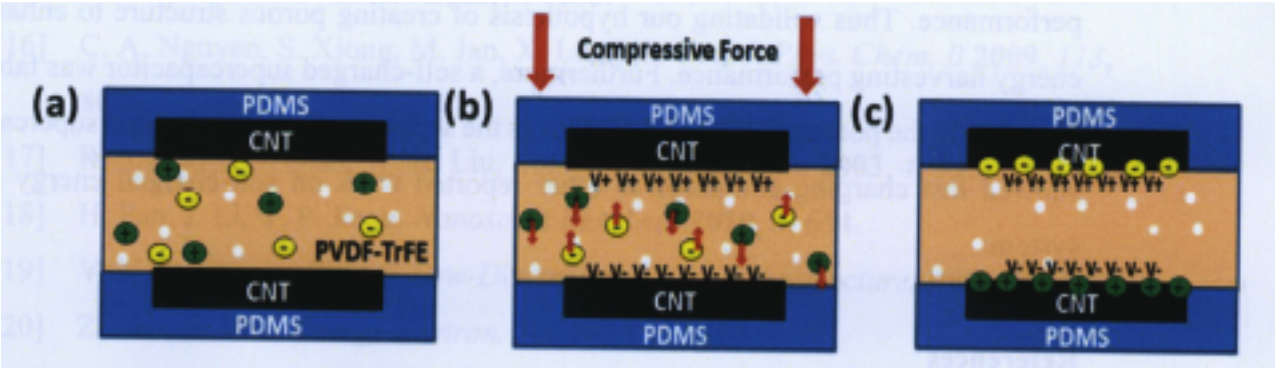

Figure 4.10. Schematic representation of the mechanism of SP-EDLC device. (a) The device is maintained at equilibrium condition where the ions are uniformly distributed in the P(VDF-TrFE) film. (b) On application of the mechanical pressure an electric field is developed which leads to the migration of ions. (c) Development of an EDL layer at the electrodes.

4.3 Principal Outcomes

- Fabricated a porous P(VDF-TrFE) film using VIPS method.
- Demonstrated enhancement of energy harvesting performance by a porous P(VDF-TrFE) film due to lower dielectric constant, higher β phase content and higher compressibility compared to that of the compact P(VDF-TrFE) film.
- Demonstrated a fast charging self-charged supercapacitor by utilizing the porous P(VDF-TrFE) as the separator.
- It is extremely challenging to electrically pole the porous P(VDF-TrFE) films, due to the easy dielectric breakdown. This problem is addressed by fabricated a self-poled P(VDF-TrFE) film, described in chapter 5.

4.4 Chapter Summary

In this chapter, a porous P(VDF-TrFE) film was prepared and showed superior energy harvesting performance compared to that of the compact P(VDF-TrFE) film, thus proving our hypothesis. The porous P(VDF-TrFE) film showed an increment in the power density by 88 times compared to that of the compact P(VDF-TrFE) film. The porous structure lower the dielectric constant, increases the higher β phase content and increases the compressibility of the P(VDF-TrFE) film, which improving the energy harvesting performance. Thus validating our hypothesis of creating porous structure to enhance the energy harvesting performance. Furthermore, a self-charged supercapacitor was fabricated by utilizing the porous P(VDF-TrFE) film as the separator. The self-charged supercapacitor showed fast charging compared to other reported work on self-charged energy storage system.

References

[1] Y.-Y. Choi, P. Sharma, C. Phatak, D. J. Gosztola, Y. Liu, J. Lee, B. Lee, J. Li, A. Gruverman, S. Ducharme, S. Hong, *ACS Nano* **2015**, *9*, 1809.

[2] V. Bhavanasi, V. Kumar, K. Parida, J. Wang, P. S. Lee, *ACS Appl. Mater.*

Interfaces **2016**, *8*, 521.

[3] S.-H. Bae, O. Kahya, B. K. Sharma, J. Kwon, H. J. Cho, B. Özyilmaz, J.-H. Ahn, *ACS Nano* **2013**, *7*, 3130.

[4] H. Matsuyama, *J. Appl. Polym. Sci.* **1999**, *74*, 171.

[5] A. Venault, Y. Chang, D. M. Wang, D. Bouyer, *Polym. Rev.* **2013**, *53*, 568.

[6] M. Li, I. Katsouras, C. Piliego, G. Glasser, I. Lieberwirth, P. W. M. Blom, D. M. de Leeuw, *J. Mater. Chem. C* **2013**, *1*, 7695.

[7] M. Gu, J. Zhang, X. Wang, H. Tao, L. Ge, *Desalination* **2006**, *192*, 160.

[8] Z. Pi, J. Zhang, C. Wen, Z. B. Zhang, D. Wu, *Nano Energy* **2014**, *7*, 33.

[9] J. H. Lee, H. J. Yoon, T. Y. Kim, M. K. Gupta, J. H. Lee, W. Seung, H. Ryu, S.-W. Kim, *Adv. Funct. Mater.* **2015**, 3203.

[10] S. Garain, T. K. Sinha, P. Adhikary, K. Henkel, S. Sen, S. Ram, C. Sinha, D. Schmeißer, D. Mandal, *ACS Appl. Mater. Interfaces* **2015**, *7*, 1298.

[11] S. Chen, X. Li, K. Yao, F. E. H. Tay, A. Kumar, K. Zeng, *Polymer (Guildf).* **2012**, *53*, 1404.

[12] D. Mandal, K. Henkel, D. Schmeißer, *Phys. Chem. Chem. Phys.* **2014**, *16*, 10403.

[13] V. Bhavanasi, D. Y. Kusuma, P. S. Lee, *Adv. Energy Mater.* **2014**, *4*.

[14] J. H. Lee, K. Y. Lee, M. K. Gupta, T. Y. Kim, D. Y. Lee, J. Oh, C. Ryu, W. J. Yoo, C. Y. Kang, S. J. Yoon, J. B. Yoo, S. W. Kim, *Adv. Mater.* **2014**, *26*, 765.

[15] L. Persano, C. Dagdeviren, Y. Su, Y. Zhang, S. Girardo, D. Pisignano, Y. Huang, J. A. Rogers, *Nat. Commun.* **2013**, *4*, 1633.

[16] C. A. Nguyen, S. Xiong, M. Jan, X. Lu, P. S. Lee, *J. Phys. Chem. B* **2009**, *113*, 8006.

[17] R. S. Ruoff, D. Qian, W. K. Liu, *Comptes Rendus Phys.* **2003**, *4*, 993.

[18] H. Pan, J. Li, Y. P. Feng, *Nanoscale Res. Lett.* **2010**, *5*, 654.

[19] V. V. N. Obreja, *Phys. E Low-Dimensional Syst. Nanostructures* **2008**, *40*, 2596.

[20] Z. Cao, B. Wei, *Energy Environ. Sci.* **2013**, *6*, 3183.

[21] X. Xue, S. Wang, W. Guo, Y. Zhang, Z. L. Wang, *Nano Lett.* **2012**, *12*, 5048.

[22] X. Xue, P. Deng, S. Yuan, Y. Nie, B. He, L. Xing, Y. Zhang, *Energy Environ. Sci.* **2013**, *6*, 2615.

[23] Y. Zhang, Y. Zhang, X. Xue, C. Cui, B. He, Y. Nie, P. Deng, Z. L. Wang,

Nanotechnology **2014**, *25*, 105401.

[24] Y. S. Kim, Y. Xie, X. Wen, S. Wang, S. J. Kim, H. K. Song, Z. L. Wang, *Nano Energy* **2015**, *14*, 77.

[25] B. L. S. W. K. Y.-S. K. S. . W. Z. L. Ramadoss A. Saravanakumar, *ACS Nano* **2015**, *9*, 4337.

Chapter 5

Self-polarized porous P(VDF-TrFE) film

This chapter addresses the persistent issue of poling porous piezoelectric polymers, by preparing a self-poled porous P(VDF-TrFE) film utilizing a modified breath figure technique, which creates and aligns the piezoelectric β phase without the costly and tedious annealing and poling processes. The energy harvesting performance of the P(VDF-TrFE) is improved by utilizing the combined effect of piezoelectric polarization and triboelectric surface charge of the self-polarized P(VDF-TrFE) film. Furthermore, a self-powered wide range pressure sensor is demonstrated. Moreover, the practical applicability of the device is demonstrated by utilizing the pressure sensor in the human-machine interface, autonomous humanoid robots, and smart quadcopters.

*This section published substantially as K. Parida, V. Bhavanasi, V. Kumar, R. Bendi, P. S. Lee, *Nano Res.* **2017**, DOI 10.1007/s12274-017-1567-6.

5.1 Introduction

Self-powered, interactive, maintenance free and multifunctional operations are the key requirement for the realization of next-generation electronics for potential application in health monitoring, sensor networks, smart robotics and sports application.[1–3] One of the key requirement for the realization of a self-powered system is the realization of an efficient energy harvesting system which can harness energy from the ambient environment. Recently, triboelectric energy harvester (TEH) reported by Wang et al. has been a promising candidate for mechanical energy harvesting due to its ability to generate higher voltage output and power density compared to that of the piezoelectric energy harvester. Additionally, it can operate at very low and irregular mechanical pressure.[4–6] Due to the superior energy harvesting ability, triboelectric energy harvester is fabricated in this work. As described in the section 2.1.3, the energy generation of the triboelectric nanogenerators depends on the surface charge of the polymers. In general, the surface charge density of polymers used in a triboelectric generator are of the order of 10^{-4} C/m. However, in comparison to a typical polymers, the piezoelectric polymers such as P(VDF-TrFE) have a higher surface charge density (in the range of 10^{-1} Cm^{-2}), which is three orders of magnitude higher than that of a typical dielectric polymer. It is hypothesized that the energy harvesting performance of the P(VDF-TrFE) can be increased by utilizing the combined effect of triboelectric surface charge and polarization induced surface charge. To validate the hypothesis, a self-poled porous P(VDF-TrFE) film is used as the triboelectric energy harvester.

5.2 Results and discussion

5.2.1 Morphological and ferroelectric characterization of the porous self-poled P(VDF-TrFE) film

Figure 5.1a shows the digital photo of the highly flexible, rollable and free-standing porous P(VDF-TrFE) film, fabricated by the modified breath-figure technique. The film is milky white in color due to the internal scattering of light, caused by the pores present in the film.[7] The surface morphology of the film (Figure 5.1b) shows the porous structure (pore size ~10

μm). The pores are not only present on the surface but are distributed throughout the matrix of the film, which can be seen in the cross-section FESEM image (Figure 5.1c). The inner pores present in the matrix of the film, are much bigger in size compared with that of the pores present on the surface. The presence of pores makes the film spongy and compressible.

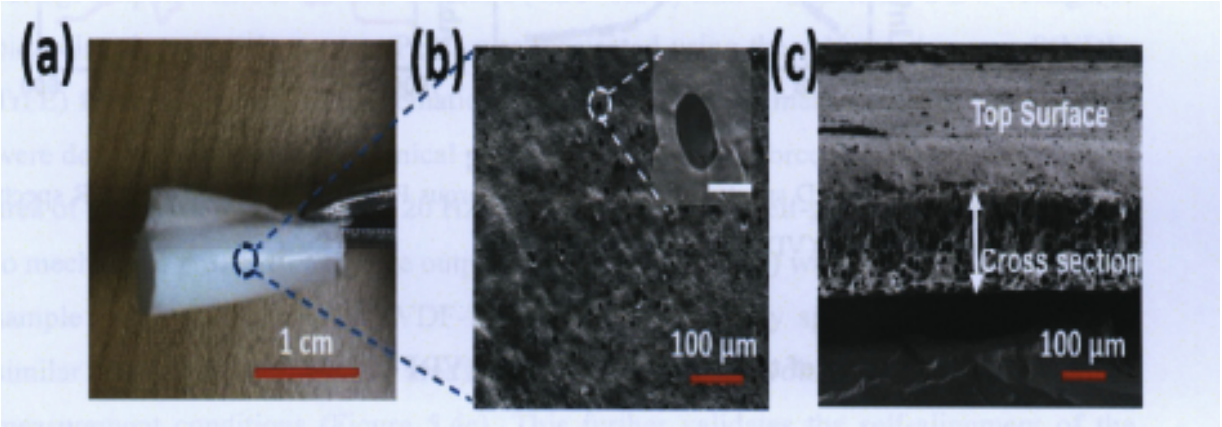

Figure 5.1. (a) Digital photo of the self-poled porous P(VDF-TrFE) film. (b) FESEM image showing the top view of self-poled porous P(VDF-TrFE) film. Inset in (b) is an enlarged FESEM image showing a pore. Scale bar: 10 μm. (c) Cross-sectional FESEM images of the self-poled porous P(VDF-TrFE) film.

The piezoelectric behavior of the P(VDF-TrFE) film is due to the presence of the β phase, which was confirmed by the XRD, and the FTIR analysis. Figure 5.2a shows the XRD pattern of the porous P(VDF-TrFE) film. The predominant peak at $2\theta = 19.7^0$ corresponds to the (110)/(200) planes of the piezoelectric β phase.[8,9] A minor amount of α phase can be found with the shoulder peak at $2\theta = 18^0$. The FTIR spectroscopy analysis of the P(VDF-TrFE) film further validates the presence of β phase. Figure 5.2b illustrates the infrared absorption spectra of the P(VDF-TrFE) porous film. The absorption band at 842 and 1276 cm^{-1} are the characteristic traits of the piezoelectric β phase.[10,11]

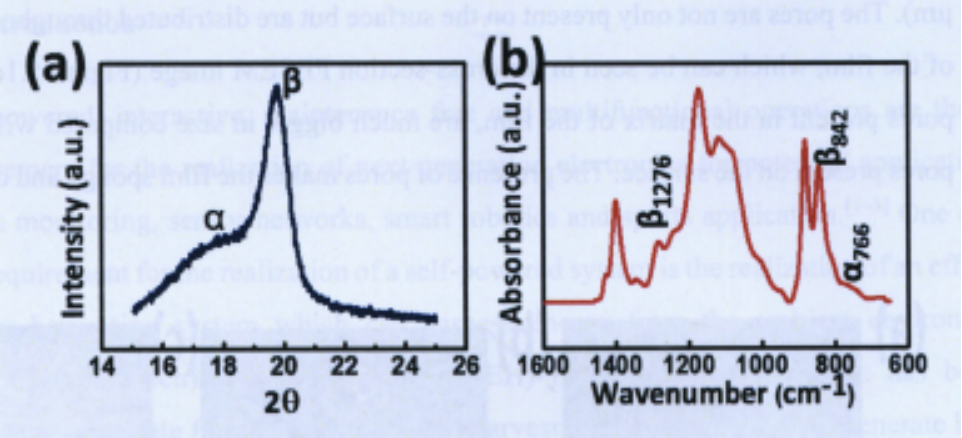

Figure 5.2. (a) XRD spectra of the self-poled porous P(VDF-TrFE) film. (b) FTIR spectra of the self-poled porous P(VDF-TrFE) film.

5.2.2 Evaluation of the self-poled porous P(VDF-TrFE) film

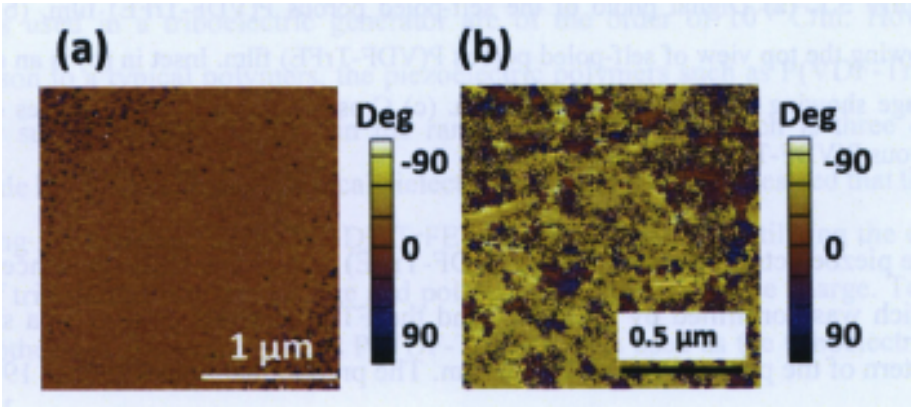

Figure 5.3. PFM phase image of the (a) Self-poled porous P(VDF-TrFE) film. (b) Non-poled compact P(VDF-TrFE) film.

The self-polarization phenomenon of the P(VDF-TrFE) film was analyzed using Piezoresponse force microscopy (PFM). The observed uniform contrast in the phase behavior of the porous P(VDF-TrFE) film (Figure 5.3a), reveals the unipolar orientation of dipoles. For comparison, PFM analysis of the control sample (non-poled compact P(VDF-TrFE) film prepared by spin coating method with similar dimensions) was carried out as

shown in Figure 5.3b. The domains with different orientations in Figure 5.3b indicates randomly oriented dipoles of the non-poled compact P(VDF-TrFE) film.[12]

Another method to evaluate the self-alignment of the P(VDF-TrFE) films is to measure the energy harvesting performance. The aligned P(VDF-TrFE) film will generate a higher voltage output, whereas the non-aligned P(VDF-TrFE) film will generate a low voltage. A piezoelectric energy harvester (PEH) was fabricated using the self-poled porous P(VDF-TrFE) film as shown in the schematic (Figure 5.4a). All the measurement in this section were done by applying a mechanical pressure of 625 kPa (a force of 62.5 N exerted on an area of 1 cm^{-2}) at a frequency of 20 Hz. Upon subjecting the self-poled P(VDF-TrFE) PEH to mechanical pressure, a voltage output of 21 V (Figure 5.4b) was generated. The control sample (non-poled compact P(VDF-TrFE) film, prepared by spin coating method with similar thickness and working area), generates an output voltage of 0.6 V, at similar measurement conditions (Figure 5.4c). This further validates the self-alignment of the porous P(VDF-TrFE) film fabricated by the modified breath figure technique.

Usually, the breath figure technique (also known as the vapor induce phase separation technique) is used to create porous polymers by exposing a drop casted or spin coated polymer solution to humidity at room temperature (25 °C).[7,13,14] In the presence of humidity water vapor condenses onto the solution. This acts as a mold for the pores and the polymer nucleates around the water droplets. In our modified breath figure technique, the drop casted polymer solution was exposed to humidity (50% relative humidity (RH)) at a temperature at -20 °C. The self-polarization effect was observed, only when the breath figure technique was performed at a temperature below 0 °C (as indicated by the piezoelectric energy harvesting performance measured with the variation of fabrication temperature, Figure 5.4d). Moreover, it was observed that the film fabricated at a temperature of -20 °C in the absence of humidity (< 5 % RH), fails to align the P(VDF-TrFE) dipoles (as indicated by the piezoelectric energy harvesting performance, Figure 5.4e). Therefore, self-polarization was obtained when both low temperature (below 0 °C) and humidity were present.

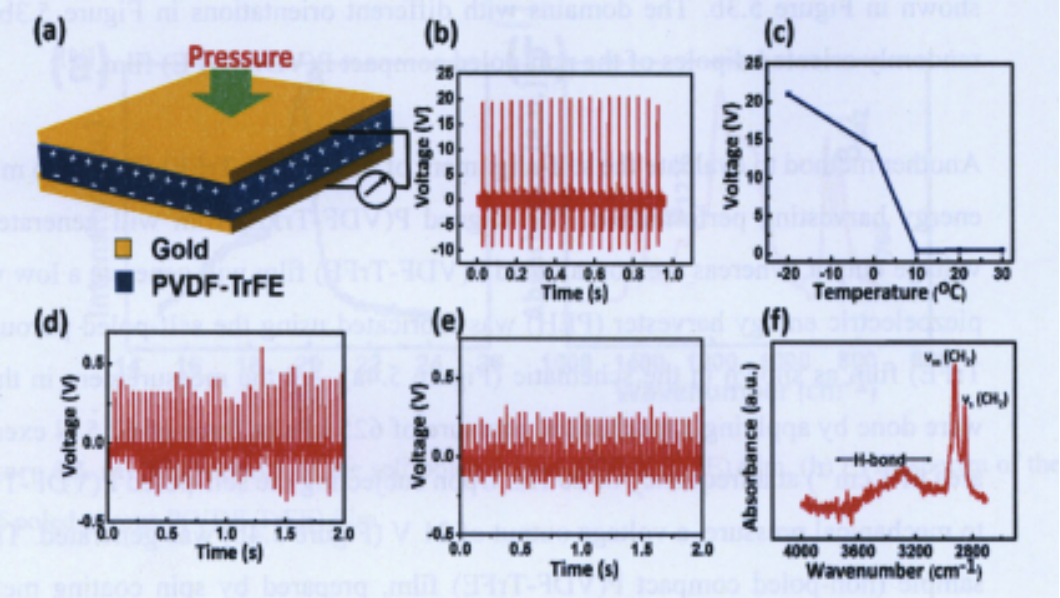

Figure 5.4. (a) Schematic diagram of self-poled porous P(VDF-TrFE) piezoelectric energy harvester. (b) The voltage output of self-poled porous P(VDF-TrFE) PEH, when subjected to a mechanical pressure of 625 kPa exerted at a frequency of 20 Hz. (c) The voltage output from the control sample (non-poled compact P(VDF-TrFE) film, prepared by spin coating method), when subjected to a mechanical pressure of 625 kPa, exerted at a frequency of 20 Hz. (d) The voltage output with the variation of fabrication temperature of the P(VDF-TrFE) film (at 50% RH), when subjected to a pressure of 625 kPa exerted at a frequency of 20 Hz. (e) The voltage output from the P(VDF-TrFE) film (fabricated at a temperature of −20 °C in the absence of humidity (< 5% RH)), when subjected to a pressure of 625 kPa exerted at a frequency of 20 Hz. (f) FTIR spectra demonstrating a peak at 3,600−3,120 cm^{-1} region verifying the presence of the hydrogen bond in the self-poled P(VDF-TrFE) film.

P(VDF-TrFE) comprises a repetitive unit block of CH_2CF_2; the electronegative fluorine and the electropositive hydrogen attached to the carbon backbone act as a molecular dipole. The electro-negative fluorine forms a hydrogen bond (H-bond) with the O-H group of the water molecules, as verified by the presence of a peak at 3600−3120 cm^{-1} region of the FTIR spectrum (Figure 5.4f).[15–17] H-bonding has been widely attributed to causing self-alignment in PVDF as reported in PVDF-AlO-rGO composites films,[16] PVDF-Cerium composites films,[18] and Langmuir Blodgett deposited PVDF films.[17] However, for films prepared by the typical breath figure technique (temperature = 25 °C and 50 % RH), the

interactions of water molecules (trapped inside polymer solution) with P(VDF-TrFE) molecular dipoles are not stable, as the thermal energy (at room temperature, 25 °C) is enough to create random motion of water molecules, which fails to align the dipoles during the nucleation of the P(VDF-TrFE) film. With our modified breath figure technique (temperature below 0 °C and 50 % RH), water vapor condenses onto the P(VDF-TrFE) solution and forms solid ice crystals, around which the P(VDF-TrFE) nucleates. The solid ice crystals form stable interactions with the P(VDF-TrFE) dipoles, which freeze the aligned dipoles (caused by the H-bonding interaction) during the nucleation process. Subsequently, when the water was evaporated from the P(VDF-TrFE) film (during drying at room temperature), a porous self-polarized P(VDF-TrFE) film was obtained. The self-polarization observed for the porous P(VDF-TrFE) film fabricated by our modified breath-figure technique, can be attributed to the stable H-bonding interaction between the solid ice crystals (water) molecular dipoles and the PVDF molecule which aligns the P(VDF-TrFE) dipoles at low-temperature (below 0 °C). The water content in the atmosphere leads to fluorine rich surface in the film, while it is likely that the glass substrate has negative charge stemming from hydroxyl groups, both leading to the directional orientation observed for the porous P(VDF-TrFE) film fabricated by our modified breath-figure technique. This work solves the pertinent difficulty of poling porous piezoelectric materials, which often leads to dielectric breakdown.[19] The modified breath figure technique provides a simple, scalable and cost-effective alternative, to the available piezoelectric polymer processing techniques, thus creating a disruptive technology to prepare piezoelectric energy harvesters and sensor devices. Self-poled P(VDF-TrFE) has been reported previously by Whiter et al. where they have prepared template-grown P(VDF-TrFE) nanowires. Due to the confined geometry of the templates leads to the formation of oriented β crystalline phase which leads to the self-alignment of the nanowire.[20] However, due to the complicated process of making nanowire by template growth method, the method is not scalable and cost effective.

5.2.3 Enhancement of the energy harvesting performance of the self-poled porous P(VDF-TrFE) film

5.2.3.1 Mechanism of energy generation of a triboelectric energy harvester

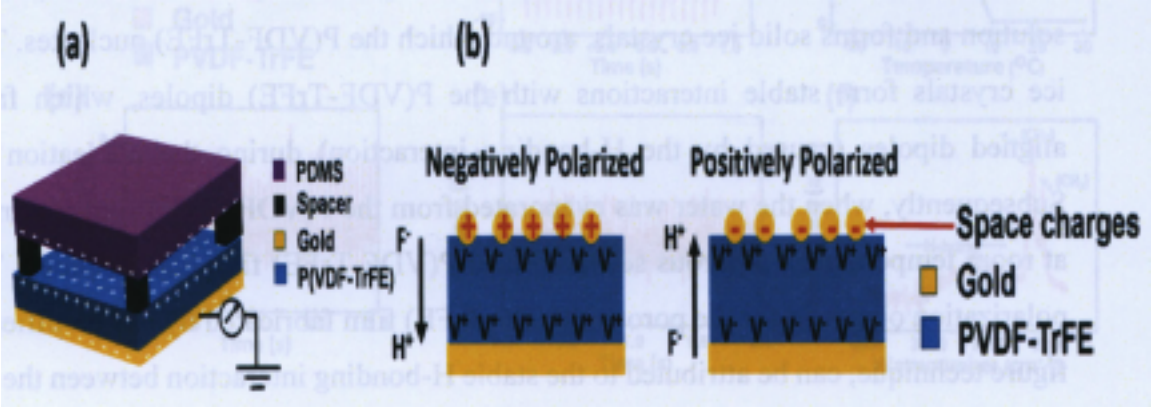

Figure 5.5. (a) Schematic diagram of the P(VDF-TrFE) TEH. (b) Schematic diagram of the negatively and positively polarized P(VDF-TrFE).

Figure 5.5a schematically illustrates the single electrode triboelectric energy harvester (TEH). The device consists of Au/P(VDF-TrFE) and polydimethylsiloxane (PDMS) film, separated by a spacer. The self-poled P(VDF-TrFE) (negatively polarized surface, Figure 5.5b) was used as the triboelectric positive material, and PDMS was used as the triboelectric negative material in the TEH. Figure 5.6 schematically depicts the complete process of mechanical pressure application and release of the self-poled P(VDF-TrFE) TEH. The working mechanism of the triboelectric pressure sensor is based on the coupling between the triboelectric effect and the electrostatic induction effect.[21–24] Before application of mechanical force, the self-poled P(VDF-TrFE) film and the PDMS were not in contact; hence there are no surface charges on the films. Upon application of a mechanical pressure, the self-poled P(VDF-TrFE) film comes in contact with the PDMS. Upon contact, the surface of self-poled P(VDF-TrFE) acquires a positive charge, and the surface of PDMS acquires negative charge due to the differences in their triboelectric polarity.[21,25] When the mechanical pressure is released, an air gap is formed between the two oppositely charged surface (PDMS and self-poled P(VDF-TrFE) film), creating an electrical potential difference between the metal contact and the ground. The potential difference resulted in a

transient flow of charge. Upon reapplication of the compressive force, the separation between the two oppositely charged surface reduces. Thus the electrical potential difference decreases, resulting in the flow of charge in the reverse direction.[26–28] Repetitive mechanical force generates multiple voltage outputs.

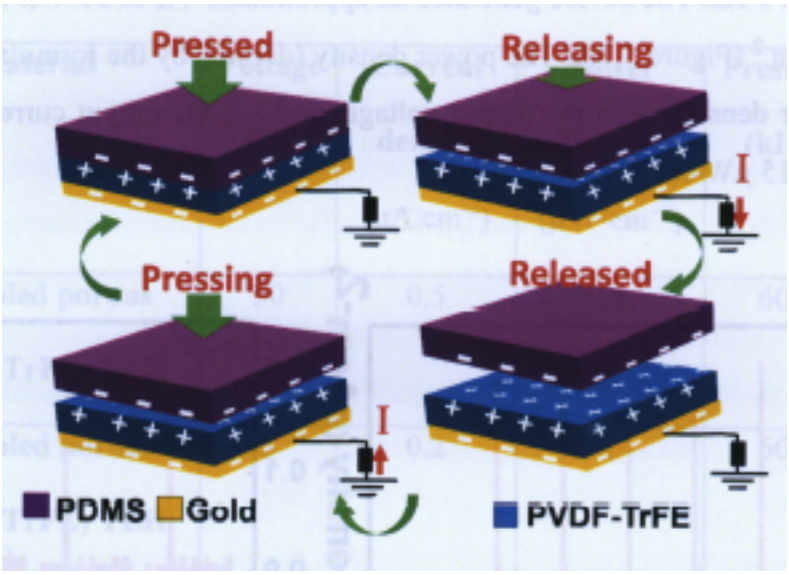

Figure 5.6. Schematic diagram of the mechanism of the P(VDF-TrFE) TEH.

5.3.2.2 Evaluation of energy generation

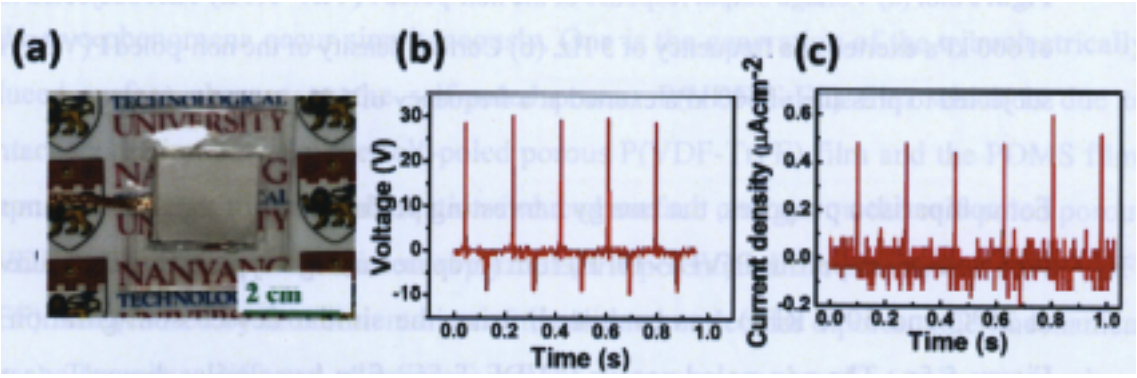

Figure 5.7. (a) Digital photo of the TEH device. (b) Voltage output of the self-poled P(VDF-TrFE) TEH subjected to pressure of 600 kPa exerted at a frequency of 5 Hz. (c) Current density of the self-poled P(VDF-TrFE) TEH subjected to pressure of 600 kPa exerted at a frequency of 5 Hz.

The energy harvesting performance of the self-poled P(VDF-TrFE) film was evaluated using the device configuration shown in Figure 5.5a. The digital photo of the device is shown in Figure 5.7a. The energy harvesting performance of the self-poled porous P(VDF-TrFE) was evaluated by exerting a compressive mechanical pressure of 600 kPa at a frequency of 5 Hz. The device generated an approximate V_{oc} of 30 V (Figure 5.7b), and I_{sc} of 0.5 $\mu A \cdot cm^{-2}$ (Figure 5.7c). The power density (defined by the formula $P = V \cdot I$, where P is the power density, V is the output voltage, and I is the output current density) of the device was 15 $\mu W \cdot cm^{-2}$.

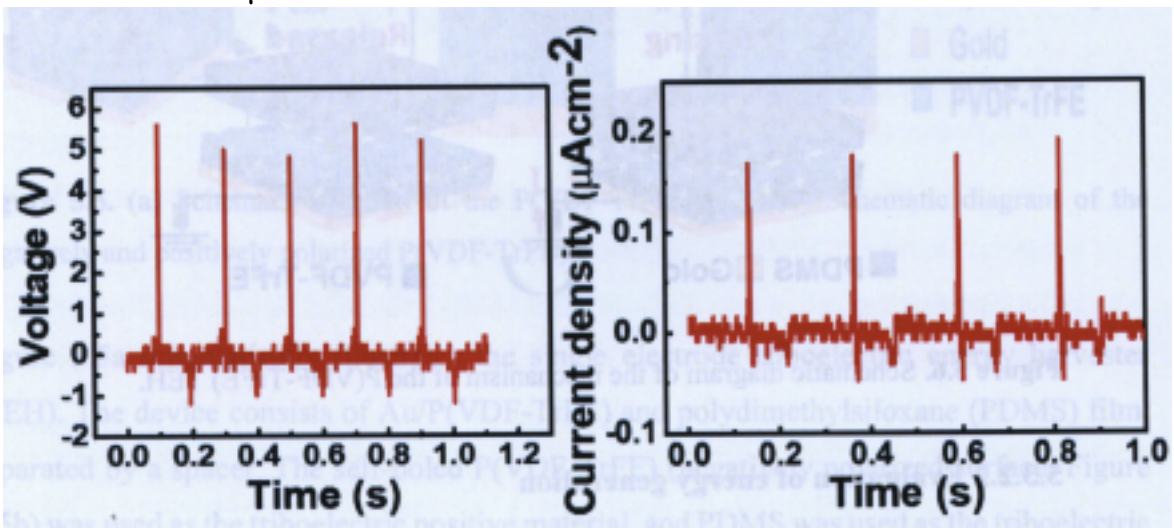

Figure 5.8. (a) Voltage output response of the non-poled P(VDF-TrFE) TEH subjected to a pressure of 600 kPa exerted at a frequency of 5 Hz. (b) Current density of the non-poled P(VDF-TrFE) TEH subjected to pressure of 600 kPa exerted at a frequency of 5 Hz.

For comparison purposes, the energy harvesting performance of the control sample (a TEH with non-poled porous P(VDF-TrFE) film (prepared using a typical breath-figure technique, at 25°C and 50% RH)) was evaluated, using the similar device configuration shown in Figure 5.5a. The non-poled porous P(VDF-TrFE) film has similar dimensions as the self-poled P(VDF-TrFE) film. The control sample generated an approximate V_{oc} of 5 V and current density of 0.2 $\mu A \cdot cm^{-2}$ at similar measurements conditions (Figure 5.8). The power density was 1.0 $\mu W \cdot cm^{-2}$. Thus, the self-poled porous P(VDF-TrFE) film exhibited a 15-fold enhancement in the power density as compared to that generated by the control sample.

The comparison of the self-poled and non-poled porous P(VDF-TrFE) TEH is summarized in Table 5.1.

Table 5.1. Comparison of the energy harvesting performance of the self-poled and non-poled porous P(VDF-TrFE) TEH.

Material	Voltage (V)	Current density ($\mu A \cdot cm^{-2}$)	Power Density ($\mu W \cdot cm^{-2}$)	Pressure (kPa)	Frequency (Hz)
Self-poled porous P(VDF-TrFE) TEH	30	0.5	15	600	5
Non-poled porous P(VDF-TrFE) TEH	5	0.2	1	600	5

The enhancement in the output performance of the self-poled porous P(VDF-TrFE) TEH can be attributed to the combined effect of piezoelectric polarization and triboelectric surface charge. When mechanical pressure is exerted on the self-poled porous P(VDF-TrFE) TEH, two phenomena occur simultaneously. One is the generation of the triboelectrically induced surface charges on the self-poled porous P(VDF-TrFE) film which is due to contact-separation between the self-poled porous P(VDF-TrFE) film and the PDMS film. Second is the generation of polarization-induced surface charges on the self-poled porous P(VDF-TrEF) film due to the internal piezoelectric potential difference across the P(VDF-TrEF) film (caused by the reorientation of the aligned molecular dipoles under mechanical stress). These two different phenomena are the factors governing the total output voltage generated by the self-poled porous P(VDF-TrFE) TEH upon the application of mechanical pressure. For the triboelectrically induced surface charges, voltage is generated when the two polymers (self-poled porous P(VDF-TrFE) film and PDMS film) approach and separate from each other. For the polarization-induced surface charges, voltage is generated when the two polymers are in contact (causing an internal piezoelectric potential difference

under mechanical stress). However, in the case of the non-poled porous P(VDF-TrFE) TEH, the output voltage is generated only due to the triboelectric surface charge. The combined surface charge of the triboelectric induced surface charge and polarization induced surface charge leads to the enhancement of voltage in case of the self-poled porous P(VDF-TrFE) TEH. This is validated by the charge transfer measurements of the self-poled and non-poled porous P(VDF-TrFE) TEH. The charge transfer for the self-poled porous P(VDF-TrFE) TEH is 4.3 times greater than the non-poled porous P(VDF-TrFE) TEH (Figure 5.9a and b). This validates the higher surface charges resulting from the combined effect of the piezoelectric polarization and the triboelectric effect. This is further evident from the larger peak width (5 times wider) of the voltage output signal of the self-poled P(VDF-TrFE) TEH compared to that of the non-poled P(VDF-TrFE) TEH (Figure 5.9c and d). The wider peak

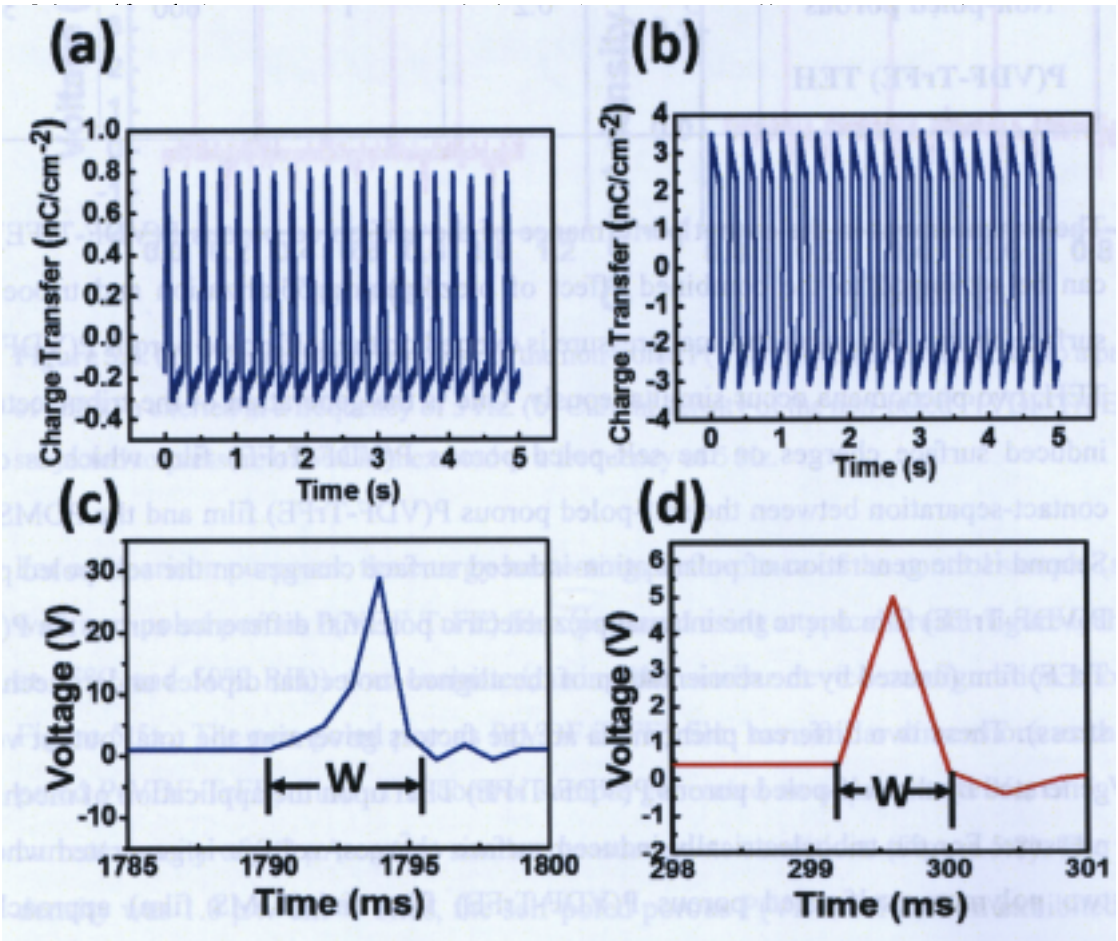

Figure 5.9. (a) Charge transfer of self-poled porous P(VDF-TrFE) TEH subjected to pressure of 600 kPa exerted at a frequency of 5 Hz. (b) Charge transfer of non-poled porous P(VDF-TrFE) TEH

subjected to pressure of 600 kPa exerted at a frequency of 5 Hz. (c) The voltage output pulse of the self-poled porus P(VDF-TrFE) TEH subjected to a pressure of 600 kPa exerted at a frequency of 5 Hz. (b) The voltage output pulse of the non-poled P(VDF-TrFE) TEH subjected to a pressure of 600 kPa exerted at a frequency of 5 Hz.

Moreover, the device exhibits exceptionally high stability in both the medium- and high-pressure ranges, by sustaining a dynamic mechanical pressure of 30 kPa for 20,000 cycles and a pressure of 350 kPa for 6000 cycles without any degradation in the performance (Figure 5.10a and b). High atmospheric humidity reduces the surface charges on the triboelectric material and hence affects the performance of a triboelectric device. The device is fully sealed to ensure stable performance of the device under different levels of humidity (Figure 5.10c). The device is sealed by applying a thin layer of silicone rubber, at the junction of PDMS and spacer (VHB tape). This prevents the water vapor from interaction with the surface of PDMS and P(VDF-TrFE) thus ensuring stable performance.

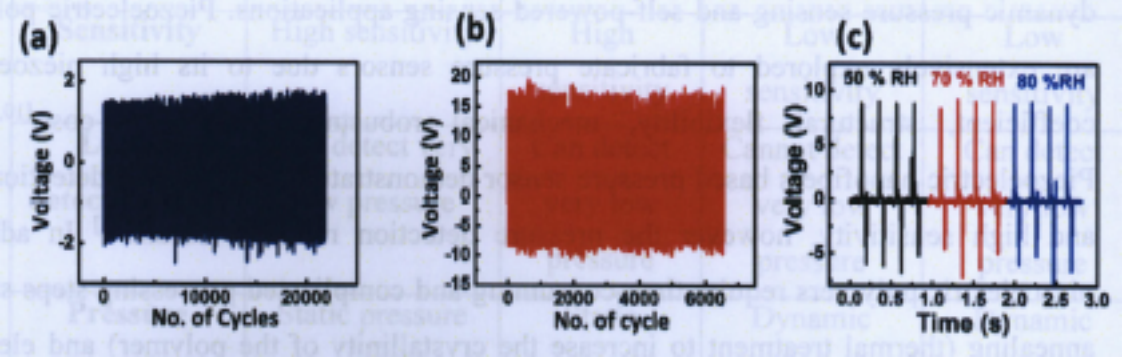

Figure 5.10. (a) Stability of self-poled porous P(VDF-TrFE) TEH for medium-pressure range (30 kPa). (d) Stability of self-poled porous P(VDF-TrFE) TEH for high-pressure range (350 kPa). (c) The voltage output of the self-poled P(VDF-TrFE) TEH at different % relative humidity (%RH) at a mechanical pressure 150 kPa exerted at a frequency of 5 Hz.

5.3 Application - self-powered wide-range pressure sensor

Self-powered, interactive, maintenance free and multifunctional operations are the key requirement for the realization of next-generation electronics for potential application in health monitoring, sensor networks, smart robotics and sports application.[1–3] One of the key components for the next-generation electronics is a pressure monitoring system,

capable of detecting a wide range of pressure with high sensitivity. There is an increasing need for materials and devices for precise and wide range (ultra-low (<1 kPa), low (1-10 kPa), medium (10-100 kPa) and high (>100 kPa)) dynamic pressure detection for a spectrum of different applications ranging from simple human touch to heavy object manipulation.[29,30] Extensive works have been carried out to fabricate precision pressure sensors, employing various mechanisms such as capacitive,[31–33] resistive,[34–36] piezoelectric,[10,37–41] and triboelectric.[4–6,42–44] Resistive and capacitive-based pressure sensors have demonstrated high sensitivity and rapid response in the low and medium pressure ranges. However, most of these pressure sensors are incapable of detecting a wide range of pressure with high sensitivity due to the inferior sensitivity at high-pressure ranges.[29,32–34,36] Moreover, its operation is only confined to static pressure monitoring, and it requires an external power source, failing to realize a self-powered or maintenance-free pressure monitoring system. Piezoelectric and triboelectric pressure sensors are used for dynamic pressure sensing and self-powered sensing applications. Piezoelectric polymers are extensively explored to fabricate pressure sensors due to its high piezoelectric coefficient, structural flexibility, mechanical robustness, and low cost.[10,41,45,46] Piezoelectric nanofibers based pressure sensor demonstrated excellent low detection limit and high sensitivity, however the pressure detection range is small.[41] In addition, piezoelectric polymers require time-consuming and complicated processing steps such as annealing (thermal treatment to increase the crystallinity of the polymer) and electrical poling (application of electric field to align the dipoles) which increases the cost and constraints the integration of polymer into different geometries and functional devices.[47,48] Recently, triboelectric energy harvester (TEH) reported by Wang et al. has been a promising candidate for pressure sensing application due to its high sensitivity, low detection limit and its use in a wide variety of application ranging from tactile imaging, real-time tactile mapping, security surveillance and healthcare monitoring.[4–6] However, the pressure detection range of the triboelectric pressure sensor is small, due to the saturation of output voltage at higher-pressure.[5,6,44] Thus, a major problem pertaining to all kinds of pressure sensors is the inability to sustain the high sensitivity for a wide range of pressure. Table 5.2 compares different characteristics of various pressure sensor. Table 5.3 shows the works reported on self-powered presser sensor including piezoelectric and

triboelectric pressure sensor. It is hypothesized that by utilizing the combined effect of piezoelectric polarization and triboelectric surface charge, the saturation pressure of the triboelectric energy harvester can be increased, thus making it capable of detecting a wide range of pressure with high sensitivity. Herein, the self-polarized porous P(VDF-TrFE) TEH was used as a self-powered pressure sensor.

Table 5.2. Comparison of different characteristics of various pressure sensor.

Pressure sensor	**Capacitive**	**Resistive**	**Piezoelectric**	**Triboelectric**
External Power	Required external power	Required external power	Do not required external power	Do not required external power
Sensitivity	High sensitivity	High sensitivity	Low sensitivity	Low sensitivity
Lowest detection limit	Can detect very low pressure	Can detect very low pressure	Cannot detect very low pressure	Can detect very low pressure
Pressure detection	Static pressure	Static pressure	Dynamic pressure with low and high frequency	Dynamic pressure with high frequency
Range of pressure detect	Narrow range of pressure	Narrow range of pressure	Limited range of pressure	Limited range of pressure till 100 kPa

5.3.1 Evaluation of pressure sensor

5.3.1.1 Evaluation of non-poled porous P(VDF-TrFE) pressure sensor

For comparison, the pressure-sensing performance of the non-poled P(VDF-TrFE) film (prepared using a typical breath-figure technique, at 25°C and 50% RH) was analyzed, using the same device configuration as shown in Figure 5.5a. For low (0.05–5 kPa) and medium (5–50 kPa) pressures (Figure 5.11a and b), the non-poled P(VDF-TrFE) pressure sensor exhibits a linear increase in the output voltage with an increase in the dynamic pressure (exerted at a frequency of 5 Hz). The sensitivities of the non-poled P(VDF-TrFE) pressure sensor for the low- and medium-pressure ranges are 0.089 and 0.053 $V \cdot kPa^{-1}$, respectively. The sensitivity was calculated from the voltage response slope (Figure 5.11a and b). This device exhibits good sensitivity in the lower- and medium-pressure ranges. However, as the pressure was increased beyond 50 kPa, the output voltage was found to saturate (Figure 5.11c), thus the sensitivity (0.0002 $V \cdot kPa^{-1}$) of the non-poled P(VDF-TrFE) pressure sensor degrades, the same as that reported in other works on triboelectric nanogenerators.[5,28,49] The output voltage generated by a triboelectric energy harvester depends on the surface charge density, which in turn is affected by the interfacial contact area between the two polymers.[43] With a gradual increase in the mechanical pressure, the interfacial contact area increases due to macroscopic deformation at the interface between the two polymers. At a certain saturation pressure, the two polymers are in complete contact with each other, thus saturating the triboelectrically induced surface charge, which restrains any further increase in the output voltage. The saturation pressure depends on the polymer material and the interfacial surface area.[50] The saturation pressure (usually around 5 to 100 kPa for TEH) often limits the operation of TEH as a wide-range pressure sensor.[5,28,49] This problem can be circumvented by using our self-polarized P(VDF-TrFE) pressure sensor (described below), which extends the limits of the saturation pressure.

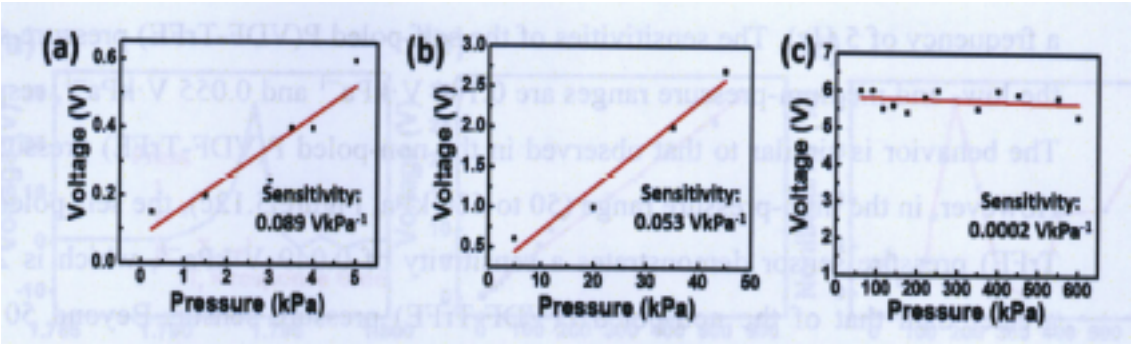

Figure 5.11. (a) Voltage output of the non-poled P(VDF-TrFE) pressure sensor for low-pressure range (0.1 to 5 kPa). (c) Voltage output of the non-poled P(VDF-TrFE) pressure sensor for medium pressure range (5 to 50 kPa). (d) Voltage output of the non-poled P(VDF-TrFE) pressure sensor for high-pressure range (50 to 600 kPa).

5.3.1.2 Evaluation of self-poled porous P(VDF-TrFE) pressure sensor

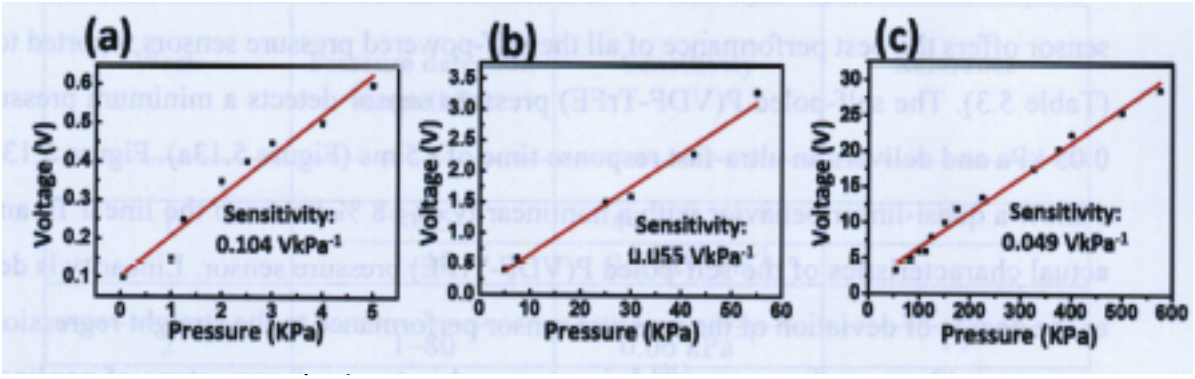

Figure 5.12 (a) Voltage output of self-poled P(VDF-TrFE) pressure sensor for low-pressure range (0.05 to 5 kPa). (e) Voltage output of self-poled P(VDF-TrFE) pressure sensor for medium-pressure range (5 to 60 kPa). (f) Voltage output of self-poled P(VDF-TrFE) pressure sensor for high-pressure range (60 to 600 kPa).

The pressure-sensing performance of the self-poled P(VDF-TrFE) film was evaluated using the device configuration shown in Figure 5.5a. For low (0.05–5 kPa) and medium (5–50 kPa) pressures (Figure 5.12a and b), the self-poled P(VDF-TrFE) pressure sensor exhibits a linear increase in the output voltage with an increase in the dynamic pressure (exerted at

a frequency of 5 Hz). The sensitivities of the self-poled P(VDF-TrFE) pressure sensor for the low- and medium-pressure ranges are 0.104 $V \cdot kPa^{-1}$ and 0.055 $V \cdot kPa^{-1}$, respectively. The behavior is similar to that observed in the non-poled P(VDF-TrFE) pressure sensor. However, in the high-pressure range (50 to 600 kPa, Figure 5.12c), the self-poled P(VDF-TrFE) pressure sensor demonstrates a sensitivity of 0.049 $V \cdot kPa^{-1}$, which is 245 times greater than that of the non-poled P(VDF-TrFE) pressure sensor. Beyond 50 kPa, the triboelectrically induced surface charge saturates, as the PDMS film and self-poled P(VDF-TrFE) film are completely in contact with each other (as indicated by the non-poled P(VDF-TrFE) pressure sensor, (Figure 5.11c). Notably, beyond 50 kPa, the piezoelectrically induced surface charge increases due to the increment of the internal piezoelectric potential with the increase in the mechanical pressure. Beyond the saturation pressure (50 kPa), the polarization-induced surface charge dominates, such that the output voltage continues to increase, while the triboelectrically induced surface charge is saturated. Thus, the self-poled P(VDF-TrFE) pressure sensor can detect a wide range of pressures from 0.05 to 600 kPa without any loss of sensitivity. To the best of our knowledge, taking into account both the wide pressure-sensing range and the sensitivity, the self-poled P(VDF-TrFE) pressure sensor offers the best performance of all the self-powered pressure sensors reported to date (Table 5.3). The self-poled P(VDF-TrFE) pressure sensor detects a minimum pressure of 0.05 kPa and delivers an ultra-fast response time of <5 ms (Figure 5.13a). Figure 5.13b and c show a quasi-linear behavior with a nonlinearity of ±8 % between the linear fit and the actual characteristics of the self-poled P(VDF-TrFE) pressure sensor. Linearity is defined as the degree of deviation of the pressure sensor performance to the straight regression line over a specific operating range.[30] It is expressed in terms of percentage of nonlinearity. The nonlinearity in percentage is calculated using the following equation 5.1.[51]

$$\text{Nonlinearity (\%)} = \frac{|V_{\text{deviation}}|}{V_{\text{max}}} \times 100\% \qquad (5.1)$$

where, $|V_{\text{deviation}}|$ is the absolute deviation between the measured output and the ideal linear output. V_{max} is the maximum full-scale output.

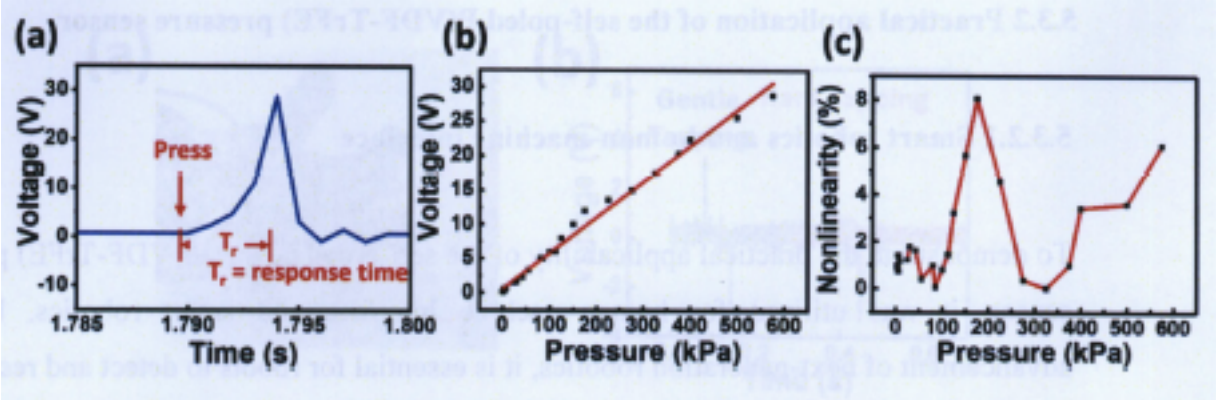

Figure 5.13. (a) Response time of self-poled P(VDF-TrFE) pressure sensor upon application of mechanical pressure of 600 kPa at a frequency of 5 Hz. (b) Variation of the output voltage of the self-poled P(VDF-TrFE) TEH with a range from 0.05 to 600 kPa. (c) Voltage error in percentage between linear fit and actual characteristics of the TEH for the range of 0.05 to 600 kPa.

Table 5.3. Sensitivity and pressure range of various self-powered pressure sensors

Work	Pressure detection range (kPa)	Sensitivity	Reference
1	<0.5	44 mV·Pa^{-1}	[44]
	1–10	0.5 mV·Pa^{-1}	
2	1–80	0.06 kPa^{-1}	[5]
3	3–6.2	0.04 V·kPa^{-1}	[6]
4	0.4–2	1.1 V·kPa^{-1}	[41]
5	<30	2.1 μS·kPa^{-1}	[52]
	0.05–5	0.104 V·kPa^{-1}	This work
6	5–50	0.055 V·kPa^{-1}	
	50–600	0.049 V·kPa^{-1}	

5.3.2 Practical application of the self-poled P(VDF-TrFE) pressure sensor

5.3.2.1 Smart robotics and human-machine interface

To demonstrate the practical applicability of the self-poled porous P(VDF-TrFE) pressure sensor, it was utilized for human-machine interface and smart robotics. For the advancement of next-generation robotics, it is essential for robots to detect and respond to human touch. The pressure sensor (device area = 4 × 2 cm^2) was attached to the finger of a humanoid robot (Figure 5.13a), to detect pressure exerted by human touch. The pressure sensor generates a voltage of 3.3 V and 5.3 V for gentle and hard finger tapping respectively (Figure 5.13b). As the force of finger tapping increases, the contact area between PDMS and P(VDF-TrFE) film increases, thus increasing the output voltage. This enables the humanoid robot to precisely feel and respond to human touch, thus extending the realms of the human-machine interface. To achieve a fully autonomous humanoid robot, which can sustain without human intervention, it is essential for the humanoid robot to detect and self-monitor its motion. This can be achieved by attaching the pressure sensor (device area = 5 × 5 cm^2) to the foot of a humanoid robot (Figure 5.13c). The pressure sensor generates a voltage of 8.4 V and 19.6 V upon slow and fast foot tapping respectively (Figure 5.13d). As the foot tapping speed increases, the output voltage generated from the pressure sensor increases, thus precisely differentiating between the different speed of humanoid motion. The fabricated pressure can be effectively deployed to monitor the walking speed of the humanoid robot, thus making the robot autonomous and self-sustaining.

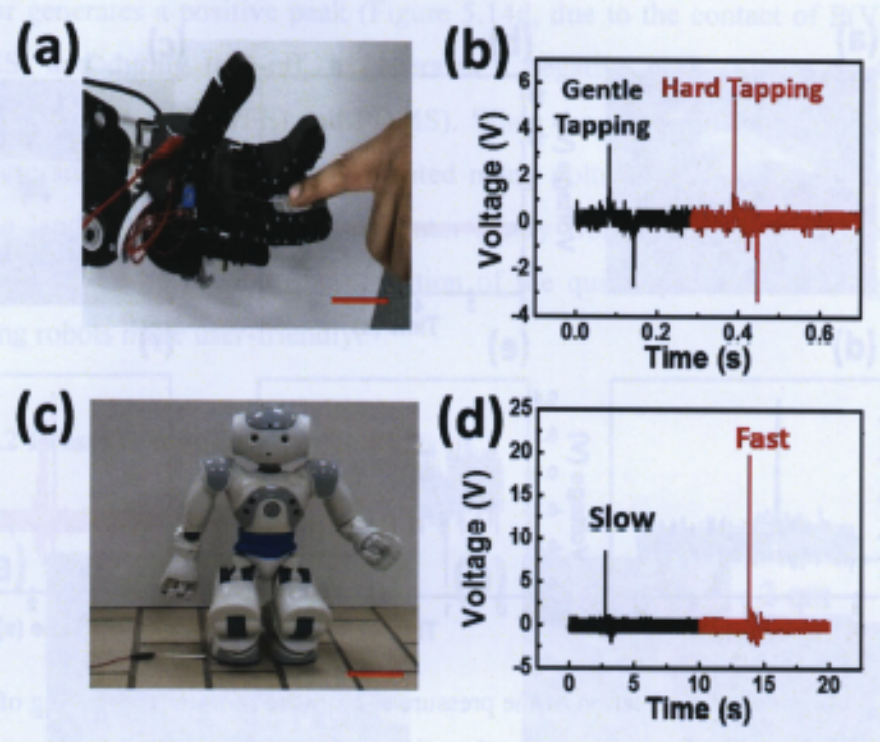

Figure 5.13. Practical application of self-poled porous P(VDF-TrFE) pressure sensor for human-machine interface and smart robotics. (a) Pressure sensor attached to the finger of the humanoid robot to detect pressure exerted by human touch. Scale bar: 4 cm. (b) Voltage output generated from a gentle and hard finger tapping on pressure sensor attached to humanoid robot finger. (c) Photograph of pressure sensor attached to the foot of humanoid robot to detect robot motion. Scale bar: 10 cm. (d) Voltage output generated during slow and fast foot tapping of the humanoid robot.

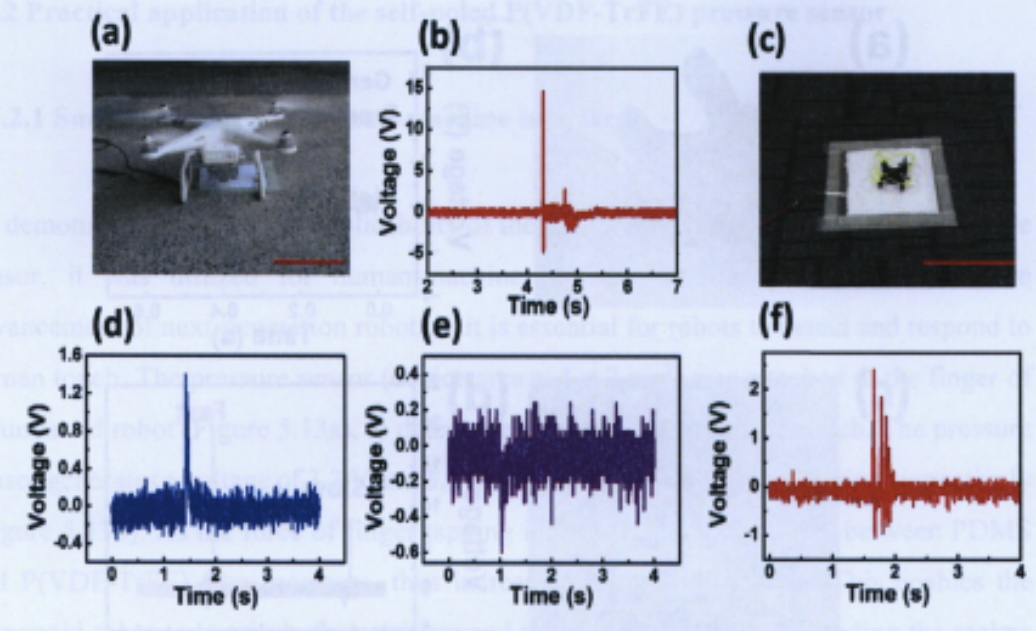

Figure 5.14. Practical application of the pressure sensor is to monitor the landing of a quadcopter robot. (a) Pressure sensor application to detection of landing pressure of large quadcopter robot. Scale bar: 20 cm. (b) Voltage output detected during the landing of the large quadcopter robot. (c) Photograph of the pressure sensor to monitor the landing of a mini quadcopter robot. Scale bar: 20 cm. (d) Voltage output detected during the smooth landing of the mini quadcopter robot on the pressure sensor. (e) Voltage output detected during take-off of the mini quadcopter robot from the pressure sensor. (f) Voltage output detected during the crash landing of the mini quadcopter robot on the pressure sensor.

A quadcopter robot is often used at some distance away from the site of the operator. Thus, it is essential for the operator to get accurate information about the landing of the quadcopter. The pressure sensor (device area = 20 × 20 cm^{-2}) was deployed to obtain information about the landing of a quadcopter by analyzing the pressure exerted by the quadcopter on the pressure sensor (Figure 5.14). A large quadcopter (weight = 1.2 kg) generates a voltage of 14.6 V upon landing (Figure 5.14 and b), and a mini quadcopter (weight = 15.3 g) generates a voltage of 1.4 V upon landing (Figure 5.14c-f), thus demonstrating the workability of the pressure sensor for both large and mini quadcopter. The pressure sensor was also used to detect various types of landing, such as smooth-landing, crash-landing and take-off (Figure 5.14d-f). During smooth landing, the pressure

sensor generates a positive peak (Figure 5.14d, due to the contact of P(VDF-TrFE) and PDMS) and during take-off, it generates a negative peak (Figure 5.14e, due to the separation of P(VDF-TrFE) and PDMS). When the quadcopter was crashed landed, the pressure sensor (Figure 5.14f) generated many voltage peaks due to vibrations created during landing. This allows the operator (away from the sight of the robot) to obtain accurate information about the condition of the quadcopter robot during landing, thus making robots more user-friendly.

5.3.2.2 Pressure mapping application

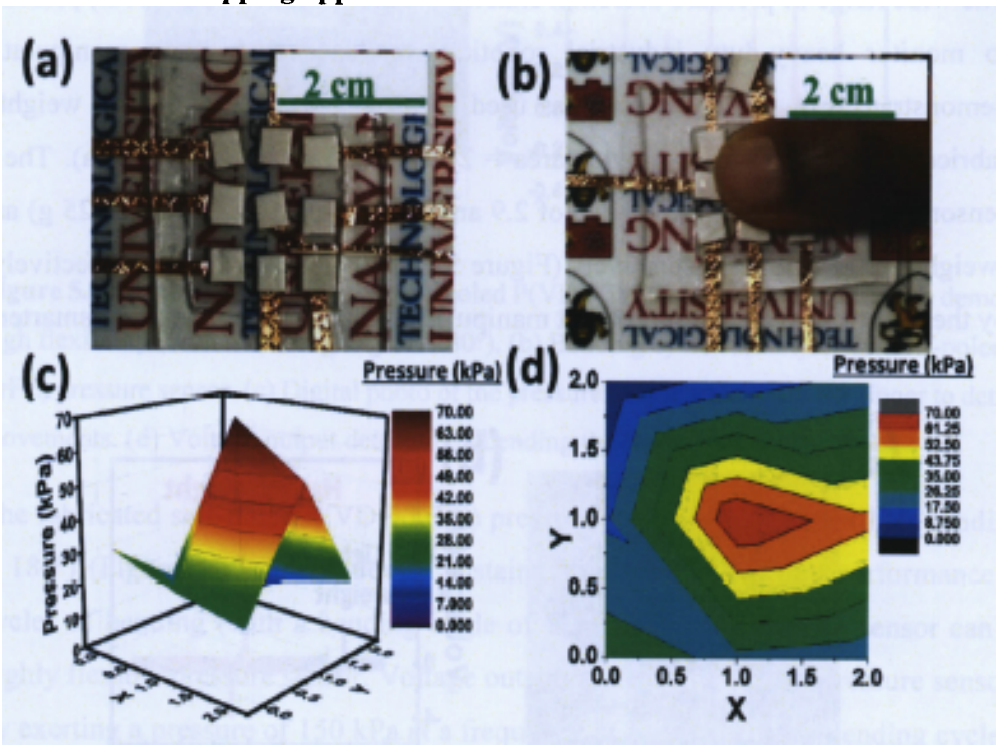

Figure 5.15. (a) The self-poled P(VDF-TrFE) pressure sensor arranged in a matrix for the pressure-mapping application. (b) Application of pressure on to the self-poled P(VDF-TrFE) pressure sensor by finger tapping. (c) 3D pressure map of pressure exerted on self-poled P(VDF-TrFE) pressure sensor upon finger tapping. (d) 2D pressure map of pressure exerted on self-poled P(VDF-TrFE) pressure sensor upon finger tapping.

For the application of pressure mapping, small self-poled P(VDF-TrFE) pressure sensor (area = 0.5 cm × 0.5 cm) was fabricated. The method followed is similar to as described in

the experimental section, except smaller glass substrate (area = 0.5 cm × 0.5 cm) was used for drop-casting the P(VDF-TrFE) solution. For pressure mapping application, 9 small pressure sensors are arranged in a matrix within an area of 2 cm × 2 cm (Figure 5.15a and b). On finger tapping the pressure sensor, voltage response from each pressure sensors are recorded simultaneously. The voltage response is represented in terms of pressure exerted over the area as shown in the 3D and 2D mapping (Figure 5.15c and d).

5.3.2.3 Heavy object manipulation

The wide range of pressure detection enables the self-poled P(VDF-TrFE) pressure sensor to monitor heavy-duty industrial robotic arm (used for object manipulation). To demonstrate this, a robotic arm was used to place objects of different weights on the fabricated pressure sensor (device area = 20 cm × 20 cm) (Figure 5.16a). The pressure sensor generated an output voltage of 2.9 and 11.4 V for light (weight = 25 g) and heavy (weight = 200 g) loads respectively (Figure 5.16b). This feature can be effectively utilized by the robotic arm to monitor object manipulation, thus making the robot smarter.

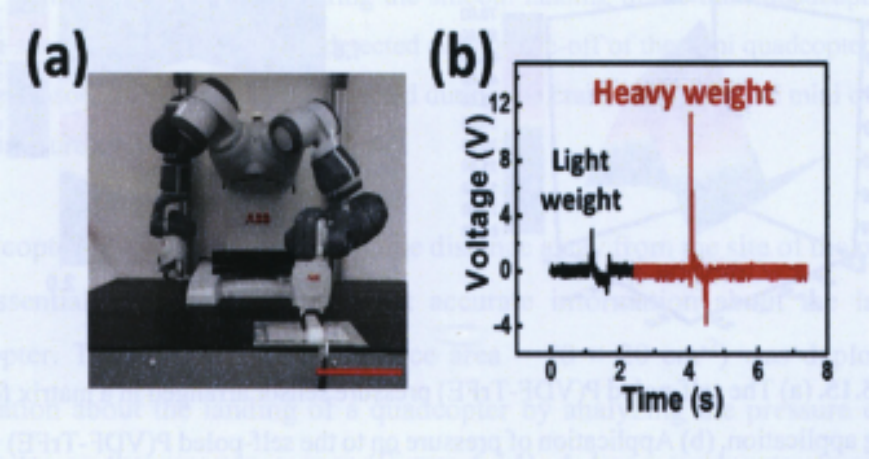

Figure 5.16. (a) Photograph of the self-poled P(VDF-TrFE) pressure sensor to detect pressure exerted by a robotic arm during object manipulation. Scale bar: 20 cm. (b) Voltage output during objects (light and heavy weight) manipulation (loading and unloading) on the self-poled P(VDF-TrFE) pressure sensor by the robotic arm.

5.3.2.4 Flexible pressure sensor

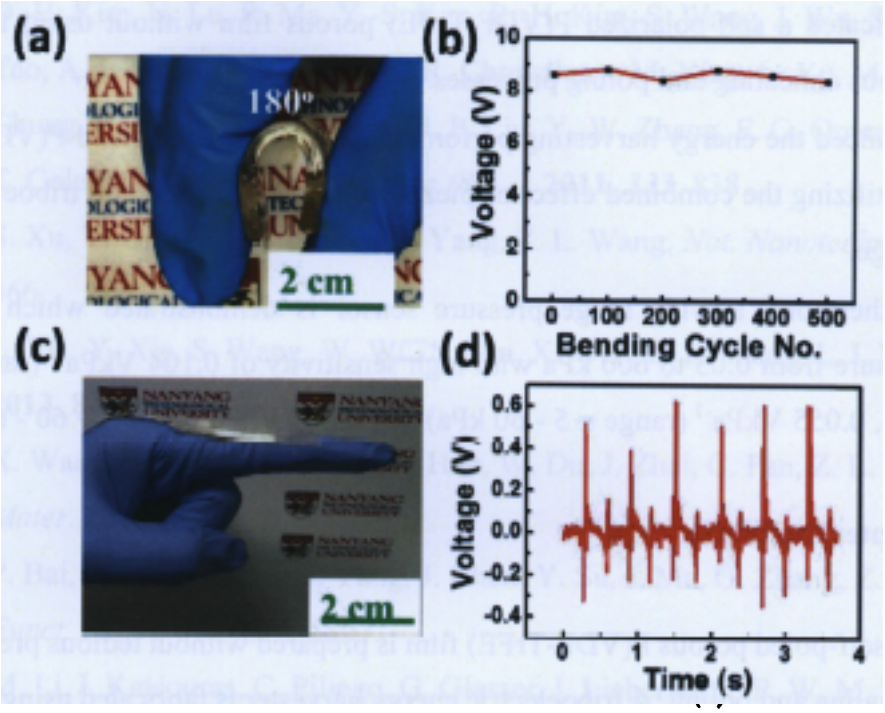

Figure 5.17. (a) Digital photo of the self-poled P(VDF-TrFE) pressure sensor device demonstrating high flexibility (with a bending angle = 180°). (b) Bending cycle stability of the self-poled P(VDF-TrFE) pressure sensor. (c) Digital photo of the pressure sensor attached to the finger to detect finger movements. (d) Voltage output detected by bending the finger.

The fabricated self-poled P(VDF-TrFE) pressure sensor is highly flexible (bending angle = 180°) (Figure 5.17a). The device sustains its energy harvesting performance for 500 cycles of bending (with a bending angle of 180°), thus the pressure sensor can act as a highly flexible pressure sensor. Voltage output is measured for the pressure sensor device by exerting a pressure of 150 kPa at a frequency of 5 Hz after each bending cycle (Figure 5.17b). Moreover, the pressure sensor generates voltage upon bending. This characteristic is utilized by fabricating a human motion detection sensor. Figure 5.17c shows the detection of finger movements by the pressure sensor. The bending of finger facilitates contact-separation between the PDMS and the self-poled P(VDF-TrFE) film, which generates an output voltage (Figure 5.17d).

5.4 Principal outcomes

- Fabricated a self-polarized P(VDF-TrFE) porous film without using the costly and tedious annealing and poling processes.
- Enhanced the energy harvesting performance of the self-polarized P(VDF-TrFE) film by utilizing the combined effect of piezoelectric polarization and triboelectric surface charge.
- Furthermore, a wide range pressure sensor is demonstrated which can measure pressure from 0.05 to 600 kPa with high sensitivity of 0.104 $VkPa^{-1}$ (range = 0.05 - 5 kPa), 0.055 $VkPa^{-1}$ (range = 5 - 60 kPa) and 0.049 $VkPa^{-1}$ (range = 60 - 600 kPa).

5.5 Chapter Summary

A novel self-poled porous P(VDF-TrFE) film is prepared without tedious preparatory steps like annealing and poling. A triboelectric energy harvester is fabricated using the self-poled porous P(VDF-TrFE) film which showed enhanced energy harvesting performance due to the combined effect of piezoelectric polarization and triboelectric surface charges, thus proving our hypothesis. Furthermore, a wide range pressure sensor was fabricated using the self-poled porous P(VDF-TrFE) film. The combined effect extends the limit of saturation pressure for the self-poled porous P(VDF-TrFE) based triboelectric nanogenerator. This work provides a new dimension to pressure sensors, by making it possible to detect a wide range of pressure (0.05 to 600 kPa) with high sensitivity; thus extending the realms of pressure monitoring from gentle human touch to heavy object manipulation. Taking into account both the wide pressure sensing range and the sensitivity, the self-polarized P(VDF-TrFE) pressure sensor shows the best performance amongst all the self-powered pressure sensors reported so far. The demonstration of a wide range pressure sensor opens up new possibilities to precisely detect pressure for a spectrum of applications (health monitoring, sensor networks, smart robotics and sports application), thus taking a huge step forward towards the realization of next-generation sensing devices.

References

[1] J. a Rogers, *Nature* **2010**, *468*, 177.

[2] D.-H. Kim, N. Lu, R. Ma, Y.-S. Kim, R.-H. Kim, S. Wang, J. Wu, S. M. Won, H. Tao, A. Islam, K. J. Yu, T. Kim, R. Chowdhury, M. Ying, L. Xu, M. Li, H.-J. Chung, H. Keum, M. McCormick, P. Liu, Y.-W. Zhang, F. G. Omenetto, Y. Huang, T. Coleman, J. A. Rogers, *Science (80-.).* **2011**, *333*, 838.

[3] S. Xu, Y. Qin, C. Xu, Y. Wei, R. Yang, Z. L. Wang, *Nat. Nanotechnol.* **2010**, *5*, 366.

[4] L. Lin, Y. Xie, S. Wang, W. Wu, S. Niu, X. Wen, Z. L. Wang, L. I. N. E. T. Al, **2013**, 8266.

[5] X. Wang, H. Zhang, L. Dong, X. Han, W. Du, J. Zhai, C. Pan, Z. L. Wang, *Adv. Mater.* **2016**, *28*, 2896.

[6] P. Bai, G. Zhu, Q. Jing, J. Yang, J. Chen, Y. Su, J. Ma, G. Zhang, Z. L. Wang, *Adv. Funct. Mater.* **2014**, *24*, 5807.

[7] M. Li, I. Katsouras, C. Piliego, G. Glasser, I. Lieberwirth, P. W. M. Blom, D. M. de Leeuw, *J. Mater. Chem. C* **2013**, *1*, 7695.

[8] M.-C. García-Gutiérrez, A. Linares, I. Martín-Fabiani, J. J. Hernández, M. Soccio, D. R. Rueda, T. a Ezquerra, M. Reynolds, *Nanoscale* **2013**, *5*, 6006.

[9] X. Li, Y.-F. Lim, K. Yao, F. E. H. Tay, K. H. Seah, *Phys. Chem. Chem. Phys.* **2013**, *15*, 515.

[10] J. H. Lee, H. J. Yoon, T. Y. Kim, M. K. Gupta, J. H. Lee, W. Seung, H. Ryu, S.-W. Kim, *Adv. Funct. Mater.* **2015**, 3203.

[11] Z. Pi, J. Zhang, C. Wen, Z. B. Zhang, D. Wu, *Nano Energy* **2014**, *7*, 33.

[12] D. Y. Kusuma, C. A. Nguyen, P. S. Lee, *J. Phys. Chem. B* **2010**, *114*, 13289.

[13] A. Zhang, H. Bai, L. Li, *Chem. Rev.* **2015**, *115*, 9801.

[14] A. Venault, Y. Chang, D. M. Wang, D. Bouyer, *Polym. Rev.* **2013**, *53*, 568.

[15] S. Jana, S. Garain, S. Sen, D. Mandal, *Phys. Chem. Chem. Phys. Phys. Chem. Chem. Phys* **2015**, *17*, 17429.

[16] S. K. Karan, R. Bera, S. Paria, A. K. Das, S. Maiti, A. Maitra, B. B. Khatua, *Adv. Energy Mater.* **2016**, 1601016.

[17] S. Chen, X. Li, K. Yao, F. E. H. Tay, A. Kumar, K. Zeng, *Polymer (Guildf).* **2012**,

53, 1404.

[18] S. Garain, T. K. Sinha, P. Adhikary, K. Henkel, S. Sen, S. Ram, C. Sinha, D. Schmeißer, D. Mandal, *ACS Appl. Mater. Interfaces* **2015**, *7*, 1298.

[19] L. Pardo, A. García, K. Brebøl, D. Piazza, C. Galassi, *J. Electroceramics* **2007**, *19*, 413.

[20] R. A. Whiter, V. Narayan, S. Kar-Narayan, *Adv. Energy Mater.* **2014**, *4*, 1.

[21] Z. L. Wang, L. Lin, J. Chen, S. Niu, Y. Zi, *Triboelectric Nanogenerators*, Springer International Publishing, Switzerland, **2016**.

[22] Z. L. Wang, J. Chen, L. Lin, *Energy Environ. Sci.* **2015**, *8*, 2250.

[23] K. Y. Lee, M. K. Gupta, S. W. Kim, *Nano Energy* **2015**, *14*, 139.

[24] Z. L. Wang, *Faraday Discuss.* **2014**, *176*, 447.

[25] J. H. Lee, R. Hinchet, T. Y. Kim, H. Ryu, W. Seung, H. J. Yoon, S. W. Kim, *Adv. Mater.* **2015**, *27*, 5553.

[26] F. R. Fan, W. Tang, Z. L. Wang, *Adv. Mater.* **2016**, 1.

[27] J. Chun, J. W. Kim, W. Jung, C.-Y. Kang, S.-W. Kim, Z. L. Wang, J. M. Baik, *Energy Environ. Sci.* **2015**, *8*, 3006.

[28] S. Wang, L. Lin, Z. L. Wang, *Nano Energy* **2015**, *11*, 436.

[29] H. Tian, Y. Shu, X. F. Wang, M. A. Mohammad, Z. Bie, Q. Y. Xie, C. Li, W.-T. Mi, Y. Yang, T. L. Ren, *Sci. Rep.* **2015**, *5*, 8603.

[30] Y. Zang, F. Zhang, C. Di, D. Zhu, *Mater. Horiz.* **2015**, *2*, 140.

[31] D. J. Lipomi, M. Vosgueritchian, B. C. K. Tee, S. L. Hellstrom, J. A. Lee, C. H. Fox, Z. Bao, *Nat. Nanotechnol.* **2011**, *6*, 788.

[32] G. Schwartz, B. C.-K. Tee, J. Mei, A. L. Appleton, D. H. Kim, H. Wang, Z. Bao, *Nat. Commun.* **2013**, *4*, 1859.

[33] S. C. B. Mannsfeld, B. C.-K. Tee, R. M. Stoltenberg, C. V. H.-H. Chen, S. Barman, B. V. O. Muir, A. N. Sokolov, C. Reese, Z. Bao, *Nat. Mater.* **2010**, *9*, 859.

[34] J. Park, Y. Lee, J. Hong, M. Ha, Y. Do Jung, H. Lim, S. Y. Kim, H. Ko, *ACS Nano* **2014**, *8*, 4689.

[35] T. Yamada, Y. Hayamizu, Y. Yamamoto, Y. Yomogida, A. Izadi-Najafabadi, D. N. Futaba, K. Hata, *Nat. Nanotechnol.* **2011**, *6*, 296.

[36] H.-B. Yao, J. Ge, C.-F. Wang, X. Wang, W. Hu, Z.-J. Zheng, Y. Ni, S.-H. Yu, *Adv.*

Mater. **2013**, *25*, 6692.

[37] J. Chun, K. Y. Lee, C. Y. Kang, M. W. Kim, S. W. Kim, J. M. Baik, *Adv. Funct. Mater.* **2014**, *24*, 2038.

[38] W. Wu, X. Wen, Z. L. Wang, *Science (80-.).* **2013**, *340*, 952 LP.

[39] J. Chun, N.-R. Kang, J.-Y. Kim, M.-S. Noh, C.-Y. Kang, D. Choi, S.-W. Kim, Z. Lin Wang, J. Min Baik, *Nano Energy* **2015**, *11*, 1.

[40] Y. Hu, C. Xu, Y. Zhang, L. Lin, R. L. Snyder, Z. L. Wang, *Adv. Mater.* **2011**, *23*, 4068.

[41] L. Persano, C. Dagdeviren, Y. Su, Y. Zhang, S. Girardo, D. Pisignano, Y. Huang, J. a. Rogers, *Nat. Commun.* **2013**, *4*, 1633.

[42] F. Fan, L. Lin, G. Zhu, W. Wu, R. Zhang, Z. L. Wang, *Nano Lett.* **2012**, *12*, 3109.

[43] K. Y. Lee, H. J. Yoon, T. Jiang, X. Wen, W. Seung, S. W. Kim, Z. L. Wang, *Adv. Energy Mater.* **2016**, DOI 10.1002/aenm.201502566.

[44] G. Zhu, W. Q. Yang, T. Zhang, Q. Jing, J. Chen, Y. S. Zhou, *Nano Lett.* **2014**, *14*, 3208.

[45] D. Mandal, S. Yoon, K. J. Kim, *Macromol. Rapid Commun.* **2011**, *32*, 831.

[46] T. Sharma, S.-S. Je, B. Gill, J. X. J. Zhang, *Sensors Actuators A Phys.* **2012**, *177*, 87.

[47] A. Tamang, S. K. Ghosh, S. Garain, M. M. Alam, J. Haeberle, K. Henkel, D. Schmeisser, D. Mandal, *ACS Appl. Mater. Interfaces* **2015**, *7*, 16143.

[48] Y. Cho, J. B. Park, B. S. Kim, J. Lee, W. K. Hong, I. K. Park, J. E. Jang, J. I. Sohn, S. Cha, J. M. Kim, *Nano Energy* **2015**, *16*, 524.

[49] L. Lin, Y. Xie, S. Wang, W. Wu, S. Niu, X. Wen, Z. L. Wang, *ACS Nano* **2013**, *7*, 8266.

[50] M. L. Seol, S. H. Lee, J. W. Han, D. Kim, G. H. Cho, Y. K. Choi, *Nano Energy* **2015**, *17*, 63.

[51] X. Huang, D. Zhang, *Sensors Actuators A Phys.* **2014**, *216*, 176.

[52] W. Wu, X. Wen, Z. Lin Wang, *Science (80-.).* **2012**, *335*, 1215.

Chapter 6

Ionic current collector for porous P(VDF-TrFE) film

The majority of the mechanical energy harvesters are fabricated using metallic electrodes that transfer charge electronically. In this chapter, the ionic conductor is utilized as the current-collecting layers of TENG. This leads to the enhancement in the energy harvesting performance due to the formation of an electrical double layer (EDL). An autonomously self-healing TENG which can recover its performance after mechanical damage was also demonstrated.

6.1 Introduction

The emergence of next-generation electronics or bioelectronics has propelled immense enthusiasm for the development of high power density mechanical energy harvesters which can be potentially used as a sustainable power source in electronic devices such as transistors,[1,2] strain sensors,[3,4] energy storage devices,[5–7] and light-emitting diodes (LEDs).[8,9] The ability of a device to restore its functionality after mechanical damage is crucial for the realization of highly durable electronics.[10] Triboelectric energy harvesters (TEHs) have been utilized as a power source for self-powered electronics due to their high voltage output, ability to function at very low and irregular mechanical impulses, high efficiency, easy availability, environmental friendliness, and low processing costs.[11–14] Most of the TEH use metallic electrodes which transfer charge electronically.[15,16] It is hypothesized that the energy harvesting performance of the P(VDF-TrFE) mechanical energy harvester can be improved by utilizing an ionic current collector, which can improve the capacitance of the device, due to the formation of an electric double layer at the ionic current collector and P(VDF-TrFE) interface. In this work, PVA slime based ionic conductors were used a current collector in triboelectric energy harvesters (TEHs) for powering electronic devices and touch sensor applications. Moreover, the ionic conductors provide self-healing ability to the TEH device.

6.2 Results and discussion

6.2.1 Characterization of the ionic conductor

Figure 6.1a shows the schematic of the fabricated TEH with ionic current collector, which consists of a self-poled porous P(VDF-TrFE) film layer with a thickness of 200 ± 10 μm, utilized as the triboelectrically positive material, a slime layer (a cross-linked poly(vinyl alcohol) (PVA) gel) with a thickness of 1 mm, as the ionic current collector, and VHB tape with a thickness of 1 mm as a substrate. The detailed fabrication method is described in the Experimental sections 3.3. In the previous chapter, it was shown that the porous self-poled P(VDF-TrFE) film is a good triboelectrically positive material due to combined effect of

triboelectric surface charge and piezoelectric polarization. PDMS is chosen as a triboelectric negative material, due to higher electronegativity.

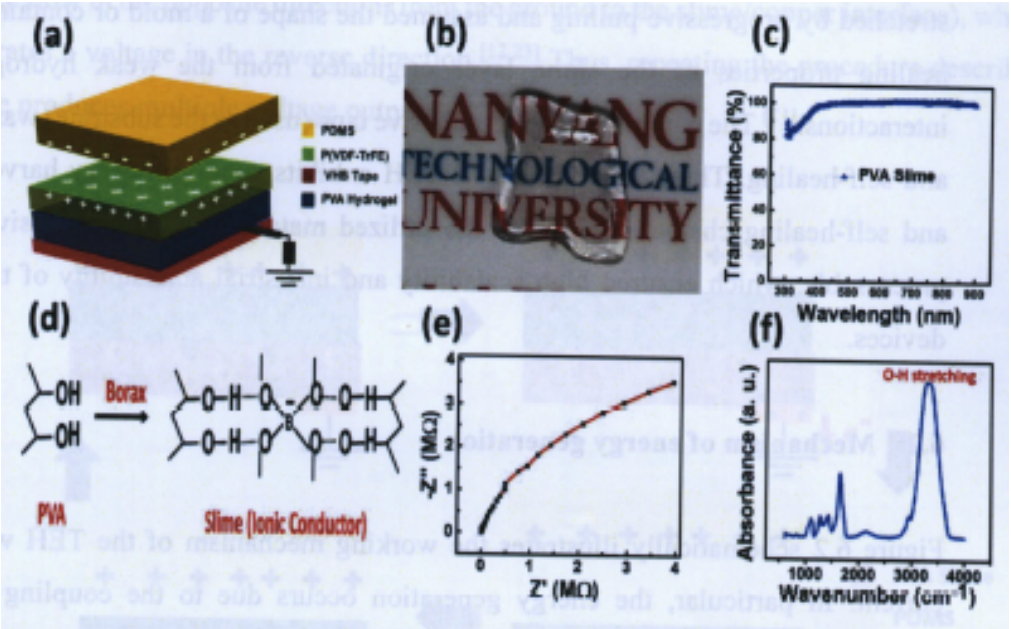

Figure 6.1. (a) Schematic diagram of the IS-TEH. (b) Digital photo of the highly transparent IS-TEH. (b) Digital photo of the ionic conductor showing high transparency. (c) Transmittance spectra of the PVA slime (ionic conductor) with respect to a glass slide. (d) Illustration of reaction between PVA and borate ions leads to the formation of slime (a borate cross-linked poly(vinyl alcohol)). (e) Electrochemical impedance spectroscopy measurement of the slime (ionic conductor). (f) FTIR spectra of the PVA slime (ionic conductor).

Figure 6.1b shows the digital photograph of the highly transparent PVA slime layer (100% transmittance for visible light, Figure 6.1c), which was formed due to the weak hydrogen bonding interactions between the tetrafunctional borate ions with the –OH group of PVA, as illustrated in Figure 6.1d. The presence of the hydrogen bonding is verified from the Fourier transform infrared spectroscopy (FTIR) (Figure 6.1f). The subsequent cross-linking led to the formation of a three-dimensional (3D) polymer network.[17] The produced slime exhibited high ionic conductivity (2.9×10^{-5} Scm^{-1}) due to the presence of positive (Na^{+}) and negative ions ($B(OH)_4^{-}$), which was measured using electrochemical impedance spectroscopy (EIS) (Figure 6.1e). The 3D PVA network provided the necessary path for ion transport (it was selected as the polymer matrix due to its non-toxicity, biocompatibility,

high transparency, and high ionic conductivity).[18] The produced weak bonds led to the formation of a viscoelastic non-Newtonian fluid;[19] as a result, the slime layer could be stretched by progressive pulling and assumed the shape of a mold or container. The self-healing properties of the slime layer originated from the weak hydrogen bonding interactions.[17] The commercial VHB adhesive tape (used as the substrate) was transparent, and self-healing. Thus, the resulting IS-TEH exhibits superior energy harvesting ability and self-healing characteristics. All the utilized materials were inexpensive and easily processable, which ensured high scalability and industrial adaptability of the fabricated devices.

6.2.1 Mechanism of energy generation

Figure 6.2 schematically illustrates the working mechanism of the TEH with the ionic current. In particular, the energy generation occurs due to the coupling between the triboelectric and electrostatic induction effects.[11,20,21] According to the triboelectric series, self-poled porous P(VDF-TrFE) foam can be considered an excellent triboelectrically positive material (due to its relatively low electronegativity), and PDMS represents an excellent triboelectrically negative material (due to its relatively high electronegativity).[21] Initially, the surfaces of porous P(VDF-TrFE) foam and PDMS were not in contact and therefore generated no surface charges; as a result, the positive (Na^+) and negative ($B(OH)_4^-$) ions of the ionic conductor remains randomly distributed across the PVA matrix. When the PDMS comes in contact with the P(VDF-TrFE), charge transfer from the P(VDF-TrFE) to the PDMS (due to the difference in their electronegativities), making the PDMS negatively charged, and the P(VDF-TrFE) positively charged.[21] When the PDMS is removed, the two oppositely charged surfaces (PDMS and P(VDF-TrFE)) become separated in space, thus creating a potential difference. The unscreened negative charge on the surface of P(VDF-TrFE) induces the accumulation of positive ions (Na^+) at the P(VDF-TrFE)/slime interface and negative ions ($B(OH)_4^-$) at the slime/copper interface, which in turn leads to electrical double layer formation.[22] This leads to a transient charge flow from the copper electrode to the ground, generating a voltage output. An electrostatic equilibrium is achieved when the two oppositely charged surfaces reach the maximum

separation distance. When the mechanical force is applied again, the distance between the PDMS and the P(VDF-TrFE) as well as their potential difference decrease, resulting in a charge flow in the opposite direction (from the ground to the slime/copper interface), which generates a voltage in the reverse direction.[12,23] Thus, repeating the procedure described above produces multiple voltage outputs.

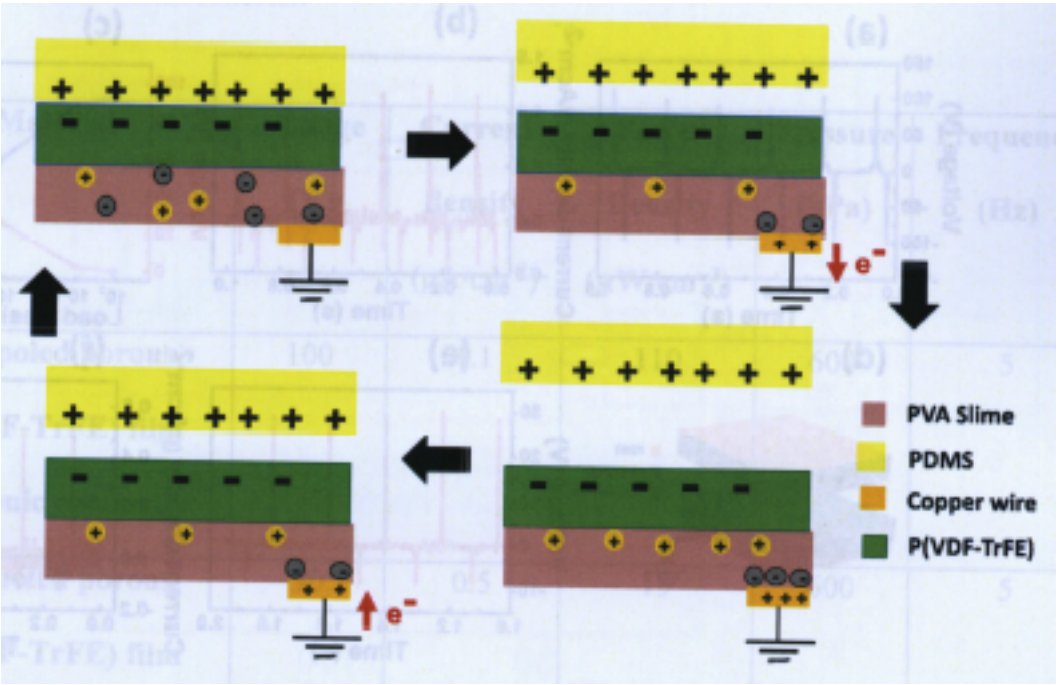

Figure 6.2. Schematic diagram of the working mechanism of TEH with the ionic conductor.

6.2.2 Energy harvesting performance of the porous P(VDF-TrFE) with ionic current collector

The energy harvesting performance of the TEH with an ionic current collector (represented by the open-circuit voltage (V_{oc}), and short-circuit current density (I_{sc}) was evaluated by applying a compressive mechanical pressure of 600 kPa at a frequency of 5 Hz. The IS-TEH generated the approximate V_{oc} of 100 V (Figure 6.3a), and I_{sc} of 1.1 $\mu A \cdot cm^{-2}$ (Figure 6.3b). During practical application, the IS-TEH will be utilized to power load with different resistance. The impedance of the load affects the performance of the energy harvesting device. Hence, energy harvesting performance of the TEH was evaluated across various load resistance. Figure 6.3c shows the variations of the voltage output and current density

of the fabricated IS-TEH with different load resistance. Due to Ohm's law, the output voltage increases and the output current decreases with an increase in the load resistance. A power density (defined by the formula P = V·I, where P is the power density, V is the output voltage of the device, and I is the output current of the device) of 110 $\mu W \cdot cm^{-2}$ was obtained from the device.

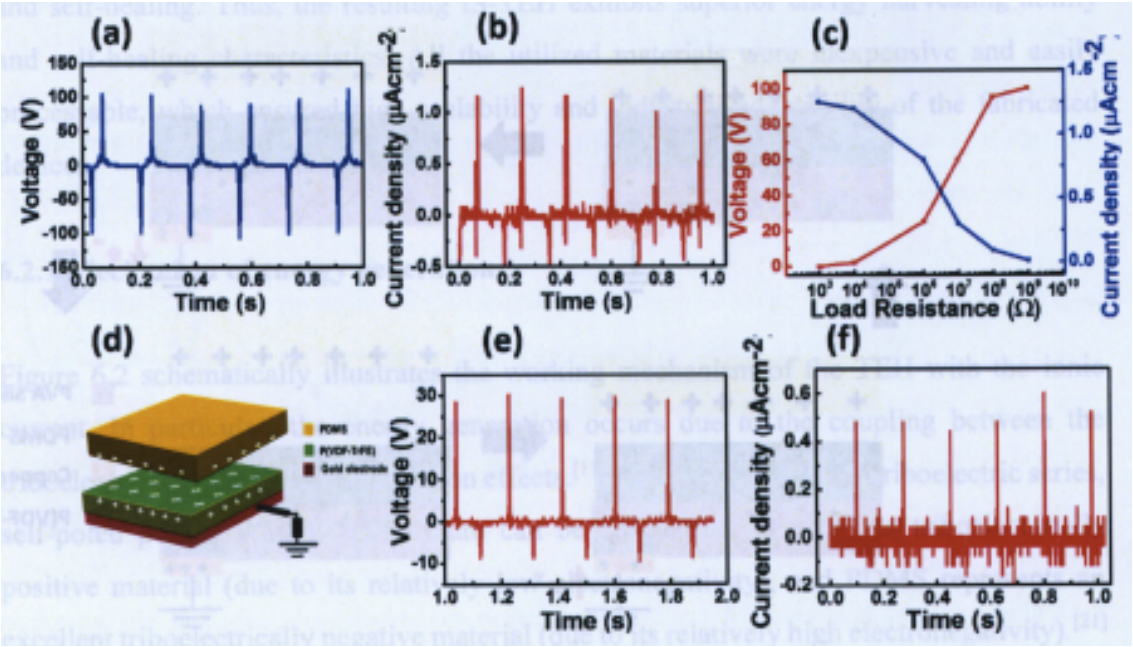

Figure 6.3. The energy harvesting performance of the IS-TEH when subjected to a mechanical pressure of 600 kPa at a frequency of 5 Hz. (a) Voltage output (V_{oc}) (b) Current density (I_s). (c) Variation of voltage and current as a function of load resistance of the IS-TEH. (d) Schematic diagram of the TEH without the ionic current collector. The energy harvesting performance of the TEH without ionic current collector when subjected to a mechanical pressure of 600 kPa at a frequency of 5 Hz. (e) Voltage output (V_{oc}) (f) Current density (I_s).

For comparison purposes, the energy harvesting performance of the control sample (a TEH utilizing a silver electrode as the current collector) was evaluated as well (Figure 6.3d, shows the schematic of the control sample). It consisted of self-poled porous P(VDF-TrFE) foam layer with a thickness of 200 ± 20 μm and area of 2 × 2 cm^2 and the gold sputtered with an area of 1 × 1 cm^2, and a sheet resistance of 4 Ωcm^{-1}. The control sample generated approximate V_{oc} of 30 V (Figure 6.3e), and I_{sc} of 0.5 $\mu A \cdot cm^{-2}$ (Figure 6.3f) at similar

pressure and frequency. The power density was calculated to be 18 $\mu W \cdot cm^{-2}$. Thus, the IS-TEH with an ionic current collector exhibited a 5-fold enhancement in the power density as compared to that generated by the control sample (Table 6.1).

Table 6.1: Summary of the energy harvesting performance of the porous P(VDF-TrFE) TEH with and without ionic current collector.

Material	**Voltage (V)**	**Current density ($\mu A \cdot cm^{-2}$)**	**Power Density ($\mu W \cdot cm^{-2}$)**	**Pressure (kPa)**	**Frequency (Hz)**
Self-poled porous P(VDF-TrFE) film with ionic conductor	100	1.1	110	600	5
Self-poled porous P(VDF-TrFE) film without ionic conductor	30	0.5	15	600	5

The observed enhancement in the energy harvesting performance for the TEH with an ionic conductor can be attributed to the EDL formation. The magnitude of V_{oc} of the IS-TEH depends on the triboelectric charge density on the P(VDF-TrFE) film surface, which in turn depends on the device capacitance.[24,25] Thus, a higher capacitance leads to a higher output voltage. During voltage generation, the positive and negative ions of the slime formed an EDL at the slime/ P(VDF-TrFE) and slime/copper interfaces, respectively. The EDL charge separation distance is infinitesimally small (in few nanometers), which significantly increases the capacitance of the device with an ionic conductor (Figure 6.4; shows the capacitance of the slime and the silicone rubber as a function of frequency). As a result, the

output performance of the fabricated IS-TEH (which is directly related to the device capacitance) increases, indicating that the use of the slime-based ionic conductor as a current collector can significantly improve its energy harvesting performance. Ionic conductors have been used in electronic devices such as actuators,[26,27] electroluminescent (EL) devices,[28–30] and touch sensors.[31–33] This work is similar to our recently reported work on use of ionic conductor for silicone rubber based triboelectric energy harvesters.[34]

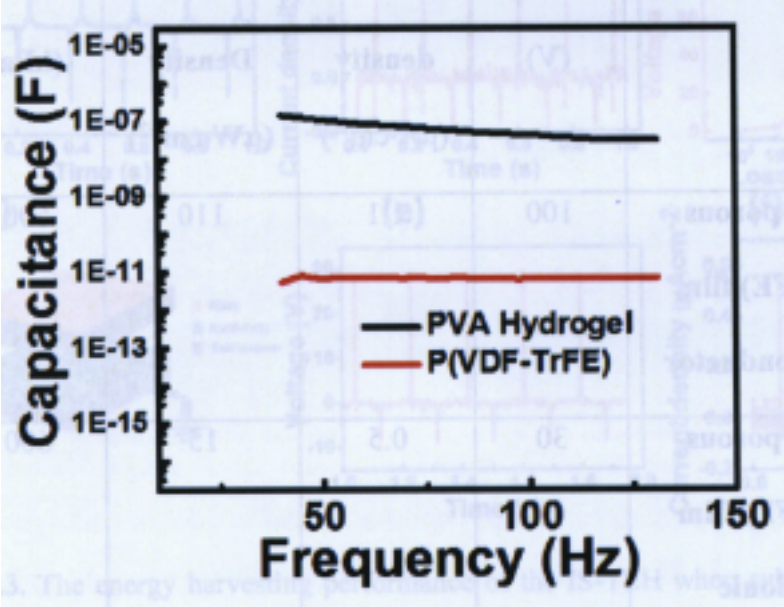

Figure 6.4. Capacitance of the PVA slime and P(VDF-TrFE) as a function of frequency.

6.3 Self-healing energy harvester

During real-time operation, the energy harvester can undergo mechanical damage due to deformation, wear and tear, and accident inflicts. Hence, the realization of a robust and sustainable self-healing energy harvester includes the ability to restore its performance after extreme mechanical damage. Thus, the performance of the fabricated IS-TEH was measured after subjecting the device to extreme mechanical damage, such as complete bifurcation of the device. After the fabricated TEH was completely bifurcated through the slime, it managed to completely heal itself without applying any external stimuli. Energy harvesting performance of the bifurcated devices (corresponding to the voltage output of

around 100 V generated upon application of an approximate mechanical pressure of 600 kPa at 5 Hz frequency) was monitored before and after self-healing (Figure 6.5a). This ability of the IS-TEH to generate superior energy harvesting performance, while being autonomously self-healing makes it an ideal power source for the realization of self-powered electronics and a touch sensor.

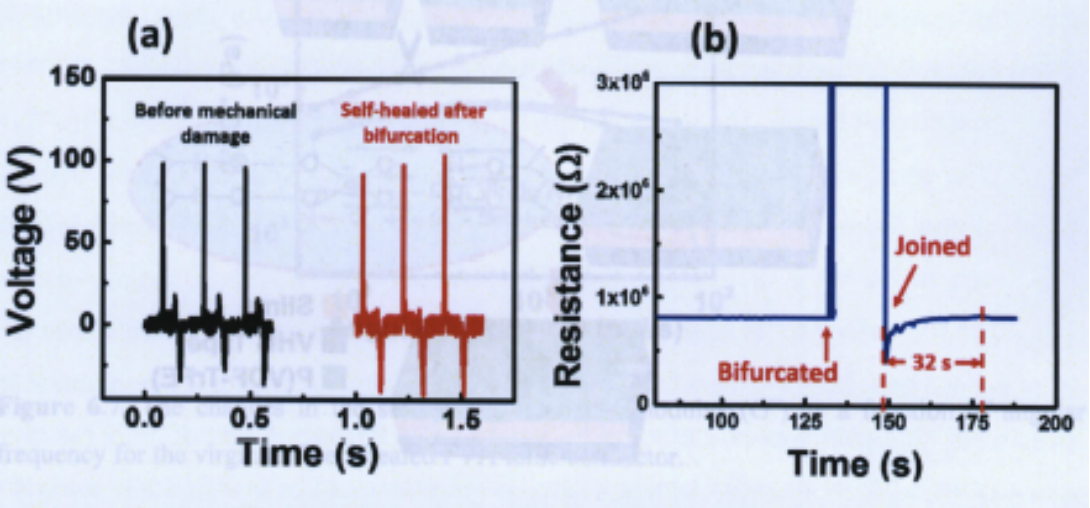

Figure 6.5. (a) The voltage output of the IS-TEH before mechanical damage and self-healed device. (b) The change in the resistance of the slime during bifurcation and self-healing.

During the self-healing process, the device restores both its mechanical and electrical properties; thus, the ionic conductor recovers its original ionic conductivity within the first 32 s with an efficiency of 99% (Figure 6.5b). Slime possesses self-healing property due to the weak hydrogen bonding interactions between its tetrafunctional borate ions and –OH groups, which are schematically illustrated in Figure 6.6. The cross-linked polymer network remains in a state of dynamic equilibrium, where weak bonds can be easily disrupted and restored at room temperature without application of any external stimuli. The IS-TEH reported in this work consisted of a PVA slime sandwiched between the P(VDF-TrFE) and VHB tape. The observed self-healing process of the TEH can be attributed to the presence of both the slime-based current collector and VHB tape. The PVA slime, used as the current collector is self-healing, and the commercial VHB tape used as the substrate and cavity to hold the slime is also self-healing. The P(VDF-TrFE) used as the triboelectric material is not self-healing. However, for the realization of a self-healing triboelectric

energy harvester, it is not critical for the P(VDF-TrFE) to be self-healing. Even with the damaged P(VDF-TrFE), the energy harvesting performance of the device remains almost the same (Figure 6.5).

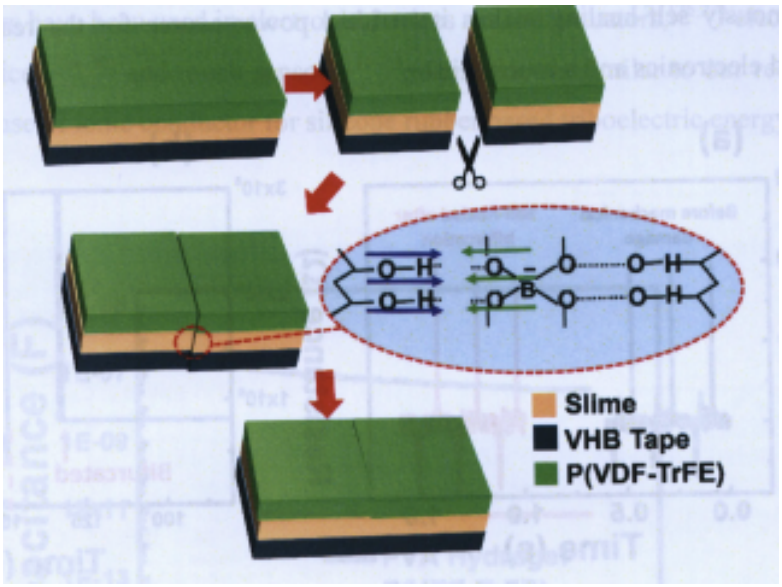

Figure 6.6. Schematic representation of the self-healing process of the IS-TEH.

6.3.1 Mechanical properties of the self-healing ionic current collector

Detailed mechanical properties (including mechanical properties before and after healing, healing time, the effect of healing temperature) of the self-healing current collector was studied. The mechanical properties such as tensile stress-strain behavior and rheological analysis were measured before and after self-healing the ionic conductor.

6.3.1.1 Rheological Analysis

Rheological properties were studied before and after healing the ionic conductor. Figure 6.7 shows the storage (elastic) (G') and loss (viscous) (G") modulus as a function of angular frequency. The storage and loss modulus of the virgin PVA slime at an angular frequency of 10 rad/s are 21.7 and 7.88 kPa respectively. For the self-healed sample, the storage and loss modulus at an angular frequency of 10 rad/s is 21.3 and 7.34 kPa respectively. The storage and loss modulus remained almost the same over the entire frequency range, before

and after self-healing, thus indicating the effective self-healing behavior of the PVA slime. This shows that the inner structures of the PVA slime are completely healed. The detailed method of characterization is provided in the experimental section 3.1.

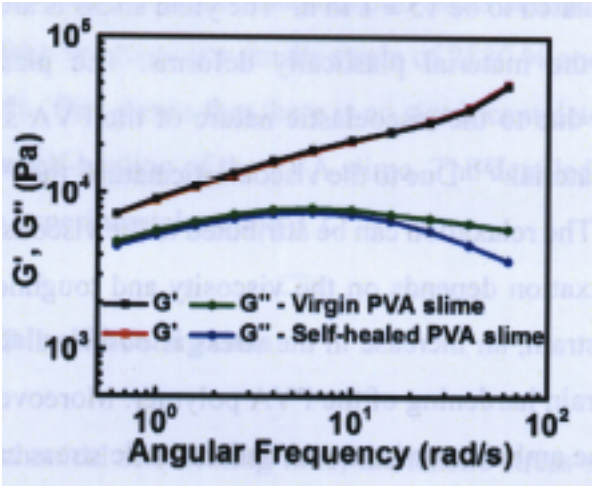

Figure 6.7. The changes in the storage (G') and loss modulus (G'') as a function of angular frequency for the virgin and self-healed PVA ionic conductor.

6.3.1.2 Tensile stress-strain behavior

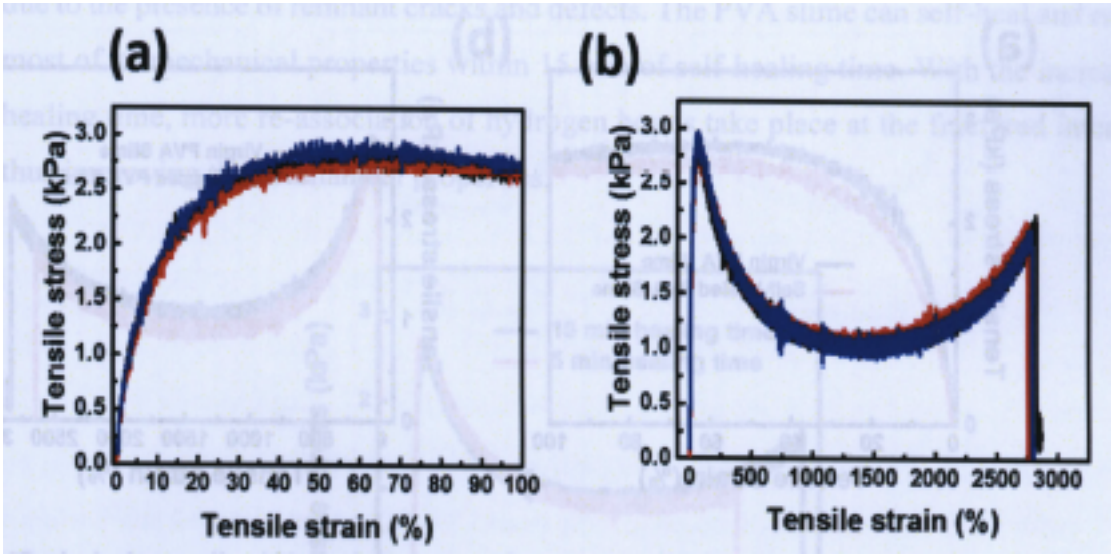

Figure 6.8. (a) and (b) The tensile stress-strain curve of 3 virgin PVA slime samples.

First, the tensile stress-strain behavior of the virgin PVA ionic conductor was measured for 3 samples, with similar dimensions. From the Figure 6.8a, it can seen that the PVA slime shows elastic behavior until 20 % tensile strain. The Young's modulus (measured within 10 % strain) is calculated to be 15 ± 1 kPa. The yield stress is around 2.8 ± 0.1 kPa. Upon further stretching, the material plastically deforms. The plastic region shows stress relaxation behavior due to the viscoelastic nature of the PVA slime, which is similar to other viscoelastic material.[35] Due to the viscoelastic nature, the PVA slime has both elastic and viscous nature. The relaxation can be attributed to the viscous nature of the PVA slime. The amount of relaxation depends on the viscosity and toughness of the material. With further increase in strain, an increase in the stress is observed. This increase in the stress can be due to the strain hardening of the PVA polymer. Moreover, prolonged exposure of the PVA slime to the ambient environment under tensile stress can accelerate evaporation of water. This can cause the hardening of PVA slime, resulting in the increase in stress. Further increase in the strain, leads to mechanical fracture. A loss of 20 % in weight of the sample before and after tensile testing upon fracture can be found; it was likely due to the accelerated loss of water during the tensile strained process. The tensile stress-strain behavior of the PVA slime was measured before and after self-healing (Figure 6.9).

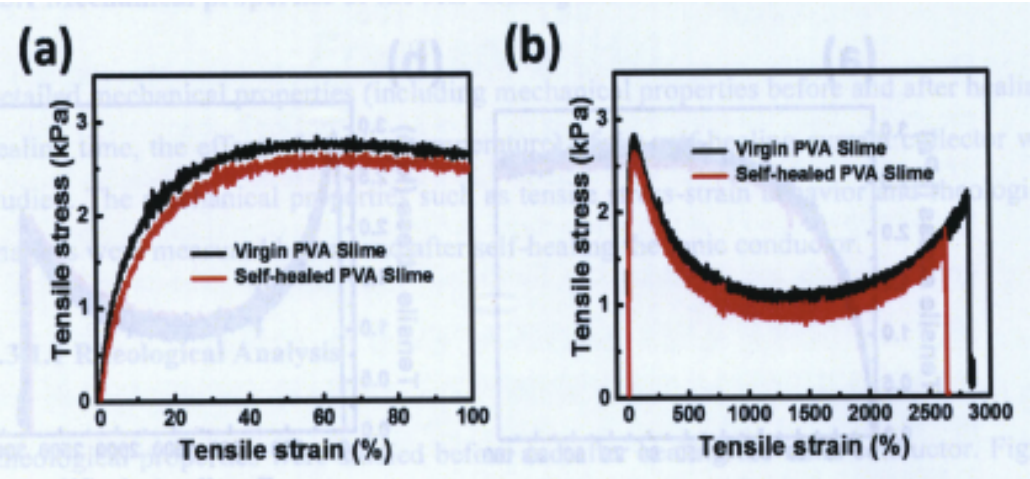

Figure 6.9. (a) and (b) The tensile stress-strain curve of the self-healing and virgin PVA ionic conductor.

The self-healed and virgin sample shows similar stress-strain behavior. For the self-healed sample, the Young's modulus (measured within 10 % strain) is calculated to be around 14 kPa and the yield stress around 2.6 kPa. This shows that the self-healed material recovers the mechanical performance in the elastic region (after self-healing). In the plastic region, the virgin PVA slime fractures at a tensile strain of 2830 % and the self-healed PVA slime fractures at 2630 %. This shows that there is no significant deterioration in the mechanical performance after self-healing of the PVA slime. The detailed method of characterization is provided in the experimental section 3.1.

6.3.1.3 Mechanical self-healing time

To obtain the mechanical self-healing time, the tensile stress-strain test was performed at different healing time. If the material is not completely healed, cracks will initiate at the mended joint, and the material will fracture. Figure 6.10 shows that the tensile stress-strain behavior of the PVA slime with 5 and 15 min healing time. Both the virgin and self-healed sample showed similar behavior in the elastic region. 5 min healing time was not sufficient, as the PVA slime fractured at a reduced strain compared to the virgin sample. This can be due to the presence of remnant cracks and defects. The PVA slime can self-heal and restore most of its mechanical properties within 15 min of self-healing time. With the increase in healing time, more re-association of hydrogen bonds take place at the fractured interface, thus improving the mechanical properties.

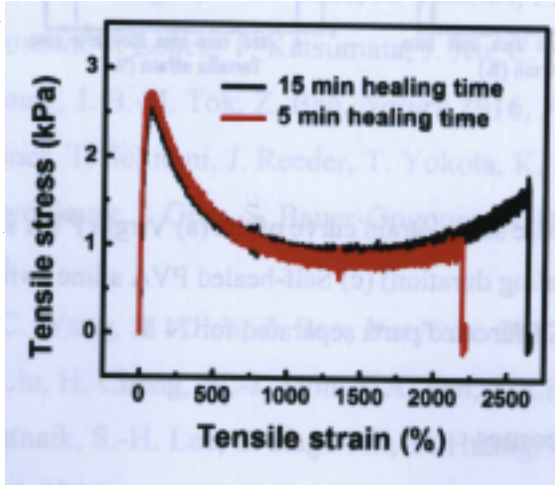

Figure 6.10. The tensile stress-strain curve of the self-healing PVA slime with different healing times.

6.3.1.4 Mechanical healing efficiency

Mechanical healing efficiency is defined as the amount of toughness restored after healing relative to the toughness before mechanical damage.[3] The mechanical healing efficiency of the slime (with 15 min self-healing duration) is 81 % (calculated from Figure 6.11a and b). However, the mechanical healing efficiency decreases to 25 % (calculated from Figure 6.11a and c) for the slime (with 15 min self-healing duration) healed after keeping the bifurcated parts separated for 24 h. The decrease in the efficiency can be attributed to the loss of hydrogen bonding, likely due to the partial loss of water from the slime that reduces its ability to endure large tensile strain. The hardening of PVA slime due to the loss of water could be the reason for the increase in the yield stress (Figure 6.11c).

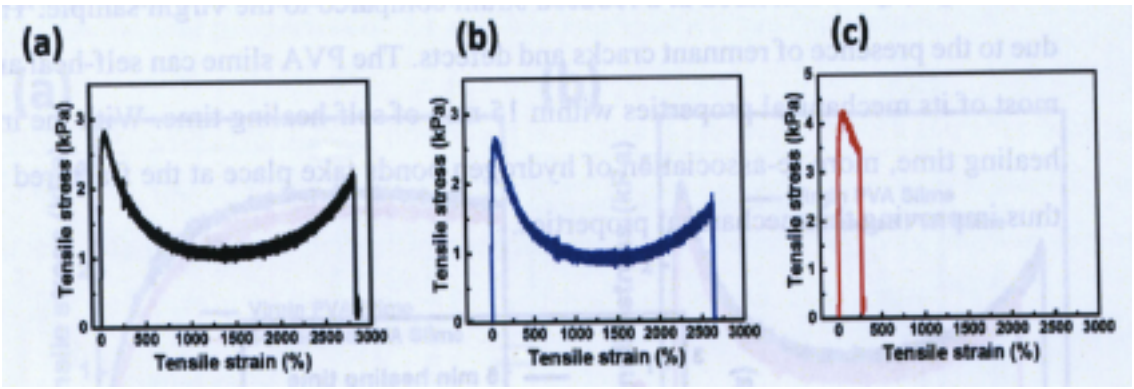

Figure 6.11. The tensile stress-strain curve of the (a) Virgin PVA slime (b) Self-healed PVA slime (with 15 min self-healing duration) (c) Self-healed PVA slime (with 15 min self-healing duration) after the keeping the bifurcated parts separated for 24 h.

6.3 Principal Outcomes

- Successfully demonstrated an effective way to enhance the energy harvesting performance of the P(VDF-TrFE) based mechanical energy harvester by utilizing an ionic current collector.
- Demonstrated a self-healing mechanical energy harvester.

6.2.3 Chapter Summary

In conclusion, a disruptive technology of using ionic current collectors in P(VDF-TrFE) triboelectric energy harvester is demonstrated, which enhances its energy harvesting performance due to the increment in the capacitance of the device, thus proving our hypothesis. The higher capacitance is due to the formation of an electrical double layer. The fabricated device demonstrated self-healing properties and was able to recover its energy harvesting performance after complete bifurcation. Owing to the higher energy generation and autonomously self-heal at room temperature, the fabricated TEH takes a quantum leap in the domain of mechanical energy harvesters. Hence, the innovative scientific concept and disruptive technology demonstrated in this work open up new possibilities for the utilization of TEHs for a broad spectrum of application including health monitoring, sports, wearable and implantable electronics, and smart robotics, enabling a huge step towards the realization of next-generation electronics.

Reference

[1] J. Y. Oh, S. Rondeau-Gagné, Y.-C. Chiu, A. Chortos, F. Lissel, G.-J. N. Wang, B. C. Schroeder, T. Kurosawa, J. Lopez, T. Katsumata, J. Xu, C. Zhu, X. Gu, W.-G. Bae, Y. Kim, L. Jin, J. W. Chung, J. B.-H. Tok, Z. Bao, *Nature* **2016**, *539*, 411.

[2] M. Kaltenbrunner, T. Sekitani, J. Reeder, T. Yokota, K. Kuribara, T. Tokuhara, M. Drack, R. Schwodiauer, I. Graz, S. Bauer-Gogonea, S. Bauer, T. Someya, *Nature* **2013**, *499*, 458.

[3] B. C.-K. Tee, C. Wang, R. Allen, Z. Bao, *Nat Nano* **2012**, *7*, 825.

[4] X. Huang, Y. Liu, H. Cheng, W.-J. Shin, J. A. Fan, Z. Liu, C.-J. Lu, G.-W. Kong, K. Chen, D. Patnaik, S.-H. Lee, S. Hage-Ali, Y. Huang, J. A. Rogers, *Adv. Funct. Mater.* **2014**, *24*, 3846.

[5] S. Xu, Y. Zhang, J. Cho, J. Lee, X. Huang, L. Jia, J. A. Fan, Y. Su, J. Su, H. Zhang, H. Cheng, B. Lu, C. Yu, C. Chuang, T. Kim, T. Song, K. Shigeta, S. Kang, C. Dagdeviren, I. Petrov, P. V Braun, Y. Huang, U. Paik, J. A. Rogers, *Nat. Commun.* **2013**, *4*, 1543.

[6] Y. Huang, M. Zhong, Y. Huang, M. Zhu, Z. Pei, Z. Wang, Q. Xue, X. Xie, C. Zhi, *Nat. Commun.* **2015**, *6*, 10310.

[7] K. Parida, V. Bhavanasi, V. Kumar, J. Wang, P. S. Lee, *J. Power Sources* **2017**, *342*, 70.

[8] T. Someya, *Nat Mater* **2010**, *9*, 879.

[9] J. Liang, L. Li, X. Niu, Z. Yu, Q. Pei, *Nat Phot.* **2013**, *7*, 817.

[10] A. Chortos, J. Liu, Z. Bao, *Nat Mater* **2016**, *15*, 937.

[11] Z. L. Wang, J. Chen, L. Lin, *Energy Environ. Sci.* **2015**, *8*, 2250.

[12] S. Wang, L. Lin, Z. L. Wang, *Nano Energy* **2015**, *11*, 436.

[13] J. Chun, B. U. Ye, J. W. Lee, D. Choi, C.-Y. Kang, S.-W. Kim, Z. L. Wang, J. M. Baik, *Nat. Commun.* **2016**, *7*, 12985.

[14] J. Bae, J. Lee, S. Kim, J. Ha, B.-S. Lee, Y. Park, C. Choong, J.-B. Kim, Z. L. Wang, H.-Y. Kim, J.-J. Park, U.-I. Chung, *Nat. Commun.* **2014**, *5*, 4929.

[15] J. Wang, S. Li, F. Yi, Y. Zi, J. Lin, X. Wang, Y. Xu, Z. L. Wang, *Nat. Commun.* **2016**, *7*, 12744.

[16] K. N. Kim, J. Chun, J. W. Kim, K. Y. Lee, J.-U. Park, S.-W. Kim, Z. L. Wang, J. M. Baik, *ACS Nano* **2015**, *9*, 6394.

[17] E. Z. Casassa, A. M. Sarquis, C. H. Van Dyke, *J. Chem. Educ.* **1986**, *63*, 57.

[18] A. A. Mohamad, N. S. Mohamed, M. Z. A. Yahya, R. Othman, S. Ramesh, Y. Alias, A. K. Arof, *Solid State Ionics* **2003**, *156*, 171.

[19] V. de Zea Bermudez, P. P. de Almeida, J. F. Seita, *J. Chem. Educ.* **1998**, *75*, 1410.

[20] Z. L. Wang, *Faraday Discuss.* **2014**, *176*, 447.

[21] Y.-C. Lai, J. Deng, S. Niu, W. Peng, C. Wu, R. Liu, Z. Wen, Z. L. Wang, *Adv. Mater.* **2016**, *28*, 10024.

[22] B. U. Ye, B.-J. Kim, J. Ryu, J. Y. Lee, J. M. Baik, K. Hong, *Nanoscale* **2015**, *7*, 16189.

[23] J. Chun, J. W. Kim, W. Jung, C.-Y. Kang, S.-W. Kim, Z. L. Wang, J. M. Baik,

Energy Environ. Sci. **2015**, *8*, 3006.

[24] W. Seung, H.-J. Yoon, T. Y. Kim, H. Ryu, J. Kim, J.-H. Lee, J. H. Lee, S. Kim, Y. K. Park, Y. J. Park, S.-W. Kim, *Adv. Energy Mater.* **2017**, *7*, 1600988.

[25] J. Chen, H. Guo, X. He, G. Liu, Y. Xi, H. Shi, C. Hu, *ACS Appl. Mater. Interfaces* **2016**, *8*, 736.

[26] C. Keplinger, J.-Y. Sun, C. C. Foo, P. Rothemund, G. M. Whitesides, Z. Suo, *Science (80-.).* **2013**, *341*, 984.

[27] Y. Cao, T. G. Morrissey, E. Acome, S. I. Allec, B. M. Wong, C. Keplinger, C. Wang, *Adv. Mater.* **2017**, *29*, 1605099.

[28] C. H. Yang, B. Chen, J. Zhou, Y. M. Chen, Z. Suo, *Adv. Mater.* **2016**, *28*, 4480.

[29] J. Wang, C. Yan, G. Cai, M. Cui, A. Lee-Sie Eh, P. See Lee, *Adv. Mater.* **2016**, *28*, 4490.

[30] C. Larson, B. Peele, S. Li, S. Robinson, M. Totaro, L. Beccai, B. Mazzolai, R. Shepherd, *Science (80-.).* **2016**, *351*, 1071.

[31] K. Tian, J. Bae, S. E. Bakarich, C. Yang, R. D. Gately, G. M. Spinks, M. in het Panhuis, Z. Suo, J. J. Vlassak, *Adv. Mater.* **2017**, *29*, 1604827.

[32] J.-Y. Sun, C. Keplinger, G. M. Whitesides, Z. Suo, *Adv. Mater.* **2014**, *26*, 7608.

[33] C.-C. Kim, H.-H. Lee, K. H. Oh, J.-Y. Sun, *Science (80-.).* **2016**, *353*, 682.

[34] K. Parida, V. Kumar, W. Jiangxin, V. Bhavanasi, R. Bendi, P. S. Lee, *Adv. Mater.* **n.d.**, 1702181.

[35] C. S. Boland, U. Khan, G. Ryan, S. Barwich, R. Charifou, A. Harvey, C. Backes, Z. Li, M. S. Ferreira, M. E. Möbius, R. J. Young, J. N. Coleman, *Science (80-.).* **2016**, *354*, 1257.

Chapter 7

Conclusions and recommendations

In this chapter, the work done in this dissertation is summarized. The three hypotheses (modifying the structural, surface charge and charge storage properties of the P(VDF-TrFE)) proposed in this work to improve the mechanical energy harvesting performance of P(VDF-TrFE) were discussed. Work done to validate the hypothesis are explained. The extent to which the hypotheses are proven are discussed in detail. The significance and the use of the work is explained in detail. Future recommendations to further improve the energy harvesting performance are provided.

7.1 Conclusions

The main objective of this dissertation is the improve the energy harvesting performance of the P(VDF-TrFE) based mechanical energy harvester for self-powered device application. To achieve the objective, it was hypothesized that by tuning the structural, and surface charge properties of the P(VDF-TrFE), the mechanical energy harvesting performance can be improved. In the first chapter, porous P(VDF-TrFE) films (with higher strain and lower dielectric constant) was created to enhance the energy harvesting performance of the P(VDF-TrFE) mechanical energy harvester. To validate our hypothesis, a porous P(VDF-TrFE) film using VIPS method was fabricated. The porous structure makes the film more compressible compared to that of the compact P(VDF-TrFE) film. Compressibility is directly related to the piezoelectric coefficient of the material, thus with the increase in the compressibility, the energy harvesting performance increases. The porous structure lowers the dielectric constant, thus creating a higher internal piezoelectric potential. Thus, the energy harvesting performance of the P(VDF-TrFE) mechanical energy harvester was improved due to the porous structural modification, thus proving our hypothesis. Additionally, the porous P(VDF-TrFE) film was used as the separator in the self-charged supercapacitor to realize a fast charging self-charged supercapacitor. In the second chapter, it was hypothesized that the energy harvesting performance of the P(VDF-TrFE) can be increased by utilizing the combined effect of triboelectric surface charge and polarization induced surface charge. To validate our hypothesis, a novel method was developed to fabricate a self-poled porous P(VDF-TrFE) film which eliminates the tedious piezoelectric polymer preparatory steps like annealing and poling. Detailed study was done to understand the mechanism of self-poling. The self-poled porous P(VDF-TrFE) film was used to fabricate a triboelectric energy harvester which enhanced the energy harvesting performance due to the combined effect of piezoelectric polarization and triboelectric surface charges, thus validating our hypothesis. By utilizing the combined effect of piezoelectric polarization and triboelectric surface charge, the saturation pressure of the triboelectric energy harvester can be increased, thus making it capable of detecting a wide range of pressure with high sensitivity. Herein, the self-polarized porous P(VDF-TrFE) TEH was used as a self-powered pressure sensor, which was able to measure a wide range pressure, thus validating our hypothesis. The possibility to detect wide-range of pressure with high sensitivity extends the realms of application of triboelectric energy harvester

for the self-powered application. Taking into account both the wide pressure sensing range and the sensitivity, the self-polarized P(VDF-TrFE) pressure sensor shows the best performance amongst all the self-powered pressure sensors reported so far. In the third chapter, it was hypothesized that the energy harvesting performance of the P(VDF-TrFE) mechanical energy harvester can be improved by utilizing an ionic current collector, which will improve the capacitance of the device, due to the formation of an electric double layer at the ionic current collector and P(VDF-TrFE) interface. To prove the hypothesis, a PVA slime based ionic conductor was prepared and was used as the current collector in triboelectric energy harvesters. The PVA slime ionic current collector leads to the formation of an electrical double layer, which increases the capacitance of the device, thus enhancing the device performance, thus validating our hypothesis. Detailed electrical and mechanical self-healing properties were analyzed. Moreover, a self-healing mechanical energy harvester was demonstrated which can recover its energy harvesting performance after complete bifurcation. Owing to the higher energy generation and autonomously self-heal properties the mechanical energy harvester can be used in a broad spectrum of application to realize self-powered devices. To summarize and evaluate, all the energy harvesting performance of all the work done in this thesis are shown in table 7.1. The power density is calculated by the formula $P = V \cdot I$, where P is the power density, V is the output voltage of the device, and I is the short circuit current of the device.

Table 7.1: Summary of the energy harvesting performance of all the work done in this dissertation.

Material and Device	Pressure (kPa)	Frequency (Hz)	Open Circuit Voltage (Voc)	Short Circuit Current density (Isc) (μAcm^{-2})	Power Density (μWcm^{-2})
Compact P(VDF-TrFE) piezoelectric device	600	5	1.8	0.08	0.18
Porous P(VDF-TrFE) piezoelectric device	600	5	6	0.6	3.6
Non-poled porous P(VDF-TrFE) Triboelectric device	600	5	5	0.2	1

Self-poled porous P(VDF-TrFE) Triboelectric device	600	5	30	0.5	15
Self-poled porous P(VDF-TrFE) film with ionic conductor Triboelectric device	600	5	100	1.1	110

7.2 Future work

- **Electrospun nanofiber of PVDF-TrFE and BTO composite for energy harvesting**

Inorganic piezoelectric material such as BTO, ZnO, or PZT have higher piezoelectric coefficient compared to that of the organic counterparts.[1,2] From the previous literature, it is known that the composite of inorganic and polymer piezoelectric materials can improve the energy harvesting performance of piezoelectric energy harvester.[3–5] To achieve this, the future plan is to fabricate ultra-fine electrospun nanofiber of P(VDF-TrFE) and BTO composite for triboelectric nanogenerator application. The use of P(VDF-TrFE) and BTO will increase the internal piezoelectric potential, thus improving the total surface charge, which can improve the energy harvesting performance. The use of electrospun nanofiber will improve the total surface area of the P(VDF-TrFE) film, thus increasing the surface charge.[6] This can improve the energy harvesting performance of the P(VDF-TrFE) mechanical energy harvester.

- **Incorporation of ionic material into porous PVDF-TrFE foam**

In chapter 7, it is shown that the use of ionic current collector can improve the energy harvesting performance of the device due to the formation of an electrical double layer at the ionic conductor and copper contact (metallic collector) interface. The performance of the device can be significantly improved by increasing the contact area of the ionic material and copper collector. With the increase in the area of contact, more number of ions will accumulate, further improving the capacitance of the device. To achieve this, the future plan is to incorporate the ionic material into the porous P(VDF-TrFE) film and use metallic current collector in the triboelectric energy harvester. This

will further increase the contact area between the ionic material and the current collector, which can further improve the energy harvesting performance.

- **Lumped model of the porous piezoelectric and triboelectric work**

The first-order lumped-parameter equivalent circuit model of the triboelectric nanogenerator is described in section 2.1.3. The triboelectric device consist of a voltage source in series with a capacitor as shown in Figure 2.5. This model can be improved by considering other parameters affecting the energy harvesting performance of the triboelectric device reported in this thesis. Porosity, polarization induced surface charge, humidity etc factors will be considered to relate the obtained results with the theoretical understanding.

Reference

[1] R. C. W. Tsang, K. W. Kwok, H. L. W. Chan, C. L. Choy, *Integr. Ferroelectr.* **2002**, *50*, 143.

[2] D. Berlincourt, H. Jaffe, *Phys. Rev.* **1958**, *111*, 143.

[3] K.-I. Park, C. K. Jeong, N. K. Kim, K. J. Lee, *Nano Converg.* **2016**, *3*, 12.

[4] X. Cui, X. Ni, Y. Zhang, *J. Alloys Compd.* **2016**, *675*, 306.

[5] R. Ding, H. Liu, X. Zhang, J. Xiao, R. Kishor, H. Sun, B. Zhu, G. Chen, F. Gao, X. Feng, J. Chen, X. Chen, X. Sun, Y. Zheng, *Adv. Funct. Mater.* **2016**, *26*, 7708.

[6] B. U. Ye, B.-J. Kim, J. Ryu, J. Y. Lee, J. M. Baik, K. Hong, *Nanoscale* **2015**, *7*, 16189.